Summer 2015

Nanoenhanced additive manufacturing: Additive introduction onto halloysite nanotubes and into 3D printing filament for tailored material characteristics

James Connor Nicholson
Louisiana Tech University

NANOENHANCED ADDITIVE MANUFACTURING: ADDITIVE INTRODUCTION ONTO HALLOYSITE NANOTUBES AND INTO 3D PRINTING FILAMENT FOR TAILORED MATERIAL CHARACTERISTICS

by

James Connor Nicholson, B.S., M.S.

A Dissertation Presented in Partial Fulfillment
of the Requirements of the Degree
Doctor of Philosophy

COLLEGE OF ENGINEERING AND SCIENCE
LOUISIANA TECH UNIVERSITY

May 2015

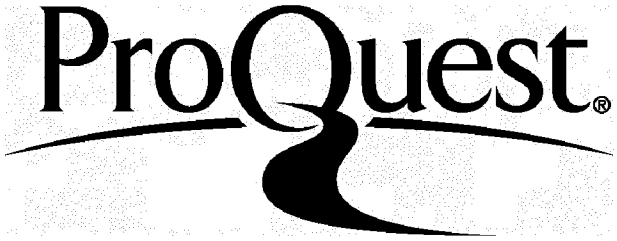

LOUISIANA TECH UNIVERSITY

THE GRADUATE SCHOOL

March 31, 2015

Date

We hereby recommend that the dissertation prepared under our supervision by James Connor Nicholson

entitled

Nanoenhanced Additive Manufacturing: Simplified Methods of Additive Introduction onto Halloysite Nanotubes and Into 3D Printing Filament for Tailored Material Characteristics

be accepted in partial fulfillment of the requirements for the Degree of PhD in Engineering

Chester Wilson

Supervisor of Dissertation Research

Head of Department

Engineering

Department

Recommendation concurred in:

Advisory Committee

Approved:

Director of Graduate Studies

Approved:

Dean of the Graduate School

Dean of the College

GS Form 13a
(6/07)

ABSTRACT

With the rapid advancement of additive manufacturing technologies in recent years on both the microscale and the macroscale, research must be done to test the limits of currently available technologies. On the microscale, halloysite nanotubes have proven to be a viable platform for reinforcement of polymers and time release of loaded chemicals, as well as a substrate material for the deposition of nanoparticles. The range of materials are limited due to polarity conflicts, and often lead to wet chemical processes that use more toxic alternatives. Three-dimensional (3D) printing and macroscale additive manufacturing techniques can be used to generate custom structures, however introduction of additives is a difficult proposition without access to industrial scale equipment. Dopants in the form of nanoparticles show great promise for achieving desired properties. Combinations of the technologies can be used in such applications as targeted treatments in medical research, complex geometrical radiation shielding, and printing and casting of conductive structures for a wide array of use.

In this work, halloysite nanotubes were investigated as a platform for the dry deposition of metallic nanoparticles through sintering of metal acetylacetonate and metal acetate compounds. These coatings were solely or in combinations achieved for iron, nickel, copper, barium, lithium, and gold. Targeted characterization was performed on the iron, barium, gold, and iron/gold dual coated halloysite to quantify exhibited characteristics of the achieved coatings: magnetic susceptibility of the iron coating, X-ray

contrast of the barium coating, and laser resonance with 532 nm and 808 nm wavelengths for the iron, gold, and iron/gold coatings.

A process for fabricating metal doped 3D printing filaments was invented using commercially available equipment and designed to allow for the shielding of low level radiation printed to a user designed specification. Metals used include iron oxide and barium sulfate. Printed films utilizing the iron oxide doped filament were shown to have a dopant threshold through the discovered method of 25wt% and showed an increase in beta radiation shielding of twice that of undoped PLA. Barium sulfate was likewise found to have a 25wt% doping threshold and showed successive increases in opacity when tested against clinical medical X-ray machines.

Conductive 3D printing filaments were also manufactured without modification of equipment, and the electrical characteristics of printed structures were measured in an attempt to classify the use of such a fabrication method for the manufacture of a hybrid conductive/nonconductive structure with attributes defined by the user. It was found that through the method used, conductive filaments using 15-20wt% graphene could be fabricated. Below this threshold, the material proved insulating; above this threshold, filament extrusion was inhibited. Resistances were found to be 1.5±0.4 MΩ and 60±7 kΩ for the 15 and 20 wt% filaments, respectively. Further, notable junction capacitances on the order of 20 pF were found for the 20wt% due to the charge accumulation around air voids inherent in the printing process. No notable junction capacitances were found for the 15wt%. Conductive bone cements were also manufactured to test the impact of the addition of graphene to the manufacturing process. Body resistance testing showed uneven dispersion through normal manufacturing means, and flexural testing showed

varied electrical characteristics depending upon the doping percentage. Mechanical properties were also found to be inhibited at doping percentages greater than 10wt%, however these could be overcome through the use of greater MMA monomer in the manufacturing process.

The first ever ability to coat halloysite nanotubes through a dry sintering process was developed as a proof of principle for multi-functional and real time customizable nanoparticle platforms. Likewise, a method to create and use metal doped and conductive 3D printing filaments on the tabletop scale was realized. Conductive bone cements were also manufactured to test their applicability as a sensor platform. Nanoparticles as additives showed ways to modify these nanotubes or 3D printing filaments with enhanced features and properties easily tailored to desired specifications.

APPROVAL FOR SCHOLARLY DISSEMINATION

The author grants to the Prescott Memorial Library of Louisiana Tech University the right to reproduce, by appropriate methods, upon request, any or all portions of this Dissertation. It is understood that "proper request" consists of the agreement, on the part of the requesting party, that said reproduction is for his personal use and that subsequent reproduction will not occur without written approval of the author of this Dissertation. Further, any portions of the Dissertation used in books, papers, and other works must be appropriately referenced to this Dissertation.

Finally, the author of this Dissertation reserves the right to publish freely, in the literature, at any time, any or all portions of this Dissertation.

Author James Connor Nicholson

Date June 22, 2015

TABLE OF CONTENTS

LIST OF TABLES

LIST OF FIGURES

CHAPTER 1

INTRODUCTION AND OBJECTIVES

1.1 Introduction

Additive manufacturing is the process of laying down successive layers of a material, commonly in a layer-by-layer process, to achieve a desired object or coating without requiring additional processing to remove unwanted material. As of 2013, this definition was modified by ASTM to include the use of a 3D modeling software to model the desired part for manufacturing by a piece of equipment that interpreted the model [1]. This caveat was added due to the rise of mass market availability of 3D printing hardware which led to a near synonymity of additive manufacturing and 3D printing. By stepping away from the added caveat of the use of 3D modeling software, much research is still done in additive manufacturing on both the micro and macroscale.

On the microscale, deposition of coatings primarily requires the use of wet chemical processes that are limited by inherent properties of the material being used. This can lead to exotic and potentially hazardous chemicals to accomplish required coatings in lieu of safer, greener options. For this manufacturing process, a combination of additive manufacturing and subtractive manufacturing are used to introduce material onto the substrate (additive) and remove any unwanted material (subtractive). In addressing the micro/nanoscale, should the platforms be desired in a medical treatment scenario, greener options for developing these coatings must be developed so as to limit

the exposure of the patient to potential leftover chemicals from the manufacturing process. To this end, halloysite nanotubes are of particular interest due to their inherent biocompatibility and tubular shape that allows desired chemicals to be easily loaded into them. In conjunction with this, inherent differing surface charges enable ease of coating in desired chemicals. One way to ensure biocompatibility is by simply coating the nanotubes in biocompatible layers, these will be eaten away over time, leading to only a delay, not a solution, to exposure [2, 3]. To ensure complete deterrence of this exposure, the hazardous chemicals must be removed from the manufacturing process. This will also enable mass manufacture to be done in the United States, where these hazardous chemicals are banned.

Techniques in large scale additive manufacturing have developed rapidly over the past few years. These methods are primarily constrained to raw polymers unless industrial scale equipment is used to introduce additives into the manufacturing material. Researchers and manufacturers have found means of overcoming the raw polymer barrier and introducing additives. These methods typically require either a multistep chemical process or modification of the manufacturing equipment depending on the material. In particular, 3D printing has seen rapid advance with the release of the MakerBot systems that have allowed inspiration to grow due to the low cost of obtaining the equipment and materials. Introduction of additives must be done using industrial equipment located at the manufacturer for custom filaments, limiting the achievable dopants desired [4]. To find effective use of these manufacturing platforms, methods must be developed that are viable across multiple fields of application that do not also necessitate the use of hazardous chemicals or proprietary equipment.

1.2 Grand Challenges of Engineering

Engineering has been responsible for many of the great advances that continued civilizations advancement through the ages. From the tools necessary to facilitate sustained agriculture to the machines of the Industrial Revolution that allowed for mass production of goods, the field of engineering has been vital to continue the required advances to allow civilizations to take the next step in their development. While the previous century provided the most drastic developments yet, moving into the 21st century poses even greater challenges to overcome. At the behest of the National Science Foundation in 2008, the U.S. National Academy of Engineering (NAE) proposed 14 engineering challenges for which solutions must be found to continue the advancement of our society [5].

One of these proposed challenges is the manufacture of better medicines, particularly in the development of what many refer to as personalized medicine. The ability for doctors to utilize custom delivery platforms that have a wide range of properties ranging from magnetism and laser resonance to time delayed release of treatment chemicals is needed. To this end, nanotechnology is widely researched as a possible delivery platform, especially in the use of nanotubes as the delivery mechanism as they can be easily loaded with chemicals for time release and coated through various means to achieve desired coatings. To ensure the treatment platform is biocompatible, manufacture must seek to eliminate hazardous chemicals in the manufacturing process.

Another NAE challenge is the prevention of nuclear terror. Since the discovery of nuclear fission and the manufacture of the atom bomb, quantities of nuclear fissionable material in the world has increased. In conjunction with this, plans for building

improvised nuclear explosives are widely accessible given the rise of the internet. At present, nearly 2 million pounds of both plutonium and highly enriched uranium exist in the world [5]. Because of this, security must be in place every step of the way: where the fissionable material is, routes of transportation into or out of cities/countries, and within cities where the potential detonation may occur.

Should prevention fail and a nuclear terrorist attack occur, large scale cleanup efforts must be readily in place to deal with the fallout of radioactive debris, preferably in a cost effective and versatile manner so as to facilitate the rapid cleanup efforts. Lead lined barrels, the primary means of disposal for radiation, are expensive, heavy, and inflexible, leading to difficulties in the large scope of cleanup efforts [6]. These barrels must also then be shipped to a proper disposal site for the radiation, an added cost on top of every other part of the disposal path. To ensure the fallout to the civilians in the area is limited in time, a platform for onsite containment must be developed so that the area need not be completely abandoned for the decay life of the secondary decay isotopes found in the surrounding region. Further, a means of rapidly achieving containment material in complex 3D geometries must be developed so as to minimize the exposure time of the onsite workers. Such a platform could also have potential use in radioactive medical implants to deter the exposure of healthy tissue to the radiation, leading to a more effective therapy in the targeted treatment areas.

1.3 Objectives

The objectives of this research are three fold. First, the applicability of metal acetylacetonates and metal acetates for the dry deposition of metal nanoparticles onto the exterior of halloysite nanotubes will be examined, negating the need for wet chemical

processes. Through thermal degradation, positively charged metal ions onto the negatively charged outer lumen of the nanotubes. These nanotubes will be coated in one metal or in combination to test tailorability of perceived beneficial characteristics. The metal coated nanotubes will then be characterized for targeted properties associated with the deposited nanoparticles. It is hypothesized that these nanotubes can serve as a modular platform for a range of applications due to the unique inherent properties and biocompatibility of the nanotubes.

Second, a versatile platform for radiation shielding that seeks to provide protection against all four types of radiation based on 3D printing will be researched. This body of work will attempts to create extrudable plastics using a modular platform that can allow for the production of thin films or complex geometrical objects to be fabricated that have a specified tailorable level of shielding as desired by the manufacturer. Three-dimensional printing will be explored as the manufacturing method, and only off-the-shelf equipment will be explored as the means of this manufacture to test the current limitations inherent in commercially available equipment.

Last, this research will seek to achieve conductive printable filament using off-the-shelf equipment with no modification. Graphene will be used as the conductive additive, and filament utilizing graphene will be fabricated and characterized for 3D printing. While current research claims this has been achieved, it necessitated manufacture of proprietary equipment, was constrained to one type of polymer, and could not breach a threshold of 15wt% doping of graphene into the polymer. This research will characterize important electrical characteristics such as resistance, piezoresistivity and junction capacitance of the layers for printed objects.

1.4 Organization of Dissertation

This dissertation comprises six chapters. Chapter One is a brief introduction to the current issues in radiation shielding and additive manufacturing and states the objectives for this body of work. Chapter Two presents a detailed review of prior literature and state of the art research in halloysite coatings and uses and additive manufacturing techniques with a focus on 3D printing efforts that are currently being pursued. Chapter Three focuses on halloysite nanotubes as a platform for custom nanoparticle sheaths that have differing properties such as magnetic control, contrasting agent, or laser resonance dictated by the material used. Chapter Four presents a new additive manufacturing technique that allows for the introduction of powdered metal additives into 3D printing filaments, discusses printability of the manufactured filaments, and tests the radiation shielding capabilities of fabricated constructs utilizing these filaments. Chapter Five further explores the fabrication method presented in Chapter Four as a means of turning the inherently insulating printing media commonly used in 3D printers into a conductive material and characterizes inherent electrical properties that must be considered in developing complex constructs that utilize the filament. Chapter Six draws conclusions on the works presented in this text and discusses future work.

CHAPTER 2

BACKGROUND

2.1 Introduction

It has been said that we are currently in the third industrial revolution [7]. Materials and technologies that were once only theoretically possible are now fabricated in small laboratory facilities or widely used in industrial applications. From nanotubes to 3D printing a car, capabilities are increasing rapidly to manipulate materials in ways once only thought of [8]. These same advances can be seen in both medicine and radiological containment. For childhood leukemia, survival rates have increased from 10% in the 1960's to 90% in 2000 [9]. Likewise, radiological cleanup has found more flexible containment methods for dealing with hybrid low level waste, especially as pertains to radioactive waste from oil drilling [10]. Despite these advances in both the biomedical treatment and radiological containment areas, setbacks have also occurred. Pancreatic cancer still has a high mortality rate, and 1% of orthopedic surgeries still result in infections [11, 12]. Large contamination of waste disposal sites still occurs due to improper packaging of waste material as in the WIPP site incident in 2014 [13]. The use of off-the-shelf equipment with little to no modification and new manufacturing techniques with modular capabilities may be greatly advantageous for both personalized medicine and radiological containment.

A review and understanding of recent advances in additive manufacturing on both the macro and microscale is necessary to understand the current capabilities of available manufacturing techniques and the areas where their use could prove of great benefit. This review will be begin by covering microscale techniques for deposition of thin films, then look to a more specific platform for this deposition: halloysite nanotubes. Next, the areas where these halloysite nanotubes area currently being used and researched will be discussed. A review of macroscale additive manufacturing will be done with a focus on advancements in recent years, especially as pertains to 3D printing and the new additive introduction means that have enabled printing of objects with customized characteristics. Finally an examination of PMMA bone cements as pertains to the medical field will be given for context of the conductive PMMA bone cements fabricated in this work.

2.2 Microscale Additive Manufacturing

When examining the deposition of material on the micro/nanoscale, many techniques are available to researchers. For the purposes of this text, four methods will be examined : chemical vapor deposition (CVD), layer-by-layer (LbL), thermal evaporation, and sputter coating. These processes are most applicable as they are widely used in the coating of the halloysite nanotubes discussed in the next section.

2.2.1 Chemical Vapor Deposition

Chemical vapor deposition (CVD) is a versatile process for the manufacturing of coatings, powders, and fibers using metals, nonmetallic elements such as carbon or silicon, and a large number of compounds including carbides, nitrides, and oxides [14]. CVD is defined as the deposition of a solid onto a heated surface through a chemical reaction between the substrate and the deposited material in the vapor phase. Because the

depositing material is in the vapor phase, the deposition occurs on the atomic or molecular level, leading to thorough thin film coatings [15]. This process is limited as it is most versatile at high temperatures of 600+ °C, temperatures at which most substrates are not thermally stable.

In research, CVD has found wide use for fabrication on the microscale. One application is in the growth of thin film diamonds to enhance mechanical properties, especially for the hardness of tools [16]. Another is for the growth of carbon nanotubes, whose aspects (length, diameter) can be easily controlled via temperature and catalyst alteration, as well as catalyst free manufacturing of these carbon nanotubes [17, 18]. Further, manufacturing of thin films of carbon known as graphene can also be done using CVD [19-21]. Another area of use for CVD is in the creation of thin films that exhibit certain properties such as superhydrophobicity or superhydrophilicity [22]. It can also be used in the growth of high aspect nanowires wherein the deposited material is built up in spires rather than as a composite film [23].

2.2.2 Layer-by-Layer

Layer-by-layer (LBL) techniques use self-assembly mechanisms of oppositely charged linear or branched polyions and nanoparticles to fabricate layers onto a charged substrate [24]. By introducing an additive of the opposing charge to that of the substrate, the additive will self-assemble onto the substrate through the available bonds [25]. This method can achieve films ranging in 5-500 nm thick, with growth steps for monolayers on the order of about 1 nm [26]. The forces used are primarily electrostatic and covalent in nature, and the self-assembly was first discovered in 1966, however it did not find wide use until its rediscover in the nineties [27]. This method is ideal for the fabrication

of layers where a perfectly ordered assembly is not required, but rather a lower order of coating is acceptable. The terminal layer can be of either charge, but oxidation may occur depending on the terminal layer material [28-30]. This method has also been used to coat materials in lipid and protein layers, allowing for a biocompatible external layer to a system that may involve cytotoxic elements in the coating process to achieve a desired characteristic [31-33].

2.2.3 Thermal Evaporation

Thermal evaporation is a technique where the temperature of the material to be deposited is raised until the vapor pressure is high enough ($> 10^{-2}$ Torr). If the ambient pressure is low enough, the vapor from the source material will condense onto the cooler substrate [34]. One issue with this process is the nonuniformity of the films if the substrate has a rough surface [35]. Further, if there are gaseous particles along the path of the traveling vapor atom, leading to less particles reaching the substrate and difficult thickness control [36].

In research, this method has found wide use for the deposition of a variety of materials. For cases where an oxide is desired, a lower vacuum can be used with a deposition material. This has led to nanostructures made of ZnO, SnO_2, and In_2O_3 to name a few [37]. This method is not constrained to thin films, and has shown to be versatile enough for the formation of nanobelts, nanowires, nanoribbons, nanorods, and hollow tubule structures [38-42].

2.2.4 Sputter Deposition

Sputter deposition is a physical vapor deposition wherein particles from the depositing material are ejected from the bulk material [43]. Because of the energies of

the particles leaving the bulk material, damage to the substrate can occur, leading to embedding of the sputtering material or ablation of the substrate [44]. Though the ablation may occur, sputtering has found wide use due to the rapid growth of thin films via this method. This has been used with numerous elements in applications such as simple thin film growth to relatively large thicknesses (>1 mm) for desired attributes to manufacturing semiconductor dots [45-48].

2.3 Halloysite Nanotubes

Halloysite nanotubes are naturally occurring nanotubes composed of silica and alumina [49]. Bonding defects between the alumina and silica lead to net negative and positive charges on the exterior and interior lumina, respectively [50, 51]. The typical inner diameter, outer diameter, and length of these tubes are 1-30 μm, 30-50 nm, and 100-2,00 nm, respectively [52-54].

As halloysite nanotubes are hollow cylinders, they can easily be loaded with a variety of chemicals through vacuum cycling, which in turn leads to a time release of the loaded chemical agent [3]. The most often researched application of this is extended delivery of drugs due to the biocompatibility of halloysite [55]. During loading of chemical agents under pressure, the lumen is filled, but some may remain as a coating on the exterior of the halloysite. For drug delivery, the release of the drug is first through desorption of the active agent from the outer lumen and the ends of the tube, then a much longer pore diffusion out of the loaded inner lumen [56]. R.R. Price *et al.* have demonstrated the ability to load both hydrophilic and hydrophobic agents into the halloysites follow appropriate pre-treatment of the nanotubes. Similar results were found with Veerabadran *et al.* in the aqueous loading of soluble drugs. Here, the nanotubes

were loaded with the chemical agent through vacuum cycling, then centrifuged to isolate the loaded nanotubes. Once done, a 5-10% initial burst release of the agent was found, followed by a much slower release [3].

Another area loading of halloysite has found use is in developing self-healing concrete and polymer matrices. To this end, an epoxy based solution can be loaded into the halloysite. Upon fracturing of the tubes or a difference in pressure attributed to fracturing of the concrete, the epoxy will be released into the damaged area, then cure so as to reinforce the body [57]. Another application in concrete and polymers is to act as a container for anti-corrosive chemicals [58]. The loaded anti-corrosive slowly leaks from the halloysite into the body that they are doped into over a long period of time, leading to continuous introduction of the anti-corrosive material into the body of the object over a long period of time.

Because halloysite nanotubes are naturally occurring, hydrophilic, and have opposite surface polarizations for the inner and outer lumen, they have found many applications in the maturation of nanotechnology due to ease of coating or ease of filling. Halloysite also has thermal and mechanical properties that are highly desirable in polymer composite areas, primarily for the reinforcement of low density polymers. By varying the amount of halloysite and selecting applicable coatings, the thermal and mechanical properties of given polymers can be specifically tailored to the desired application [59-61]. Mechanical properties can also be enhanced through the addition of halloysite. It has been shown that the tensile strength and tensile modulus to increase when halloysite is used as a filler [62]. In further study, this has been attributed to the interfacial bonding between the polymer matrix and the added halloysite [63]. For

shielding applications, this enables the tailorability of the mechanical breaking point to the application desired. In comparison to other clay additives, halloysite has shown exceptional dispersivity, as well as visual transparency in the polymer matrix [64].

For achieving coatings of these nanotubes, layer-by-layer is commonly used as the inherent charge differentials make coating through this method very easy. Coating of layers can be done for many reasons. The first is to slow or control the release of chemicals diffusing out of the halloysite, potentially in a time delay scenario [65]. The second is using the halloysite as a platform for the deposition of catalytic material [66, 67]. Both of these methods use the inherent negative exterior lumen as a basis for deposition of the coating material in a solution of the opposing charge. As previously discussed, this can limit what material is placed onto the nanotubes due to polarity conflicts. One method of overcoming this is the use of alternating layers of differing charge to build up the coating rather than using a bulk coating method.

In comparison to carbon nanotubes, halloysites prove much cheaper, and far less toxic [68]. Due to both of these factors, this makes the addition of halloysite into shielding applications very favorable due to the lack of toxicity to the environment. A high surface area of 64.19 m^2/g combined with a low cost also makes halloysite ideal candidates for the absorption of waste products as they can be easily disposed of once their absorption limits have been met [69]. By coating halloysites in certain materials, ionic bonding to the halloysite structure can be achieved in liquid environments [70]. This is aided by the spiral structure of the halloysites and the water molecule defects found in the halloysite bonding layers, providing a fast adsorption rate [71]. This could

potentially lead to specialized coating-enabled adsorption of radioactivity from liquid wastes, further reducing the cost of disposal.

2.4 Metal Acetylacetonates and Metal Acetates

Metal acetylacetonates and metal acetates are unique salts that are commonly used to detect for metal ions in aqueous solutions. They are made of a metal ion (x=+1, +2, or +3) and the acetate/acetylacetonate bonds [72]. Iron and gold are more commonly known compounds, but other metal compounds exist such as barium, nickel, zinc, copper, chromium, cobalt, lithium, and titanium, and are widely manufactured by the chemical industry. Metal acetylacetonates are also used as precursors for synthesis of nanoparticles, metal catalysts, and NMR shift reagents [73-78]. These compounds also thermally degrade between 200-300 °C. During thermal degradation, acetone and carbon dioxide are outgassed for metal acetylacetonates in a low energy reaction, and leaving behind positively charge metal ions. Metal acetates also degrade through outgassing acetone and carbon dioxide albeit with higher energy reactions, leading the metal acetate to explode upon thermal degradation [79]. Due to the negatively charged outer lumen of the halloysite, these compounds make ideal candidates for dry sintering of metal coatings due to the positively charged ions left after thermal degradation.

2.5 Macroscale Additive Manufacturing

Additive manufacturing offers many promising venues for rapid prototyping, especially should a method of introducing and characterizing additives into the fabrication process be achieved. Additive manufacturing is again defined as the fabrication of an object through the introduction of successive amounts of material, commonly in a layer-by-layer process. As of 2013 this was modified to include the use

of a computer-aided design (CAD) file that is converted to a stereolithography (.STL) file to physically fabricate an object through a machine that interprets the file [80]. Though these methods of rapid prototyping have long been used in industry for rapid prototyping, commercially available equipment on the consumer scale is only now becoming available [81-83]. The majority of basic additive manufacturing techniques use readily castable materials such as plastics, but methods exist for ceramics and metals too. In a perfect scenario these methods would be interchangeable independent of the material being used, however very different manufacturing means must be used depending on the material [84].

Additive manufacturing currently falls into three categories depending upon the state of the material being used: solid based, liquid based, or powder based. Solid based additive manufacturing is primarily restricted to the manufacture of laminated objects wherein sheets of material are laid successively on top of one another, then fused through temperature and pressure, then cut to the desired shape using a carbon dioxide laser [85]. While applicable to metals, this method will generate large amounts of waste material post manufacturing. Metals are more commonly additively manufactured through power based methods wherein layers of powder are sintered, melted, our bound through chemical means before the next successive layer is placed [86-89]. The most common of these methods is selective laser sintering where a laser is used to sinter each powdered layer before the next is laid down [90]. Liquid-based additive manufacturing uses either a material that is melted, deposited, then solidified or a liquid polymer that is deposited then solidified through a curing process [91]. With liquid polymers, the current layer

must be polymerized before the next layer can be deposited, leading to issues with maintaining resolution for the manufactured constructs [92-94].

For consumer level additive manufacturing, 3D printing technologies have become widely available due to market place demand [95, 96]. A typical 3D printing setup utilizes a user generated .STL file to generate the desired object so long as the object fits within the printing volume of the 3D printer [97, 98]. Because of the ease of using these devices, wider arrays of materials and the ability to tailor the properties of those materials in a user defined way are required [99]. Also needed is a method to ensure consistent dispersion in the host polymer without requiring industrial grade equipment that still ensures printability through commercially available printers.

Fused deposition modeling printers typically use thermopolymers filaments to build the desired three-dimensional object in a layered manner. Thermopolymers are unique in that they do not melt, but rather reach a state of melt-flow where they run like a very thick liquid. These thermopolymers do not retain their heat very well, and once they have left the heated print head, rapidly return to room temperature, a desired quality for maintaining resolution. The most commonly used thermopolymers polylactic acid (PLA) and acrylonitrile butadiene styrene (ABS). Consumer printers operate at resolutions of tens of microns in the x- and y-directions and 50-400 microns in the z-direction. The two commonly used filament diameters are 1.75 mm and 3mm, and these pass through a print head extruder that narrows to a nozzle of 0.4 mm diameters, forcing the plastics into meltflow as they pass through. As the print head temperature, percentage fill, and resolution are easily modified, highly variable designs of the same construct can

be obtained. This can be inhibitory as inherent print defects do exist for these machines due to offset print platforms, variations in temperature, and print speed.

The fabrication process can be further customized by using designer filaments with tailored material properties. One such filament is called Laywood, a PLA-saw dust mix that allows for printing of plastic with the texture and smell of wood [100]. Altered temperature can allow for a change in the wood tones and a darker or lighter wood coloring. Another filament is call Carbomorph, a conductive filament that utilizes carbon black and PCL to achieve printing of conductive structures [98]. A printer with dual heads can be used to fabricate an object that has selected portions that are conductive or insulating, resulting in a printable circuit construct. Little characterization of the electrical properties has been done on this filament other than to show conductivity was achieved.

The push for cheaper and customized filament creation has led to the design of personalized filament extruders. These devices use pellets of the desired thermopolymer to fabricate the filaments. An auger is used to force the pellets through a heated meltflow zone and out a metal die that is drilled to the diameter of the desired filament. Once the filament has exited the metal die, it rapidly cools back to room temperature, maintaining the desired diameter for printing. The temperature is easily modified, however temperatures that are too high will result in filament with too small a diameter and temperatures that are too low will result in little to no meltflow, potentially breaking the driving motor of the auger.

It is difficult to introduce additives into this system as a gradient of the desired additive will result along the length of the filament with no way of ensuring the amount

of dopant per inch within the filament. The filament can be cut up and reextruded after this process, but this will lead to additional heating of the additive, time, and cost in waste materials, as well as a loss in confidence in doping percentages.

2.6 PMMA Bone Cements

Bone cement is typically composed of polymethylmethacrylate (PMMA) and has been used by orthopedic surgeons for more than six decades. The first use of this material was in 1958 when British orthopedic surgeon Sir John Charnley implanted a hip endoprosthesis using PMMA [101]. The PMMA allows for the implantation and fixation of prostheses to the bone and has been the subject of continuous development in parallel with improved surgical techniques.

Medical grade bone cements typically consist of 90% polymer and the rest an additive to lend radiopacity to the cements such as barium or zirconium oxide [101]. To create the bone cement, a spherical powdered PMMA is mixed with a liquid monomeric methylmethacrylate (MMA) in the presence of a catalyst [102]. The powder quickly dissolves in the monomer and the monomer then polymerizes at room temperature to form a putty-like cement. Once polymerized, the mixture will fully set within an hour, thus casting or application of the cement must be done rapidly. The resulting set bone cement is a strong but brittle mass. The spheres and the polymerized monomer do not bond chemically [103].

Many different types of bone cements are commercially available that have different viscosity, processing, content, and application properties [103]. During the curing process, many surgeons mix antibiotics into the bone cement during the mixing process [104]. Many antibiotics can be used, the typical being gentamicin, tobramycin,

or vancomycin [105]. Gentamicin is primarily used in the United States while tobramycin is commonly used worldwide, both for gram-negative bacterial infections [106, 107]. Vancomycin is used in the treatment of gram-positive bacterial infections [108]. All of these antibiotics are available in powdered form, and can be readily mixed with the PMMA powder prior to the introduction of the MMA monomer. Once the bone cement is implanted, the added antibiotic will leach from the bone cement to the local areas. This is usually enough to kill any bacteria left in the operative wound. One consideration is the leaching time from the bone cement is limited, typically on the order of the first 24 hours [109]. Previous experiments have shown that release of antibiotic is limited to less than 10% of the loaded antibiotic. This is attributed to the nonporous nature of the cement. Further, the introduction of the antibiotics leads to mechanical weakening of the cement, restricting the amount of antibiotic that can be added [110]. In looking for new and improved uses of these bone cements, especially as may pertain to sensor development, the introduction of other additives is desired to achieve new properties such as conductivity. Little work has been done to this end, especially as pertains to the impeded mechanical properties of the cements once the additive is introduced.

CHAPTER 3

DRY DEPOSITION OF METAL NANOPARTICLES ONTO HALLOYSITE NANOTUBES

3.1 Introduction

Halloysite nanotubes are naturally occurring aluminosilicate tubular composites with a structure of ($Al_2Si_2O_5(OH)_4 \cdot 2H_2O$). Due to bonding deformations, a hollow cylindrical structure is achieved that has inherent charge imbalance: the outer surface exhibits a net negative charge while the inner surface exhibits a net positive charge. The lengths of the tubes commonly varies from 100-2000 nm with common inner/outer diameters on the order of 30-50 nm and 10-30 nm, respectively.

The natural occurrence of these nanotubes combined with the ease of coating and loading these nanotubes has led to much research on the material. The net charge differential between inner and outer surfaces has also enabled multiple layered coatings to be accomplished on the surface of these nanotubes.

Due to the hollow inner structure of the nanotube also allows for pore diffusion of loaded chemicals via vacuum loading. Another benefit of these tubes is the adsorption of chemicals at room temperature from solution due again to the charge imbalance between surfaces. These two properties have led much research on halloysite nanotubes to be done in the area of time delayed drug delivery. This can be accomplished through the loading of the desired chemical into the nanotube, then coating a sacrificial layer of some

biocompatible nature to the exterior of the nanotube. Once introduced into the body, the sacrificial layer is eaten away, leading to a time release via pore diffusion of the chemical. This diffusion is not completely exponential as there is a burst release once the sacrificial coating is worn away, but exponential characterization is achieved after a short time.

Halloysite has also shown to improve mechanical properties of polymers when used as an additive. Specialized coatings and loaded chemicals have also shown to allow for "self-healing" material that overcomes damage through the release and oxidation of the loaded chemicals that is triggered when damage occurs. Complex coatings of metals and polymers have also been achieved leading to a variety of properties, however these require long chemical process, and often necessitate the use of hazardous chemicals in place of less hazardous options due to the hydrophilic nature and polarity inherent in the halloysite.

This chapter presents a method to coat halloysites with a variety of metallic sheaths to achieve tailorable properties in a short amount of time. The metal sheaths achieved were comprised of iron, barium, copper, nickel, lithium, and gold. Additionally, multilayered metallic sheaths were accomplished in the form of iron/old coatings. Desired characteristics were measured for the iron, barium, and gold coated halloysite.

3.2 Design and Objectives

This research examines the ability to deposit material onto the exterior of the halloysite nanotubes utilizing only sintering of existing compounds with the halloysite nanotubes. To ensure coating of the desired element(s) was achieved, electron

microscopy and elemental analysis was performed. Further, unique characteristics of the coating additive were tested to ensure retention of desired properties once placed on the surface of the nanotube. The following sections give a more in depth breakdown of the objects to be achieved.

3.2.1 Metal Coating Objective

The first objective is to achieve deposition of metal nanoparticles onto the surface of the nanotube while reducing the number of required steps, the cost of materials, and the time required to fabricate the resultant coated nanotubes. A method of selectively coating the halloysite nanotubes in iron, gold, copper, barium, lithium, copper, and nickel will be developed.

3.2.2 Modular Metal Coating Objective

The second objective is a furthering of the first, ensuring tunability of the sheath of metal to be deposited onto the surface of the nanotube. A method of coating the nanotubes with multiple metal compounds will be developed and the nature of these multiple metal coatings will be explored.

3.2.3 Imaging and EDAX Objective

The third objective is to confirm that the coatings present are the desired metals and to observe the behavior of the nanoparticles on the surface of the nanotube post-manufacture. Scanning electron microscopy (SEM) and transmission electron microscopy (TEM) will be used for imaging. Energy dispersive X-ray analysis (EDAX) will be used to examine the elemental composition of the coated halloysites. This characterization technique excites electrons in the target material via X-ray and characterizes the present elements by signature photons emitted upon relaxation of these electrons. For heavier

elements, two or more characteristics signals can be obtained. Elements equal to or lighter than beryllium will be unable to be measured due to the use of a beryllium lens; the machine is calibrated to discard these characteristic energy signals.

3.2.4 Magnetic Susceptibility Objective

The fourth objective is to test the susceptibility of halloysite coated with iron nanoparticles, and to quantify the materials ability to retain a magnetic field. Gauss measurement and alternating gradient magnetometer (AGM) will be used.

3.2.5 X-ray Opacity Objective

The fifth objective is to characterize X-ray opacity of barium coated halloysites when added to a polymer matrix. Specifically, PMMA bone cement will be used as an embedding media for the nanotubes to observe X-ray opacity of the overall construct.

3.2.6 Laser Resonance Objective

The final objective is to test resonance with specific wavelengths of light of the nanoparticles deposited onto the surface of the nanotube. Specifically, nanotubes coated with iron, gold, and both iron and gold sheaths will be tested for laser resonance at 532 nm and 808 nm wavelengths utilizing a thermocouple to test for heat generated by the sample.

3.3 Fabrication

Metal acetylacetonates degrade completely around 300 °C , outgassing a mixture of acetone, methane, and carbon dioxide while leaving behind positively charged metal ions. By mixing metal acetylacetonates with the halloysites, then sintering at 300 °C, the presence of the negatively charged exterior lumen of the halloysite presents a readily

available bonding opportunity for the metal nanoparticles, allowing for a one step coating process of the metal nanoparticles.

All coated halloysites shown here were subjected to sintering at 300 °C for 4 hours, and, with the exception of the gold coating, all were mixed in a 1:1 ratio by weight metal acetylacetonate to halloysite nanotubes. 100 mg of each (halloysite and the associated acetylacetonate) were weighed, mixed in a VWR borosilicate glass container, then vortexed for one minute. A Vulcan oven was used for the sintering process. The containers were placed inside, then the oven was programmed to heat to 300 °C at a rate of 12.8 °C/min, then held at this temperature for 4 hours. The program then cooled the oven to room temperature at a rate of 5 °C/min. These heating/cooling rates were chosen arbitrarily as nothing happens below 150 °C, increasing linearly with added heat after that. This process resulted in metallic sheaths or nanoclusters deposited onto the surface of the nanotubes. Temperatures were varied for certain additives. After the sintering process, the glass container was covered, vortexed, then ground by mortar and pestle to break up and large clumps due to present humidity in the environment. Figure 3.1 shows a sample post sintering, pre vortex/grounding.

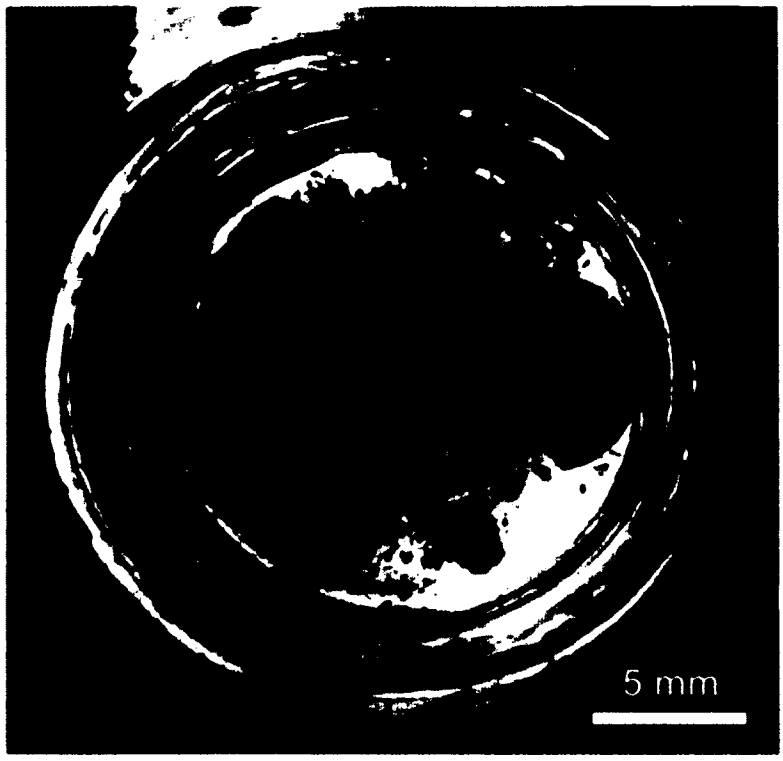

Figure 3- 1: Sintered iron coated halloysite post sintering.

3.4 Testing

Testing was done in three parts. First, fabrication of the metallic sheaths were performed, and SEM/TEM imaging was done along with EDAX to confirm the coating found in SEM/TEM was of the expected elemental composition. Next, fabrication of dual coated halloysite nanotubes were performed, and imaging was done via TEM and EDAX to confirm the presence of both dopants. SEM was unable to be performed due to the magnetic nature of the coatings. Finally, coating specific tests were done as applicable to the various sheaths obtained to test their performance against currently used additives.

3.4.1 Metallic Sheath Creation

Multiple batches of each metal acetylacetonate additive were made to verify consistency of the process. Conditions were kept as sterile as possible, and new borosilicate glass containers were used for each fabricated batch.

3.4.2 Halloysite Imaging and Verification

All coated samples were imaged using SEM and TEM. SEM comparison of raw halloysite to coated halloysite visually confirmed coatings were present, and TEM comparison showed greater density material was present on the surface of the nanotube while preserving an empty lumen. EDAX was used to confirm the elemental makeup of the sintered samples, confirming the desired additive was present in the sample.

3.4.3 Magnetic Characterization of Iron Coated Halloysite

Magnetic characterization was done in two parts for the iron coated halloysite. First, a sample of the iron coated halloysite was fabricated in a 1:1 mixture of iron (III) acetylacetonate to halloysite. The sample was then subjected to a magnetic field for 72 hours, and measured with both a DC Gaussmeter. Additional characterization was done to find the hysteresis curve using both an alternating gradient magnetometer (AGM) and vibrating sample magnetometer (VSM).

3.4.4 CT Scan of Barium Coated Halloysite

CT scan images were collected of PMMA bone cement samples loaded with varying percentages of uncoated halloysite and barium coated halloysite to test for contrast of the polymer. Undoped PMMA cements, commercial barium-enhanced cements, halloysite only enhanced cements, and combinations therein were imaged on the CT machine to act as positive and negative controls for each additive. The CT facility at

the Biomedical Research Institute in Shreveport, Louisiana was used, and calibrated to normal use standards.

3.4.5 Laser Resonance Characterization of Iron, Gold, and Iron/Gold Dual Coated Halloysite

Resonance data of the iron, gold, and iron/gold dual coated halloysite were tested using lasers with wavelengths at 532 nm and 808 nm. These two wavelengths were chosen specifically for a strong resonance peak of the gold nanoparticles (532 nm) and for a local maximum resonance peak of the gold nanoparticles while also provided for transmission through living tissue (808 nm). Samples were tested in two ways. First, dry samples of the material were placed in clean borosilicate glass containers and tapped until a uniform surface was achieved. A thermocouple was placed on the bottom of the container, and the sample was exposed to the laser for 5 minutes. Second, 10 mg of halloysite were mixed into 1 mL of water in a clean borosilicate glass container. The sample was vortexed for one minute to achieve dispersion of the nanotubes in the water, then the sample was exposed to the laser for 5 minutes.

3.5 Results and Discussion

The method to create a modular platform for of metal deposition onto the surface of halloysite involved trials of alternative methods utilizing metal acetate and metal acetylacetonates before the process was optimized. First, metals were deposited onto the surface of the nanotube. Once this was proven a success, multiple layered differing metals were tested and confirmed. As different characteristics were tested for differing coatings, characterization paths differed depending upon the metal deposited and the attribute to be confirmed.

3.5.1 Coating Halloysite Nanotubes

The metal acetates and metal acetylacetonates were used in a sintering process to achieve varying coatings of metal onto the surface of halloysite. Once coated, the nanotubes were analyzed using SEM, TEM, and EDAX to confirm the presence of the metal additive and examine how differing metals reacted to the negative lumen of the halloysite. The coated nanotubes were secured onto carbon tape to prevent damage to the SEM/EDAX system, resulting in the carbon peaks seen. Nanotubes were coated specifically with iron, barium, copper, nickel, lithium, and gold.

3.5.1.1 *Control Halloysite Nanotubes*

Prior to examining the coated halloysite, images of the raw halloysite were obtained for comparison. SEM (Figure 3-2), TEM (Figure 3-3) and EDAX (Figure 3-4) were performed.

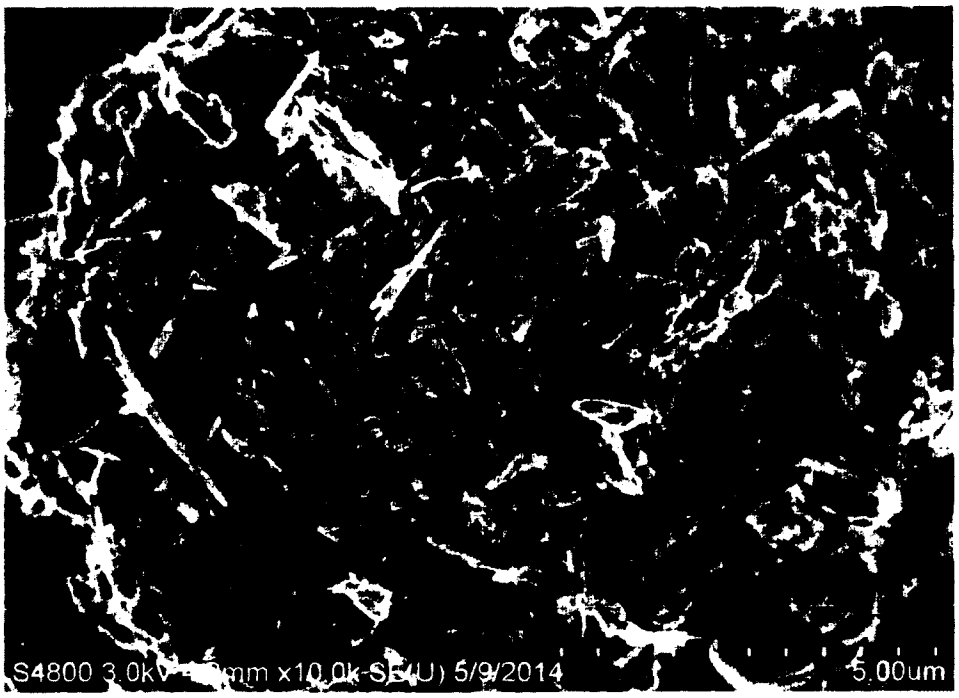

Figure 3- 2: SEM of control halloysite nanotubes.

Figure 3- 3: TEM of control halloysite nanotubes.

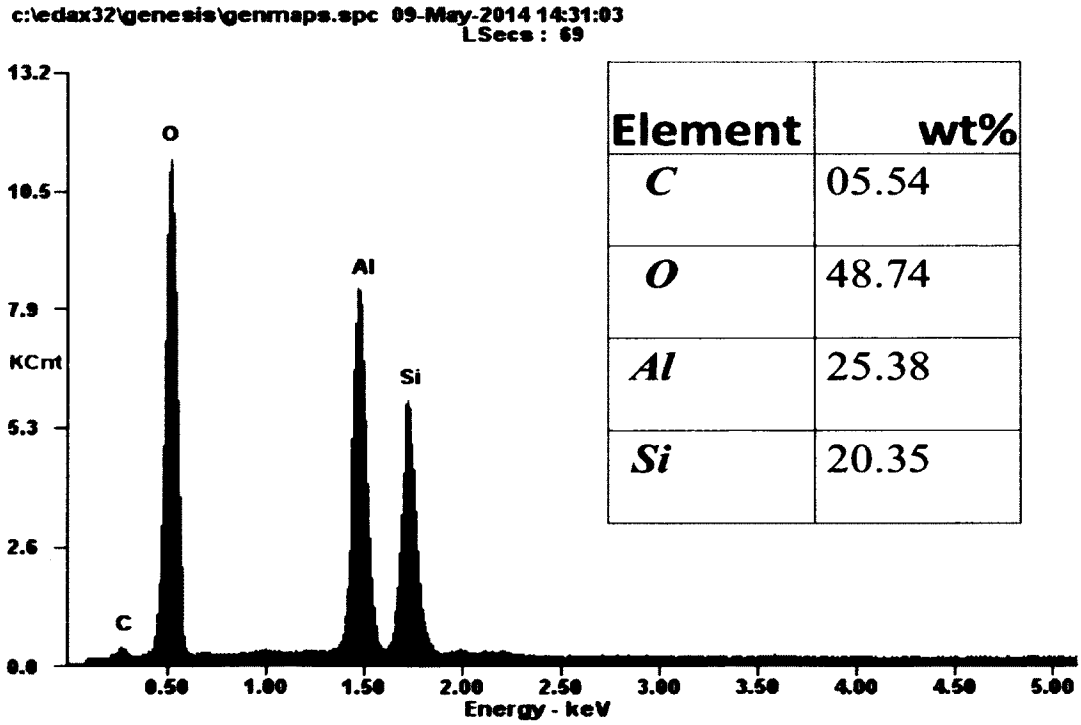

Element	wt%
C	05.54
O	48.74
Al	25.38
Si	20.35

Figure 3- 4: EDAX of control halloysite nanotubes.

Halloysite clumps in the presence of water, and this is evident in the SEM picture due to humidity in the air. The TEM shows the characteristic hollow inner lumens of the tubes, as well as the differing sizes of respective tubes. The EDAX confirms the expected aluminum, silicon, and oxygen present in the aluminasilica nanotubes and the carbon peak characteristic of the carbon tape used. It should be taken from these pictures that the nanotubes show smooth surfaces with no artifacts present on either the outer surface or the interior of the nanotube.

3.5.1.2 *Iron Coated Halloysite Nanotubes*

For the coating of the halloysite with iron, two compounds were used: iron (II) acetate and iron (III) acetylacetonate. The samples were run in 100 mg 1:1 reactions of halloysite and either the acetate or the acetylacetonate. The sintered powders were then vortexed and ground by mortar and pestle to overcome clumping from humidity during the sintering process. The iron (III) acetylacetonate coatings proved to be magnetically susceptible while the iron (II) acetate coatings did not. Due to the magnetically susceptible nature of the iron acetylacetonate sintered nanotubes, SEM had to be performed on the iron acetate coated tubes due to the high magnetic fields used for SEM imaging, and is shown in Figure 3-5. TEM and EDAX were able to be performed on the iron acetylacetonate sintered tubes, and are shown in Figure 3-5 and 3-6, respectively. These are shown in Figure 3-5, Figure 3-6, and Figure 3-7.

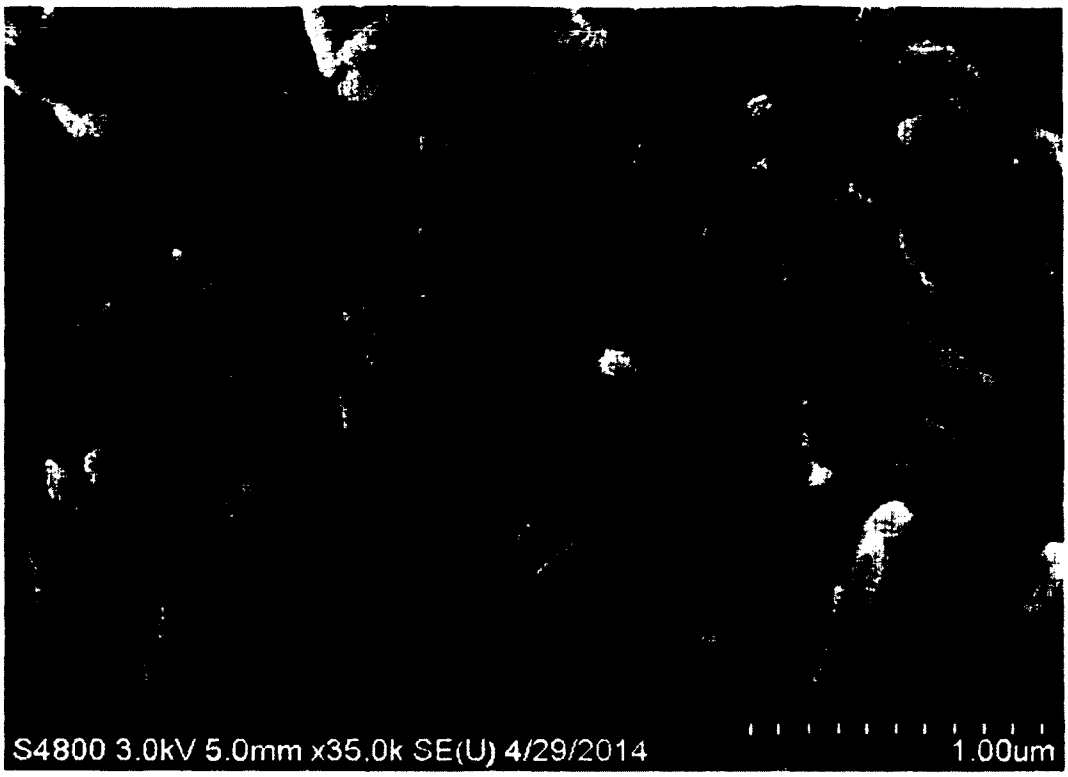

Figure 3- 5: SEM iron coated halloysite using iron (II) acetate.

Figure 3- 6: TEM iron coated halloysite using iron (III) acetylacetonate.

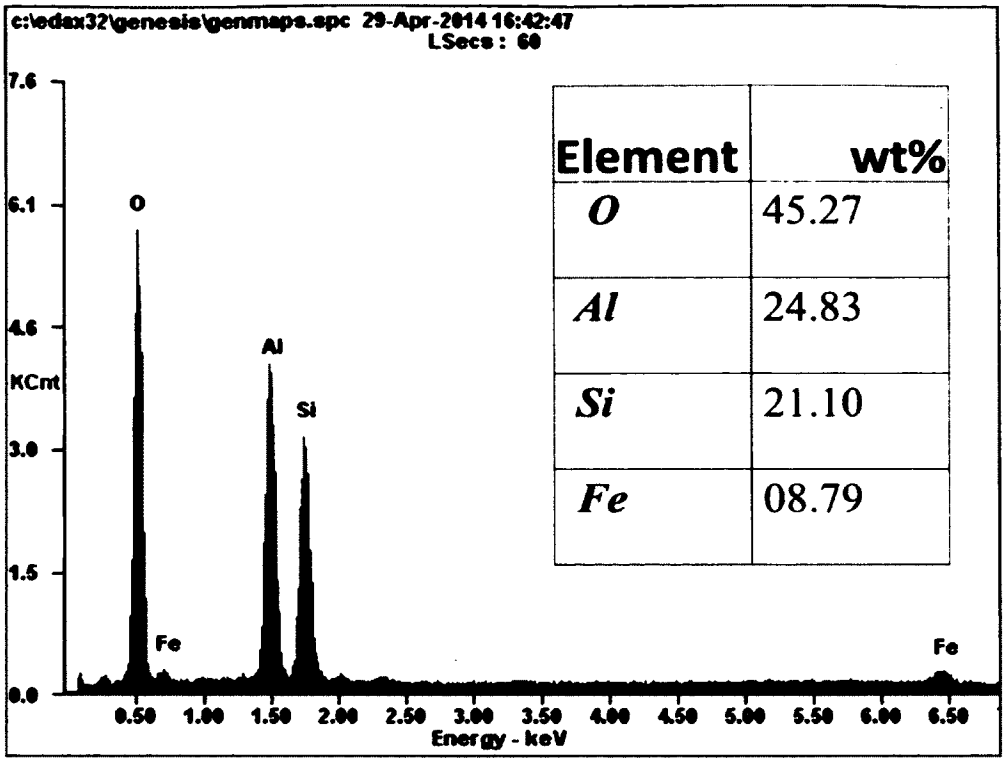

Figure 3- 7: EDAX iron coated halloysite using iron (III) acetylacetonate.

Imaging and EDAX confirm the coatings to be iron. It should be taken away that the iron tends to clump in spheres on the surface of the halloysite rather than to bind evenly along the surface of the tube. Further, the iron tended to preferentially bond near the ends of the nanotube rather than along the middle. Due to the magnetically susceptible nature of these coated nanotubes that utilize the iron (III) acetylacetonate, potential uses could be found in controlled localized drug delivery or for hyperthermia treatment. Further, localized chemosensitizing agent delivery could increase the effects of cancer treatments while also reducing the amount of sensitizing agent used.

3.5.1.3 *Barium Coated Halloysite Nanotubes*

To coat halloysite with barium, barium acetylacetonate dihydrate was used. Fabricated batches were created in 1:1 ratios in weights of either 100 mg or 250 mg. The

resulting mixture was then sintered at 300 °C, then vortexed to overcome any clumping. SEM, TEM, and EDAX are shown in Figures 3-8, 3-9, and 3-10, respectively.

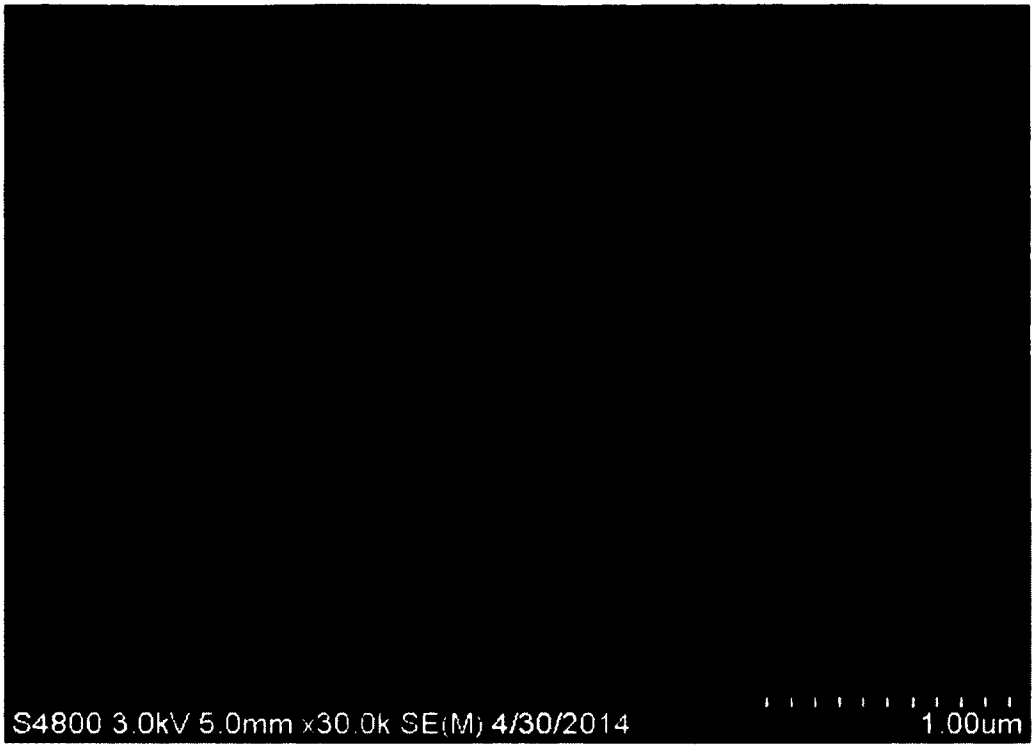

Figure 3- 8: SEM of barium coated halloysite nanotubes.

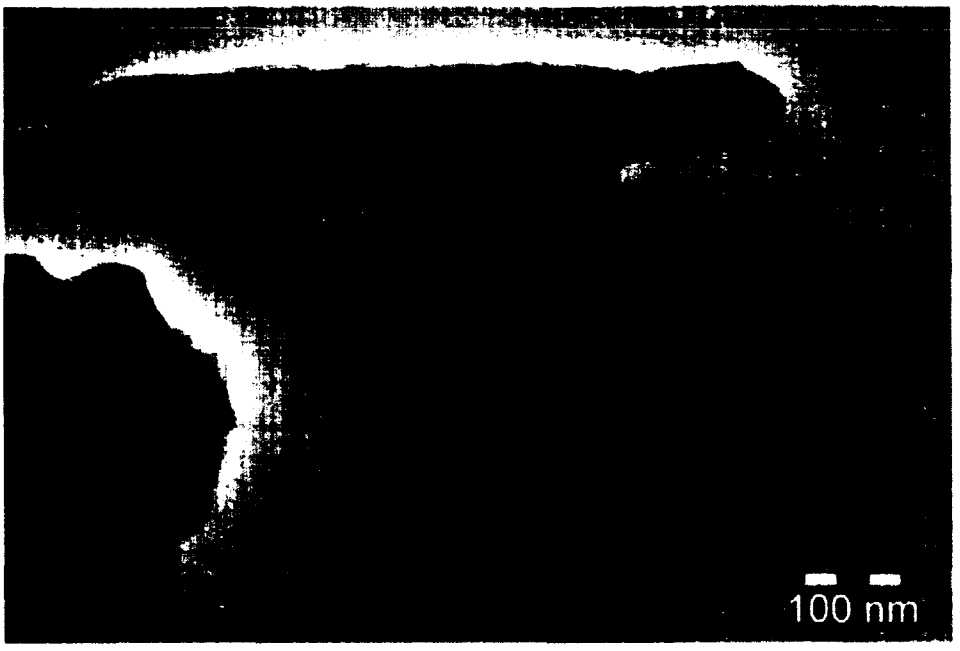

Figure 3- 9: TEM of barium coated halloysite nanotubes.

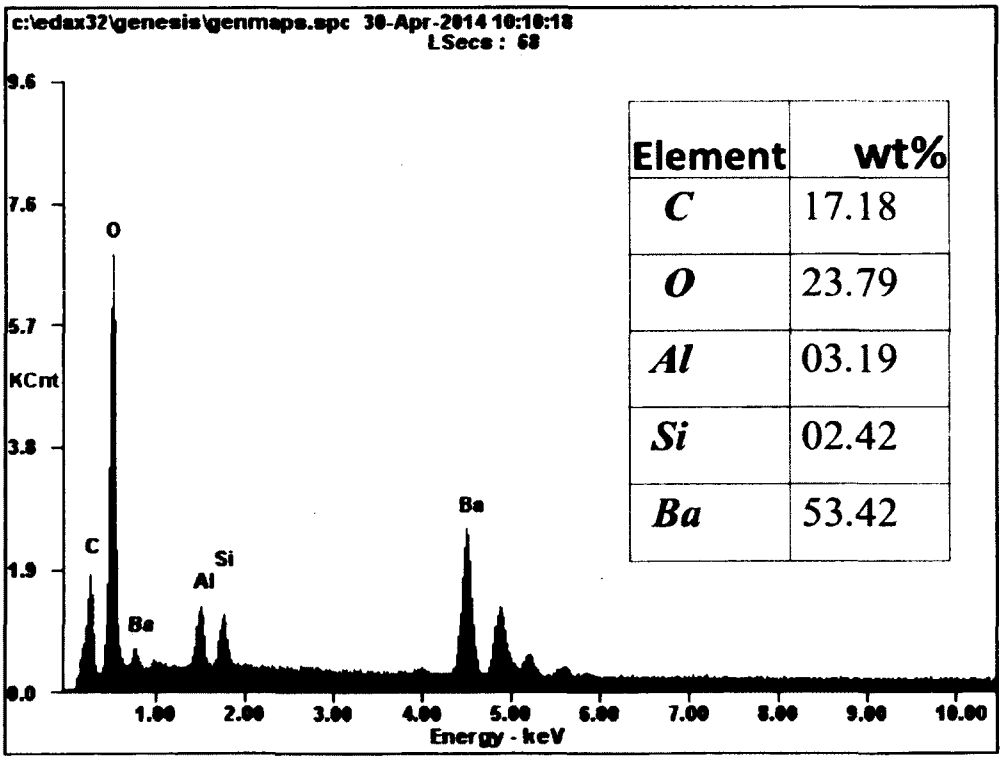

Figure 3- 10: EDAX of barium coated halloysite nanotubes.

Barium proved to bond tightly along the body of the nanotube, which can be seen in both the SEM and TEM images. Further, the EDAX shows two primary resonance peaks for barium. As barium is a common contrast agent in the medical field for X-rays, the ability to create tubes coated with contrasting agent is potentially of great value in medical use.

3.5.1.4 *Copper Coated Halloysite Nanotubes*

Copper acetylacetonate was mixed in 100 mg batches 1:1 with halloysite nanotubes and sintered at 300 °C. SEM, TEM, and EDAX were performed to ensure coating had taken place, and are shown in Figures 3-11, 3-12, and 3-13, respectively.

Figure 3- 11: SEM of copper coated halloysite nanotubes.

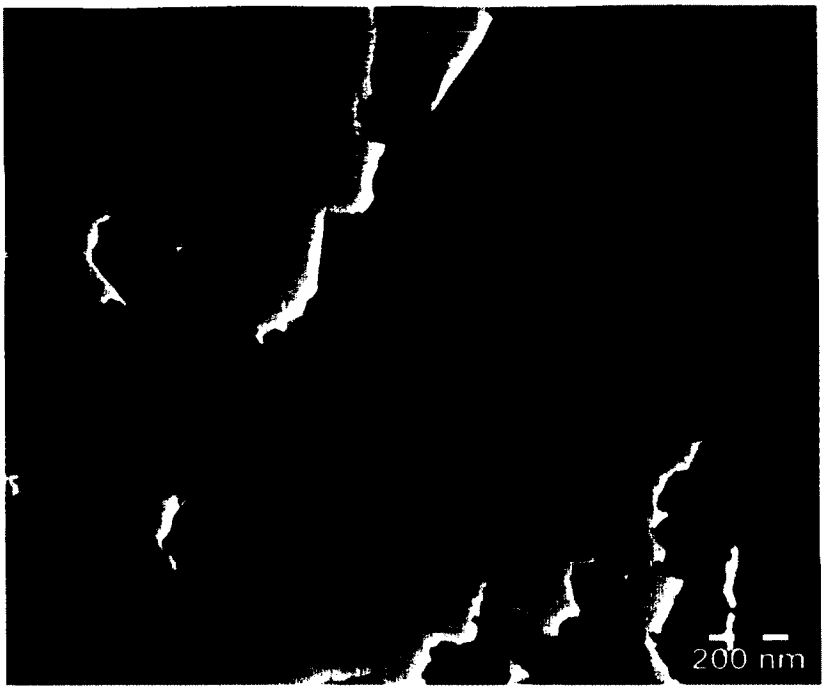

Figure 3- 12: TEM of copper coated halloysite nanotubes.

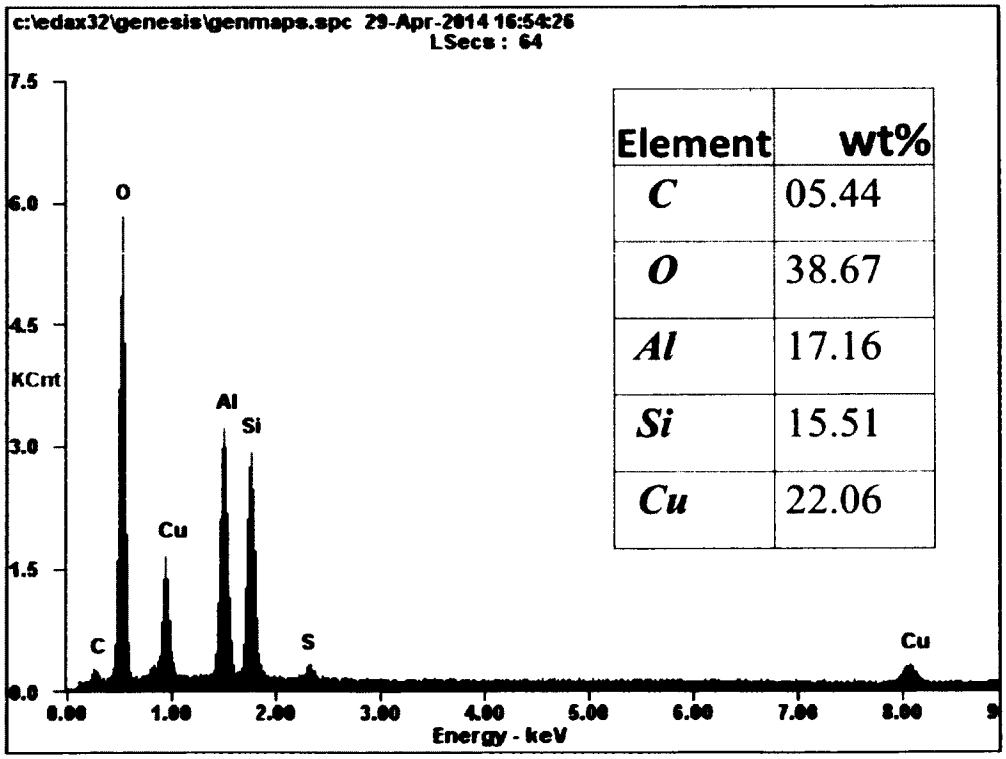

Figure 3- 13: EDAX of copper coated halloysite nanotubes.

Here, TEM and EDAX confirm the presence of copper, however it is difficult to visually confirm the copper in the SEM. The copper coating bonded similarly to the iron; that is, it preferentially bonded in irregular clumps along the surface of the tube. Unlike the iron, it showed no preference in specific bonding places along the body of the tubes, and sheet coatings were obtained on many of the imaged nanotubes.

3.5.1.5 *Nickel Coated Halloysite Nanotubes*

To create a nickel coating on the halloysite, nickel acetylacetonate was mixed 1:1 with halloysite in 100 mg batches. SEM, TEM, and EDAX were performed to confirm the sintering and coating of the nickel onto the halloysite, and is shown in Figures 3-14, 3-15, and 3-16, respectively.

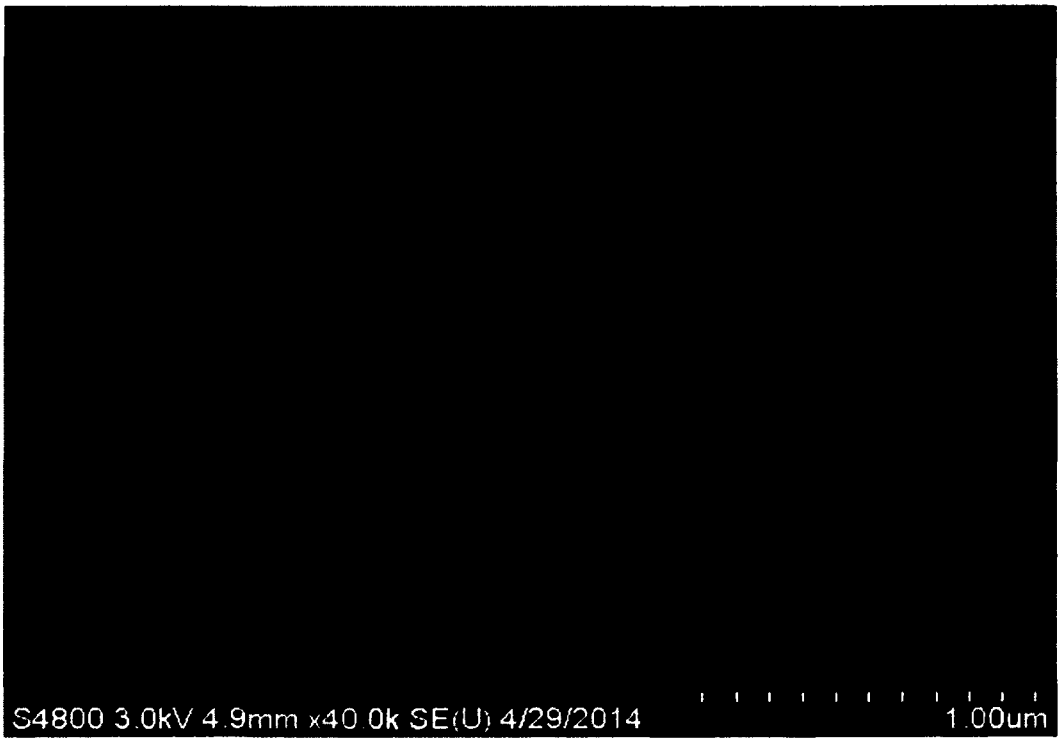

Figure 3- 14: SEM of nickel coated halloysite nanotubes.

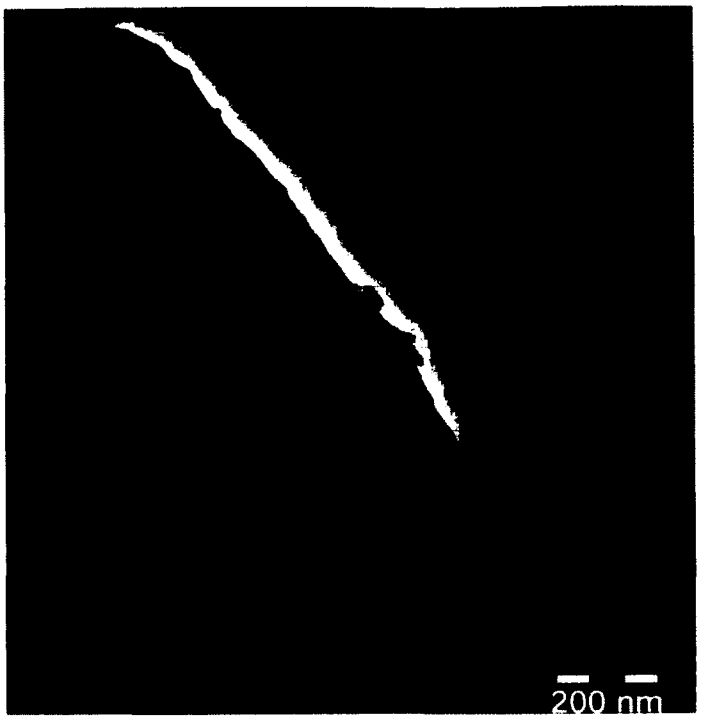

Figure 3- 15: TEM of nickel coated halloysite nanotubes.

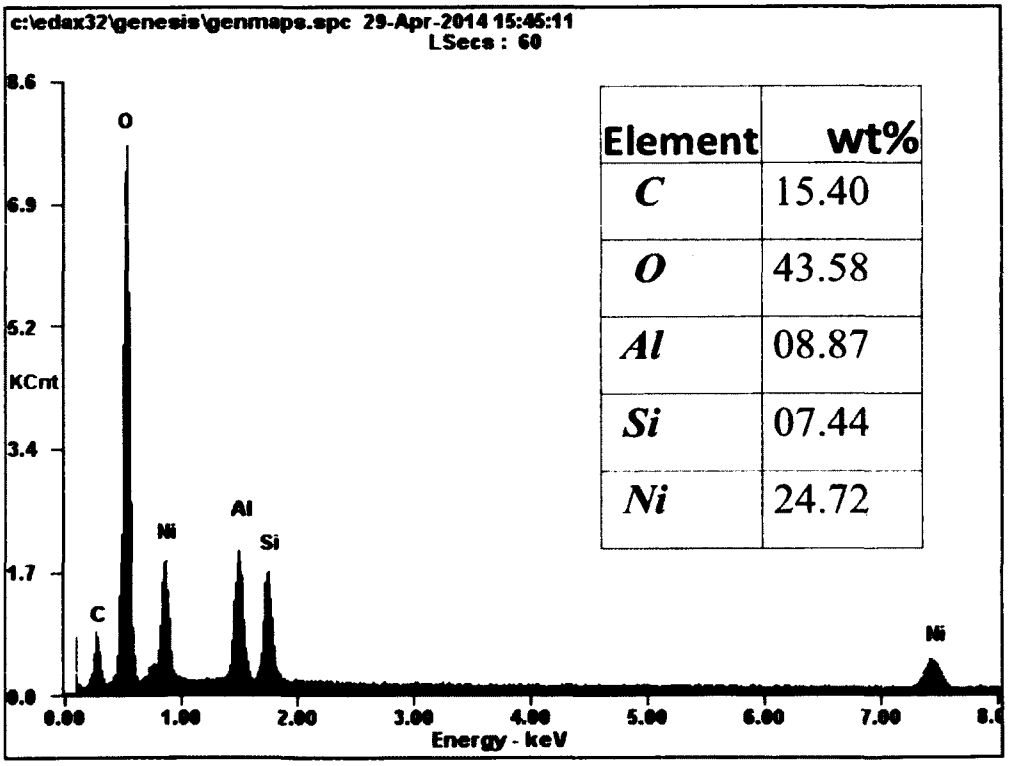

Figure 3- 16: EDAX of nickel coated halloysite nanotubes.

From the above testing, the nickel presence was confirmed. The nickel tended to bond closely along the body of the tube, resulting in a less transparent nanotube with apparent small spheres of nickel observed in the TEM.

3.5.1.6 *Lithium Coated Halloysite Nanotubes*

Lithium acetylacetonate was mixed 1:1 with halloysite nanotubes in 100 mg batches and sintered at 300 °C. SEM, TEM, and EDAX were performed, and are shown in Figures 3-17, 3-18, and 3-19, respectively.

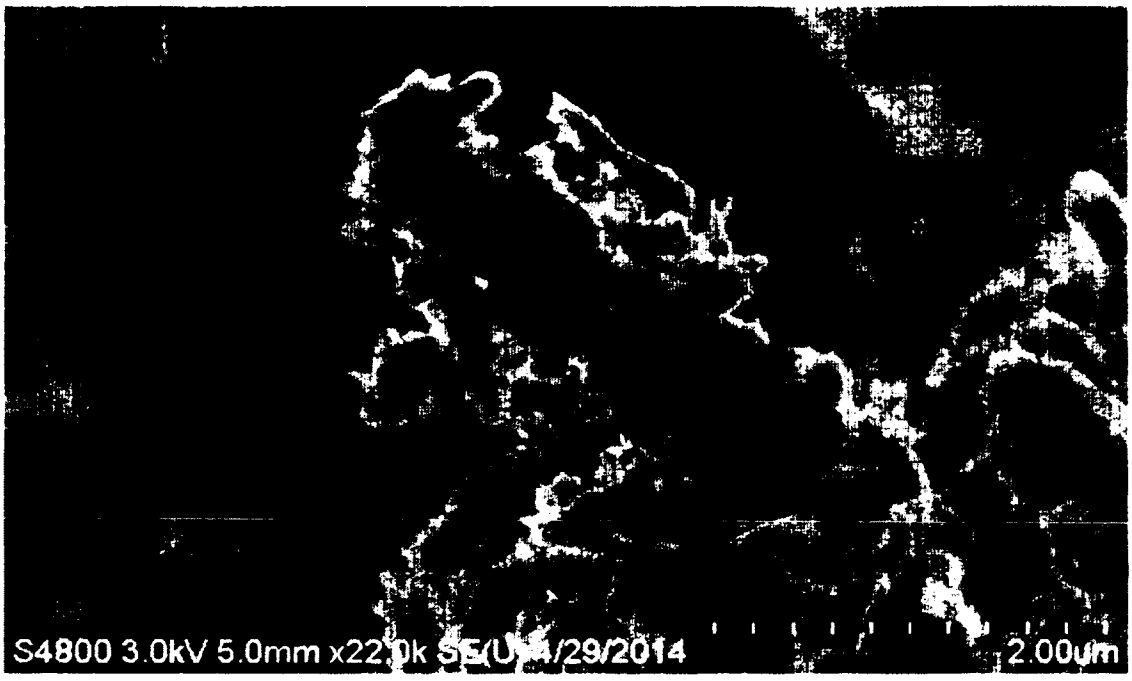

Figure 3- 17: SEM lithium coated halloysite nanotubes.

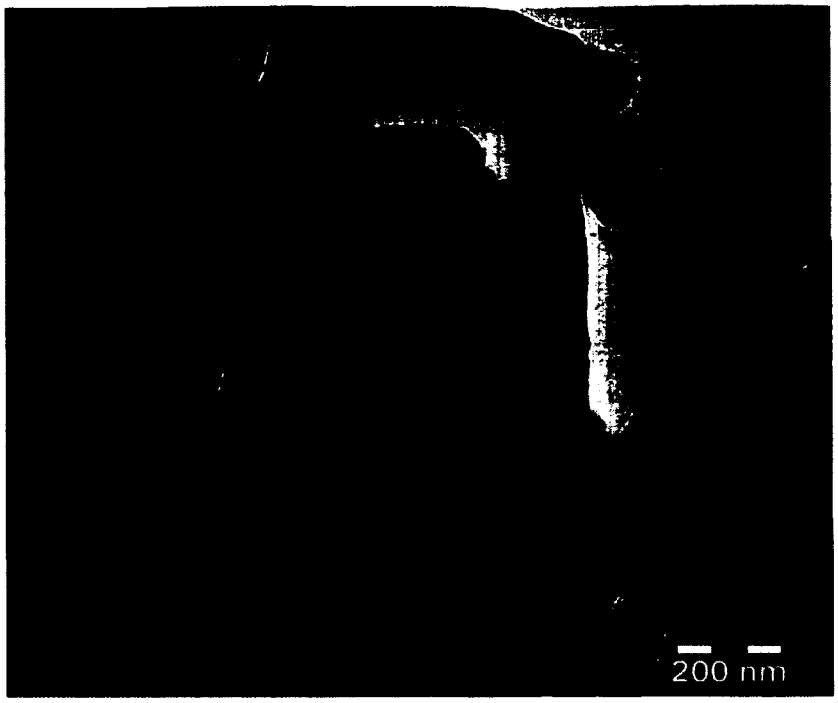

Figure 3- 18: TEM lithium coated halloysite nanotubes.

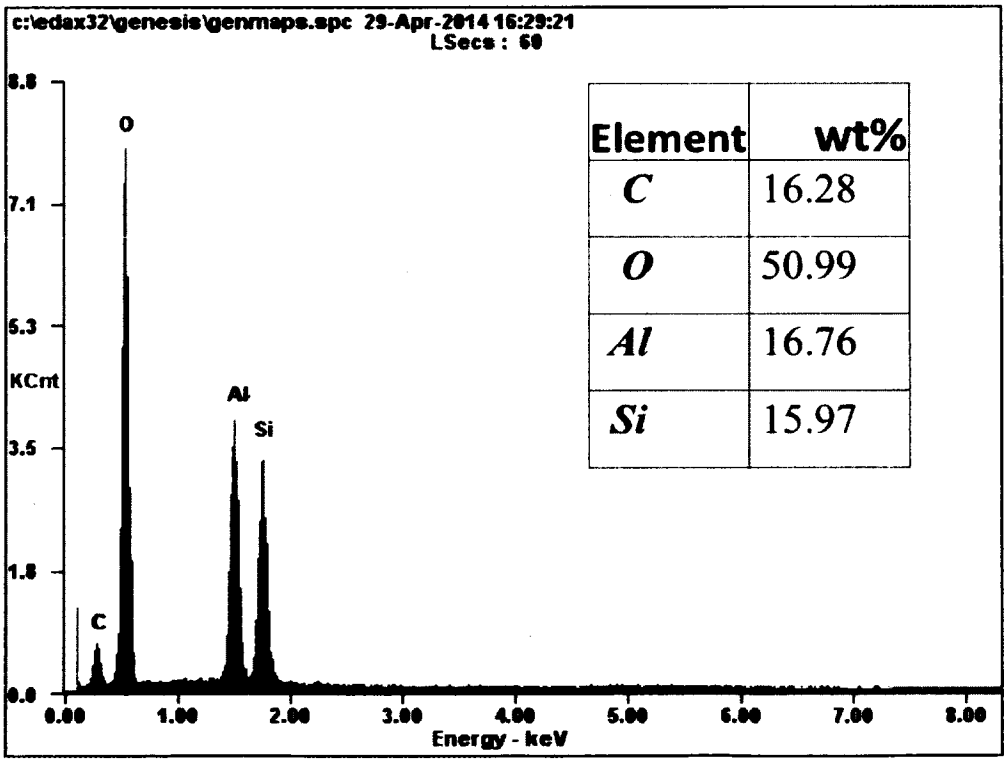

Figure 3- 19: EDAX lithium coated halloysite nanotubes.

Lithium is an extremely light element, lighter than the silicon, aluminum, and oxygen found in the halloysite. Visually, the presence of lithium can be confirmed in both the SEM and TEM. For the SEM, we notice irregular clumping in what appears to be a somewhat crystalline fashion, which would coincide with lithium's crystalline bonding patterns with itself. The TEM shows multiple halloysite nanotubes bonded together by the lithium that has sintered to itself, building a crystalline bond after initial layers of lithium bonded to the surface of the halloysite. EDAX was unable to confirm the presence of the lithium as the particular EDAX system used utilizes a beryllium lens for filtering the signal. As such, the beryllium lens will filter signals from light elements (hydrogen, helium, lithium, and beryllium) and is only reliable for elements heavier than beryllium.

3.5.1.7 *Gold Coated Halloysite Nanotubes*

Coating the halloysite in gold required a different approach. There is no commercially available gold acetylacetonate, so the compound decided upon was gold acetate. The initial attempt to sinter the gold was performed at 300 °C, however gold acetate has a violent reaction when heated, leading to an explosion of gold dust in the oven. As such, successive runs were performed to minimize this explosion and maximize the amount of gold left to react with the halloysite. Temperatures between 200-210 °C were found to reduce the explosive tendency to an acceptable level while still allowing the sintering to occur. Temperatures below this threshold did not achieve full reaction, leaving unreacted gold acetate in the sample. Shown in Figure 3-20 is a sample of gold acetate sintered at 250 °C.

Figure 3- 20: Gold acetate and halloysite nanotubes sintered at 250 °C.

Once the reaction has occurred at these high temperatures, the heavy gold ions in the air fall back down, coating the exterior of the container. Further, samples sintered around 200 °C proved to be tightly bonded together due to the ductile nature of the gold and the preferential bonding nature of gold nanoparticles to bond more readily to themselves than to any other surface. Once samples were obtained, SEM, TEM, and EDAX were performed and are shown in Figures 3-21, 3-22 and 3-23, and 3-24, respectively.

Figure 3- 21: SEM of gold coated halloysite nanotubes sintered at 200 °C.

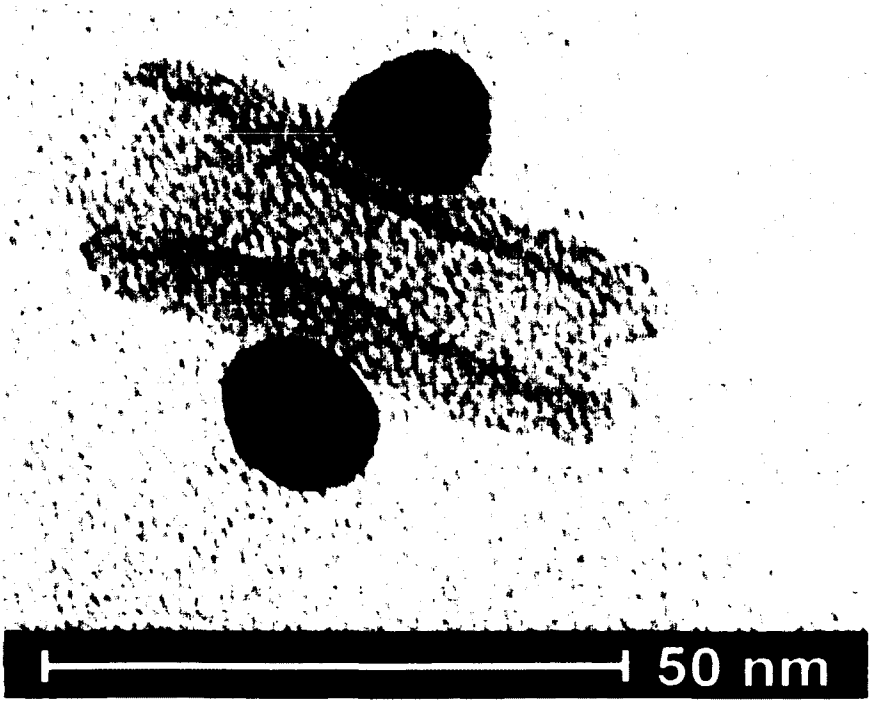

Figure 3- 22: TEM of gold coated halloysite nanotubes sintered at 200 °C.

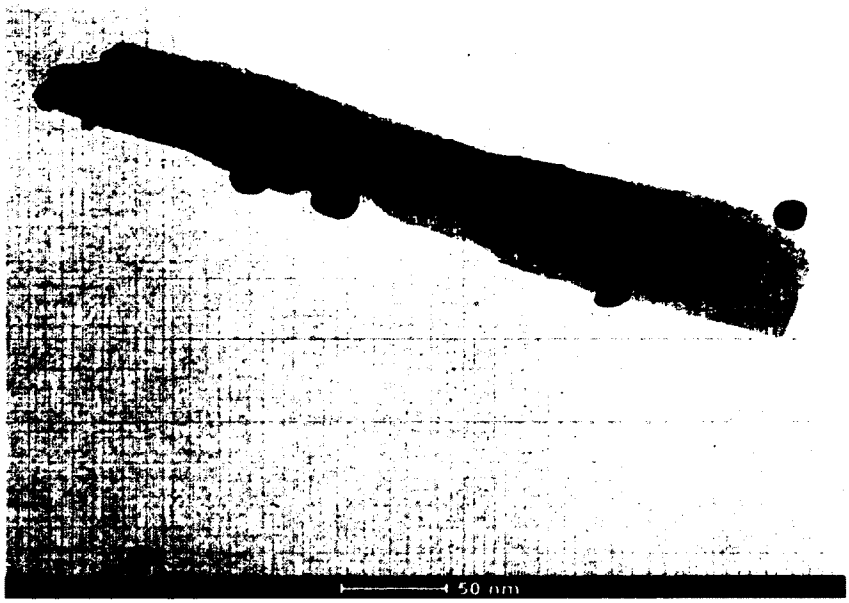

Figure 3- 23: TEM of gold coated halloysite nanotubes sintered at 200 °C.

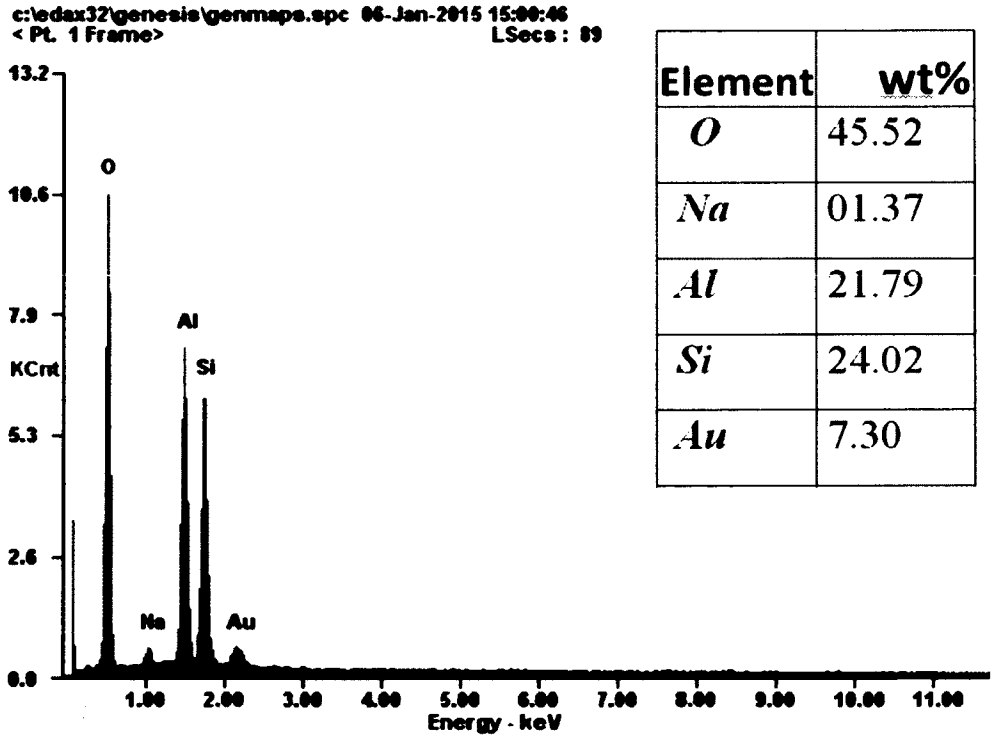

Element	wt%
O	45.52
Na	01.37
Al	21.79
Si	24.02
Au	7.30

Figure 3- 24: EDAX of gold coated halloysite nanotubes sintered at 200 °C.

As discussed before, gold nanoparticles preferentially to themselves than with any other surfaces. This is evident in the SEM and two TEM images above that show gold seeds on the surface of the nanotubes. Further, the EDAX confirmed the presence of gold on the surface of the nanotube. A sodium contamination peak was obtained and is attributed to a precursor material used to manufacture the gold acetate as it was present in all samples run using the gold acetate.. Gold coatings on halloysite are of particular interest to the medical community as gold nanoparticles are currently under study for their laser resonance properties, specifically for tumor treatment and hyperthermia.

3.5.2 Multiple Metal Coating of Halloysite Nanotubes

To have a tunable, modular platform, it was desired to test the viability of this method to coat a sample of halloysite nanotubes with multiple metals to test retention of both coatings. Iron and gold were chosen as these metals have two easy properties to test, and had distinct bonding formations that would visually confirm whether the elements bonded to the nanotubes or not. Iron (III) acetylacetonate was used for the iron deposition to test whether magnetic properties were retained and gold acetate for the gold deposition. The iron was deposited first through a 100 mg 1:1 batch of iron (III) acetylacetonate to halloysite, then sintered in the Vulcan oven at 300 °C. Once the sintering was done, the resulting sample was ground in a mortar and pestle, then mixed with 100 mg of gold acetate via vortexing. The resulting mixture was then sintered at 200 °C and ground in a mortar and pestle to overcome clumping. The resulting mixture showed the same magnetic properties as the iron coated halloysite. For imaging

confirmation, only TEM and EDAX were run due SEM concerns to the magnetic nature of the iron particles. TEM is shown in Figure 3-25 and EDAX in Figure 3-26.

Figure 3- 25: TEM of iron/gold dual coated halloysite nanotubes.

Visually, the lighter fuzzy clumps are the iron particles and the darker spheres are the gold particles. Upon testing, the halloysite retained the magnetic properties of the iron coated halloysite.

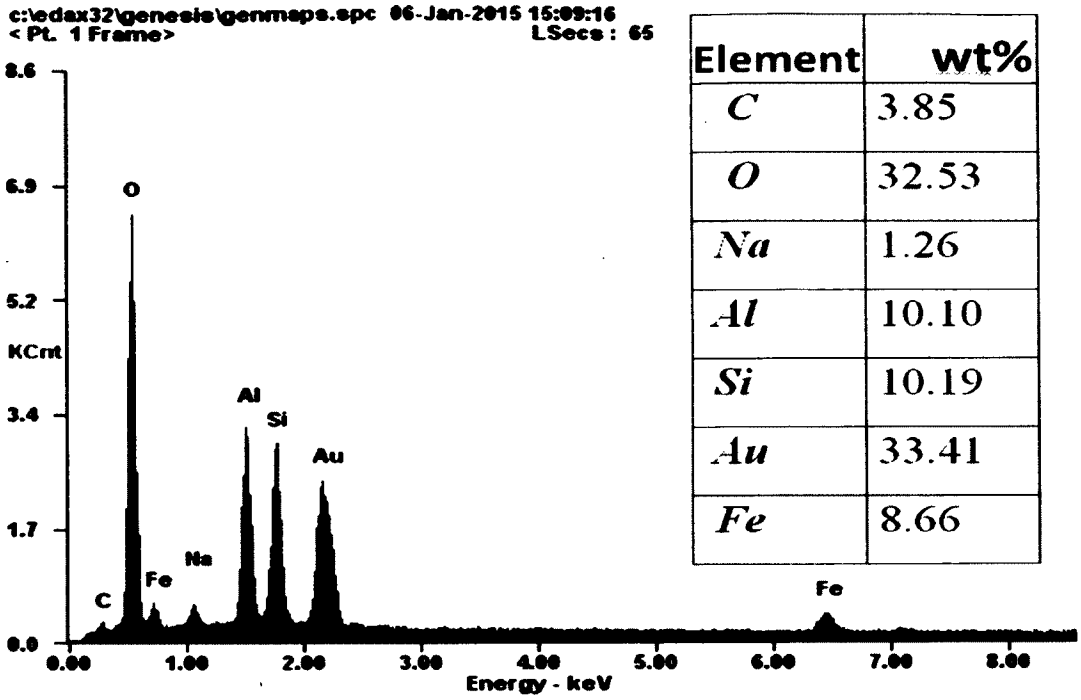

Element	wt%
C	3.85
O	32.53
Na	1.26
Al	10.10
Si	10.19
Au	33.41
Fe	8.66

Figure 3- 26: EDAX of iron/gold dual coated halloysite nanotubes.

The EDAX shows that all desired elements are present while also maintaining the sodium contamination peak.

3.5.3 Magnetic Characterization

The iron coating of halloysites potentially enabled a magnetic response to be achieved. To characterize this, three tests were performed. First, the sample magnetized for 72 hours, and a measurement using a DC Guassmeter was performed. Second, The sample was tested using an alternating gradient magnetometer (AGM) to test for the hysteresis curve. Finally, to confirm the hysteresis results, multiple batches of differing iron coated halloysites were fabricated with successively more iron and the samples were tested using a vibrating sample magnetometer (VSM) for their respective hysteresis curves.

3.5.3.1 *DC Gaussmeter Testing*

Initial characterization of the magnetic nature of the halloysite nanotubes was performed using a sample of iron (III) acetylacetonate sintered halloysite created in a 250 mg 1:1 batch. The sample was then ground to ensure minimal clumping of the sample, placed on a borosilicate glass slide, then subjected to constant magnetization for 72 hours. The magnet used was measured using an AlphaLab DC Gaussmeter, Model 1-ST. The magnetic field was tested at a 5mm, 2mm, and 0.5 mm standoff, and found to be 1650±30 G, 4000±50 G, and 5350±45 G, respectively. After the 72 hour exposure, the sample was tested at the same distances once the magnet was removed. The sample was found to retain a magnetic field of 50±3 G at a 5 mm standoff, 98±8 G at a 2 mm standoff, and 227±5 G at a 0.5 mm standoff.

3.5.3.2 *AGM Testing*

Further characterization was performed using a Princeton Measurements Corporation MicroMag Alternating Gradient Magnetometer (AGM) on samples prepared as previously described above. For characterization, 10 μg were placed on Kapton tape, then applied to the probe and the program was run. The AGM used was constrained to ±10,000 Oe, a relatively low magnetic field for such a small sample size. Shown in Figure 3-27 is the hysteresis curve obtained.

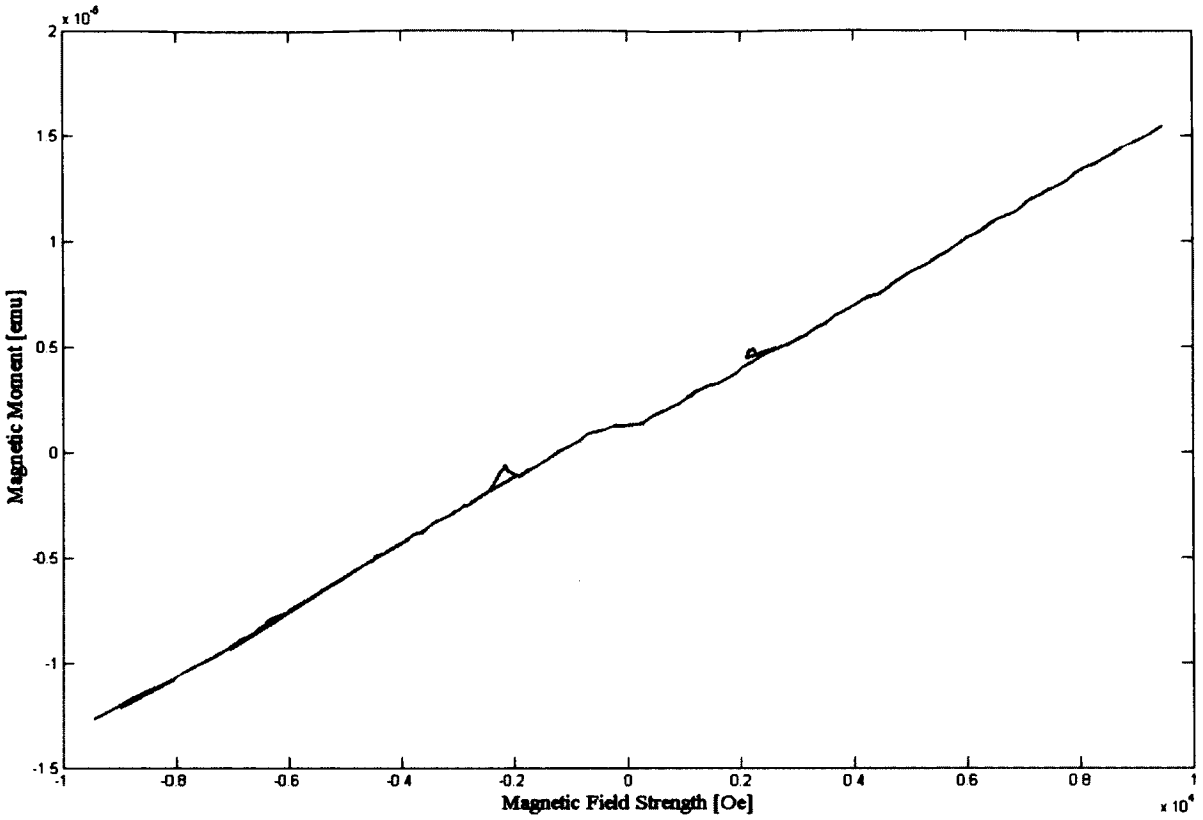

Figure 3- 27: AGM hysteresis curve for iron coated halloysite.

This curve showed to be relatively linear. This is attributed to the small amount of sample; the halloysite is nonmagnetic, and as such only the iron coating the halloysite shows results. Given this, only part of the overall sample that was constrained to 10 μg was able to be magnetized, and thus a small but distinct hysteresis curve was obtained. This curve would scale up given greater amounts of sample, and would trend towards a more traditional hysteresis curve. The offset from the origin is due to the prior magnetization of the sample, leading to a measured magnetic field without external fields applied.

3.5.3.3 *VSM Testing*

To obtain a greater characterization of the iron coated halloysite, additional testing was done using a vibrating sample magnetometer at Grambling. For this testing, amounts of material around 0.12 ± 0.02 grams are used. Once measured, they are placed in a glass container and affixed to the end of a glass rod. This is then placed between two large magnets and tested for vibration between +10000 G and -10000. For this testing, 99 point of interest were run. As the machine gets closer to zero, more points are used to examine potential ferromagnetic nature of the material. This characterization is preferable to the AGM for bulk material testing due to the increase in sample size.

Initial data was taken for raw halloysite and raw iron acetylacetonate. Shown in Figures 3-28 and 3-29 are the respective data for these two sets of material. A small hysteresis curve can be seen for the halloysite. Additionally, the halloysite proved to retain some inherent magnetization from the measuring process, as shown by the offset from the origin and the separation of the hysteresis lines. The iron acetylacetonate was seen to have a linear magnetization as the magnetic field increases, as is expected for elemental iron with no retention of magnetization from the brief exposure to the magnetic field.

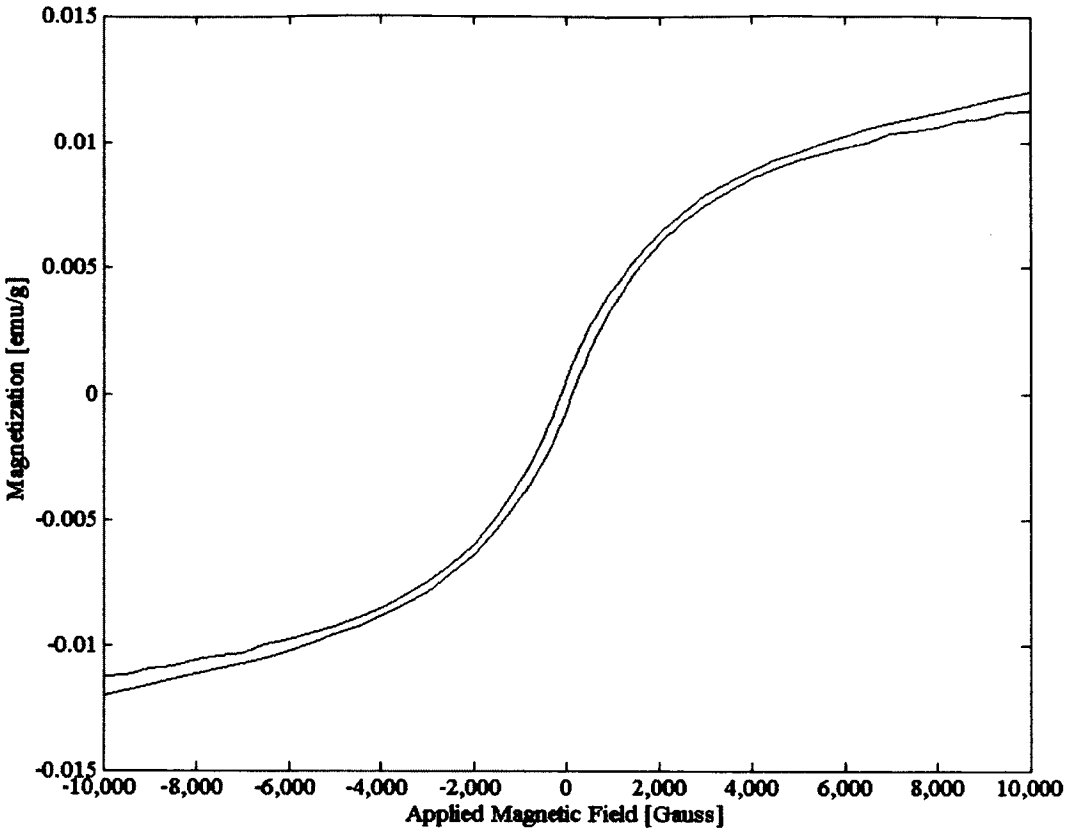

Figure 3- 28: VSM for raw halloysite.

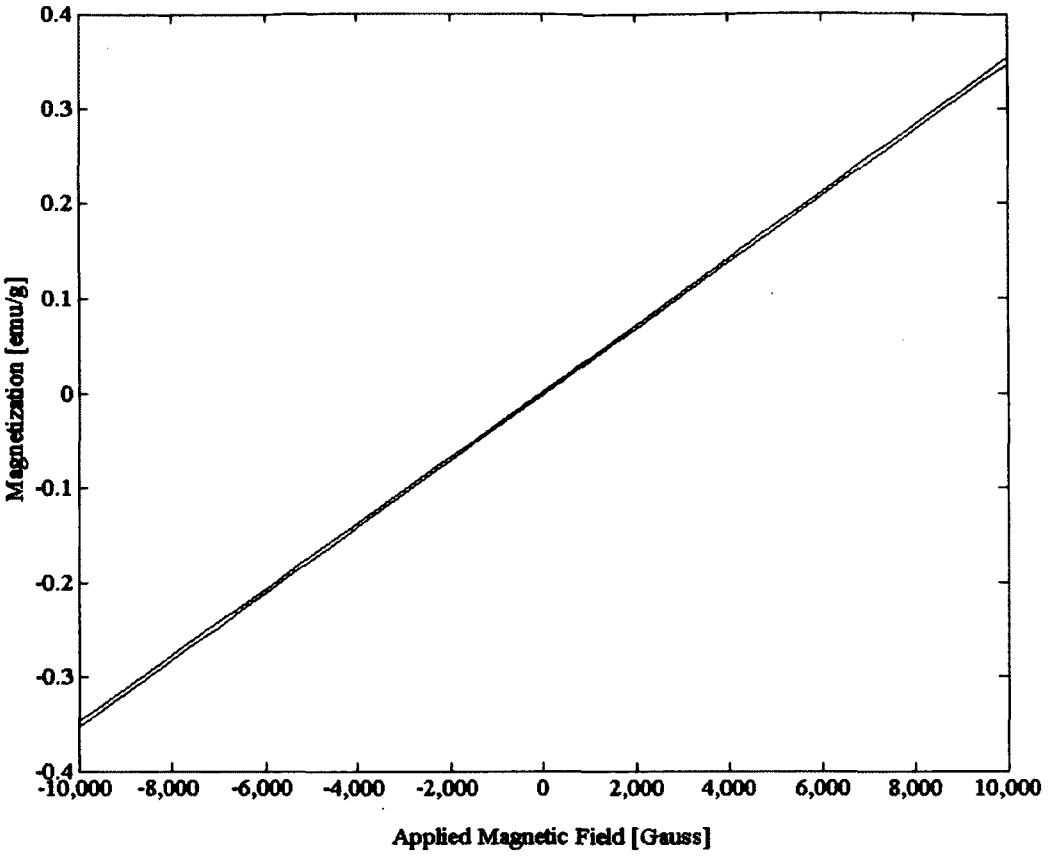

Figure 3- 29: VSM for iron acetylacetonate.

For the iron coated testing, multiple samples of iron coated halloysite were fabricated using different amounts of iron acetylacetonate. The basis for these ratios is 250 mg of halloysite that was used in all sample batches. Weights were prepared in ratios of (iron acetylacetonate: halloysite nanotubes) 0.5:1, 1:1, 1.5:1, 2:1, 2.5:1, and 3:1. Once combined, the samples were vortexed for even dispersion, placed in 10 mL glass beakers, and cooked at 300 °C for 4 hours. To minimize any loss of additive through potential out gassing, glass slides were placed over the samples. Shown in Figure 3-30 are the curves obtained.

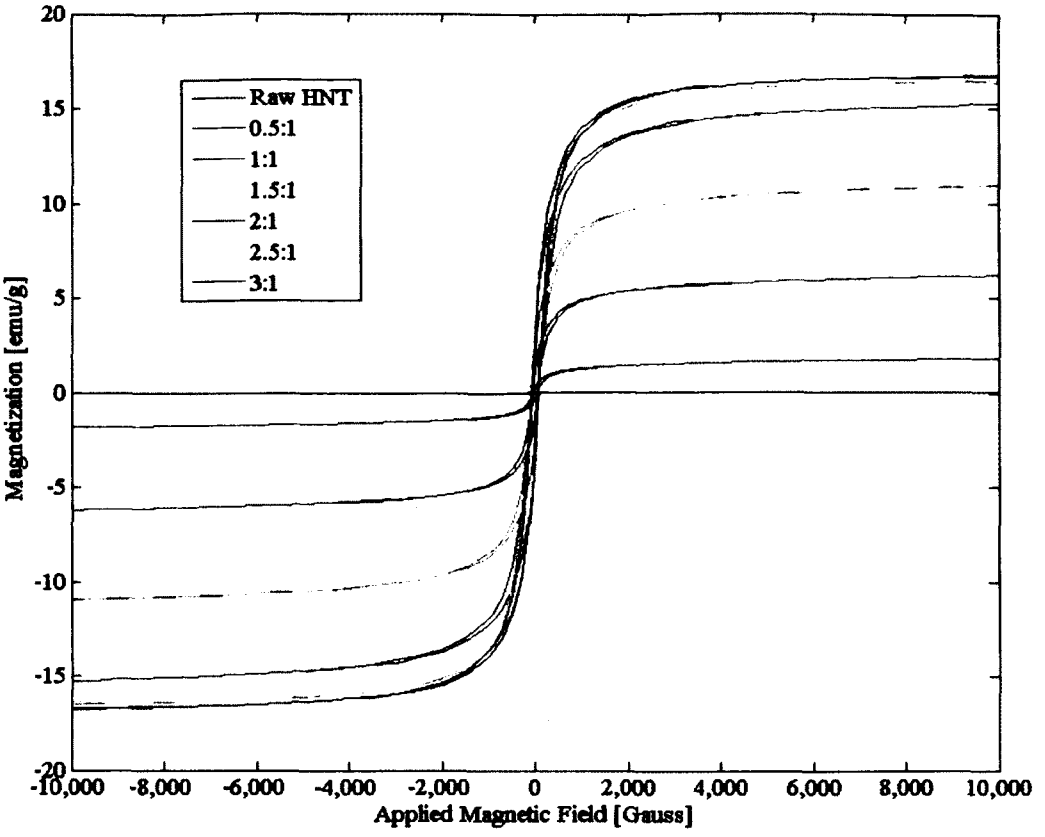

Figure 3- 30: VSM curves for varying levels of iron coated halloysite.

As the sample is prepared with more iron, a higher magnetization of the sample can be observed. At higher ratios of iron acetylacetonate to halloysite, the curves become very similar, suggesting a saturation point is reached around 2.5:1-3:1 iron acetylacetonate: halloysite nanotubes. This is most likely due to unreacted iron acetylacetonate powder in the sample and the low amount of active sites for the iron to bind to on the halloysite.

3.5.4 CT Scan Characterization of Barium Coated Halloysite

Barium is commonly used as a contrast agent in biomedical imaging technologies due to its high absorption coefficient in the energy ranges characteristic to medical grade isotopes. Halloysite nanotubes have been shown to increase the mechanical properties of

biomaterials such as PMMA bone cements, however these bone cements necessitate the addition of barium sulfate into the polymer mixture during curing if opacity of the part is desired [111]. Because the bonding of the barium onto the surface of the nanotubes is a tight sheath, the addition of barium coated halloysites into the PMMA mixture was tested to see if opacity of the sample could be achieved at a sufficiently high enough level so as to remove the need for barium sulfate added into the mixture. Shown in Figure 3-31 are the two sets of structures cast in commercial grade bone cement: the first enhanced with uncoated halloysite, and the second enhanced with barium coated halloysite.

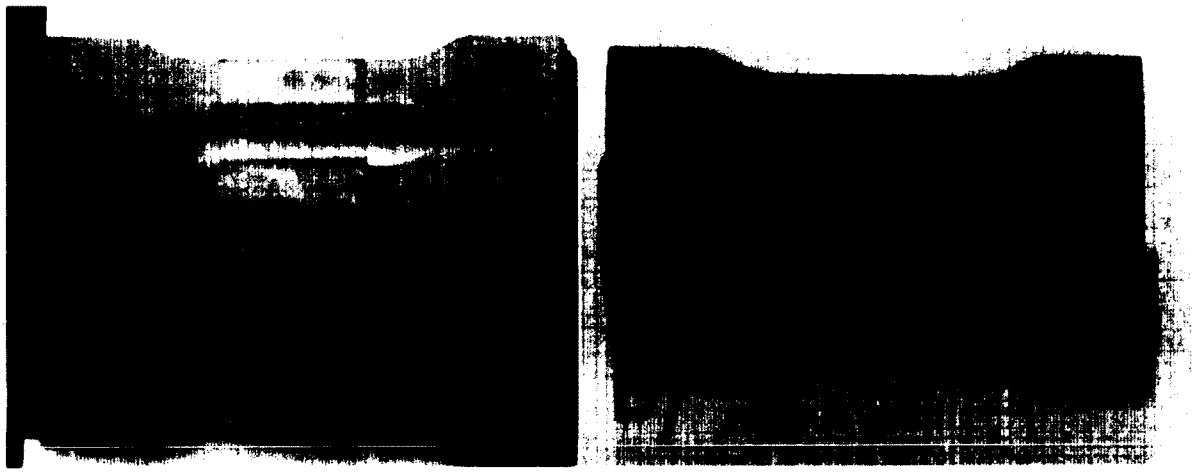

Figure 3- 31: A) Halloysite nanotube enhanced PMMMA bone cement, B) Barium coated halloysite nanotube enhanced PMMA bone cement.

For control, three different commercially available bone cements were tested for comparison of contrast: a low viscosity barium sulfate-added PMMA/MMA bone cement, a high viscosity barium sulfate-added PMMA/MMA bone cement, and a PMMA only bone cement with no barium sulfate added. The halloysite and barium coated halloysite were added to the PMMA only mixture to test the increase in contrast. A CT three-dimensional scan was performed on a 30 mm long rectangular bar sample of each

bone cement with the machine set at 120 kV. Fifty to one hundred 1 mm point regions of interest (ROI) were calculated during the scan for each sample for contrast in Hounsfield units (HU), a common unit used in medical imaging to describe the opacity of a material. Figure 3-32 shows the resulting averaged contrast of all samples tested.

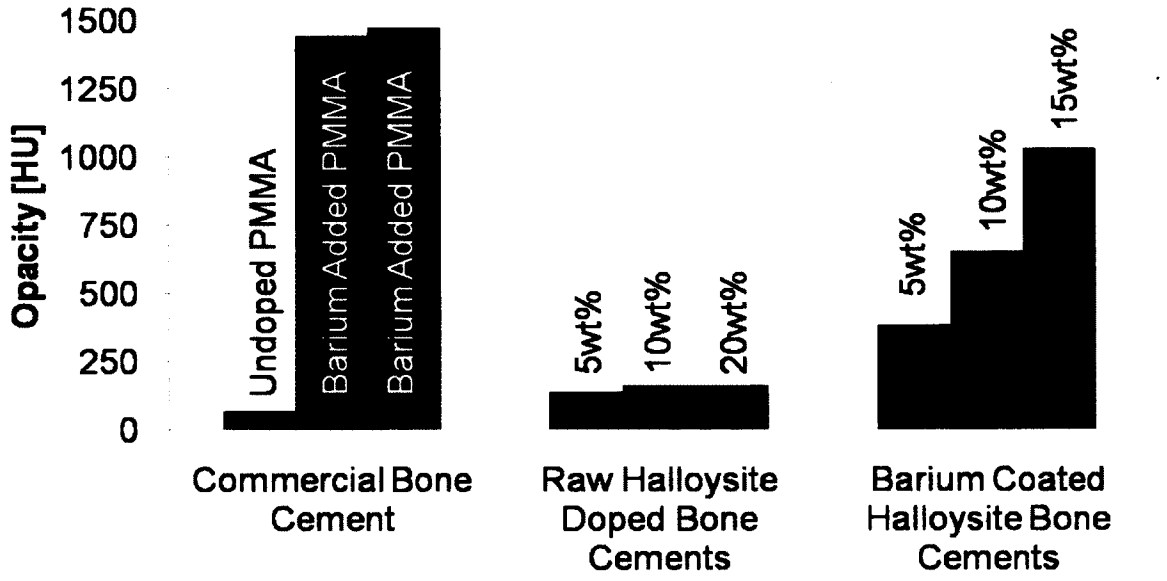

Figure 3-32: Opacity of commercial bone cement, raw halloysite doped bone cement, and barium coated halloysite doped bone cement.

The PMMA only bone cement proved to have very little contrast as compared to the barium sulfate-enhanced bone cements. While previous literature has shown that halloysite is capable of increasing the mechanical properties of bone cement, the opacity achieved for 5wt%, 10wt%, and 20wt% of halloysite barely increases the contrast of the mixture as compared to cements doped with barium sulfate. In contrast, 15wt% of barium coated halloysite brought the PMMA only bone cement from 68 HU to 1029 HU, an increase of 15.1 time the undoped level. Further, 15wt% halloysite achieved 70%

contrast of commercially available bone cement that only used barium sulfate as an additive. Each 5wt% doping of barium coated halloysite increased the contrast by about 300 HU. It should be noted that the barium used were fabricated in a 1:1 ratio of barium acetylacetonate dihydrate to halloysite, and that additional contrast could be achieved by sintering the halloysite with additional barium to achieve thicker coatings.

3.5.5 Laser Resonance Characterization of Iron, Gold, and Iron/Gold Coated Halloysite

Gold nanoparticles are currently being researched for biomedical therapies for their laser resonances. Because the gold coating onto the halloysite showed to form small clusters of gold, laser resonance was tested of these halloysites along with the iron/gold dual coat for a magnetically stationary laser resonance platform. For this testing, two lasers of 532 nm and 808 nm wavelengths were chosen with powers of 20 mW and 2 W, respectively. Gold nanoparticles have a strong resonance peak at 532 nm, and a local maximum at around 808 nm. 808 nm lasers are currently used in laser therapies due to a transmission window in living tissue that allows 808 nm wavelengths to pass through into deep tissues. Because the iron/gold dual coat was tested for laser resonance, the iron coated halloysite was also tested for its resonance at these values as a control along with raw halloysite. The samples were prepared in 1:1 batches as described above, and mortar and pestle ground after sintering.

3.5.5.1 *Laser Wavelength Characterization*

Prior to testing, both lasers were characterized using an OceanOptics USB4000 Fiber Optic Light Spectrometer (360-1000 nm) combined with the Overture processing software. For the setup, the laser was focused on the tip of the fiber optic cable, then the

measurements were taken after 1 minute to ensure filtering of background light via the software. Shown in Figure 3-33 is the spectrum for the 532 nm laser, and in Figure 3-34 the spectrum for the 808 nm laser at 2 W.

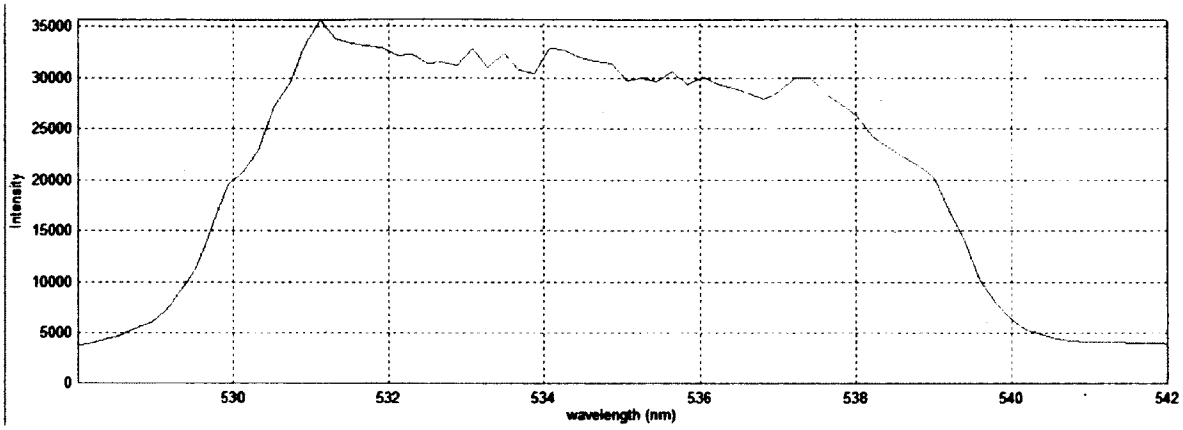

Figure 3- 33: Spectrum for 20 mW 532 nm laser.

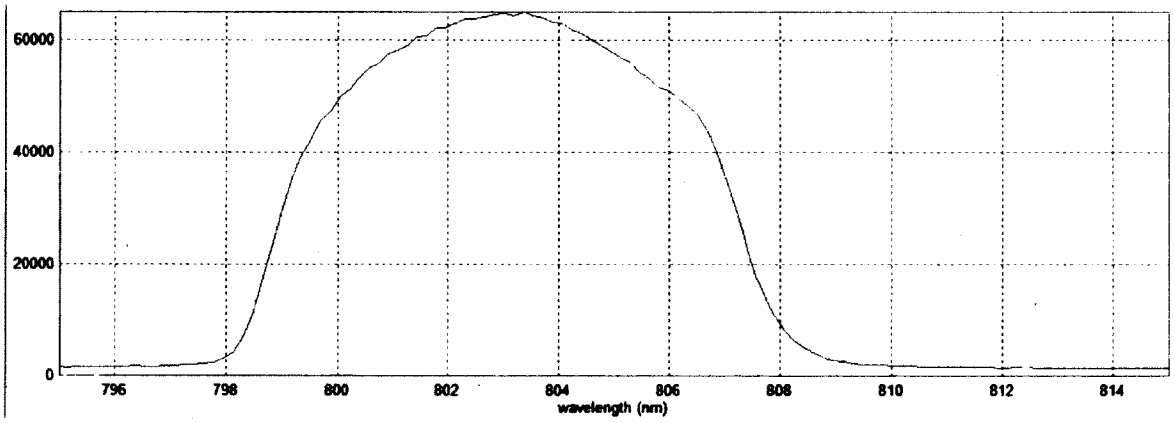

Figure 3- 34: Spectrum for 2 W 808 nm laser.

From these measurements, the lasers are classified to their given wavelength bands. The 532 nm laser was found to have a variance of 534 ± 6 nm, and the 808 nm was found to have a variance of 803±5 nm.

3.5.5.2 *Laser Resonance of Dry Samples*

The first laser resonance test was performed on dry samples. Each group was placed in a clean 10 mL borosilicate glass beaker with a thermocouple taped to the bottom. Background temperature was recorded, then the sample was exposed the laser for 5 minutes. At 5 minutes, the final temperature was recorded. Shown in Table 3-1 are the results for the 532 nm laser.

Table 3- 1: Initial and final temperatures for halloysite exposed to 532 nm laser for 5 minutes.

	T_o (°C)	T_f (°C)	ΔT (°C)
Raw HNT	23.3	23.3	0
Iron HNT	23.3	23.5	0.2
Gold HNT	22.8	24.0	1.2
Iron/Gold HNT	22.5	22.7	0.2

For this test, the gold coated halloysite showed a stronger response than any other coating with a 1.25 °C increase in temperature. The raw halloysite, white in color, completely reflected the laser, and thus experienced no heating. The dark color of the iron led to the second highest change in temperature, though it was only 0.2 °C. The lack of greater heating of the iron/gold dual coat could be attributed to only a small amount of gold having been deposited as compared to the larger amount of iron. New samples of each batch were created, then exposed to the 808 nm laser as shown in Table 3-2.

Table 3- 2: Temperatures for halloysite exposed to 808 nm laser for 5 minutes.

	T_o (°C)	T_f (°C)	ΔT (°C)
Raw HNT	22.7	27.1	4.4
Iron HNT	22.8	38.8	16.0
Gold HNT	22.9	41.7	18.8
Iron/Gold HNT	22.7	39.0	16.3

The 808 nm laser was 100 times more powerful than the 532 nm laser, leading to increased heating in all samples. The raw halloysite still experienced the least amount of heating among the batches, with only a 4.4 °C increase. The iron showed a full 16 °C gain in temperature, attributed to the dark color of the tubes absorbing the laser. The iron/gold dual coat showed a greater increase than the raw iron with 16.3 °C gained, and this again can be attributed to gold being present, but in a small amount. Finally, the gold coating experienced the greatest increase at 18.8 °C, however the temperature peaked at 44.5 °C at 4 minutes then slowly decreased down to the final temperature. This gain then decrease can be attributed to complete resonance with the laser and potential ablation of the gold coated halloysites.

3.5.5.3 *Laser Resonance of Wet Samples*

To better test the response of the coated halloysite, laser resonance was done on 10 mg samples placed in 10 mL of deionized water. The samples were agitated via stirring, then exposed to the laser for 1 minute to ensure suspension of particles during the testing. The 532 nm laser proved too weak in power to generate significant heating. Testing with the 808 nm laser yielded appreciable results due to the greater power of the laser. The laser was again used at 2 W to compare to the dry powder testing. Shown in Table 3-3 are the obtained results for this testing.

Table 3-3: Temperatures for halloysite exposed to 2W 808 nm laser for 1 minute.

	T_o (°C)	T_f (°C)	ΔT (°C)
Water	22.6	23.2	0.6
Raw HNT	23.9	24.5	0.6
Iron HNT	24.4	26.4	2.0
Gold HNT	24.0	27.8	3.8
Iron/Gold HNT	23.7	25.5	1.8

Testing was first performed on deionized water with no sample in it to get a baseline of heating attributed to solely to the laser. To this end, it was found over the course of a minute that the water was heated 0.6 °C. Raw halloysite proved to have the same heating over the course of a minute, and this is attributed to reflection and scattering of the laser from the halloysite. Iron coated halloysite proved to heat 2 °C during the one minute testing time. Iron/gold showed a heating of 1.8 °C, slightly less than the iron coated, however this sample clumped significantly more than any other sample. Gold again showed the greatest heating of the batch, achieving a 3.8 °C increase. During this testing, only increases in temperature were observed unlike the dry powder testing.

3.6 Conclusion

A modular method of sintering metal nanoparticles onto the surface of halloysite nanotubes was achieved through the use of metal acetates and metal acetylacetonates. The method proved to work for a variety of compounds, and achieved coatings of iron, barium, copper, nickel, lithium, and gold. This method was confirmed via SEM, TEM, and EDAX. The coated halloysite showed unique properties based upon the coating material. Iron coatings were proven to be magnetically susceptible and retain magnetization after extended exposure to a magnet. Barium coatings proved to add

contrast in MRI imaging of commercially available biomaterials. Gold showed laser resonance in the regimes characteristic to gold nanoparticle research.

The ability to alter the amount of metal coating was also demonstrated by increasing or decreasing the amount of metal acetylacetonate to halloysite nanotubes. A saturation point of iron coating was found to be around 3:1 for iron acetylacetonate: halloysite nanotubes. This was believed to be due to unreacted iron acetylacetonate in the bulk and the lack of present active bonding sites of the halloysite due to saturation

Mixed coatings on the surface of the halloysite nanotubes were also demonstrated. Iron and gold were successively layered onto the surface of the nanotubes, and visual and elemental analysis proved the distinct presence of both elements. Laser resonance was also achieved of the dual coated nanotubes, and found to be greater than that of iron coated tubes, but less than that of gold coated tubes for all three tests performed. This could be overcome by a greater coating of gold onto the nanotubes, however this was not achieved due to a restriction of materials.

Halloysite have proved to be a versatile platform for the deposition of nanoparticles to achieve a variety of characteristics. Further, these can easily be tailored to desired specifications as seen for the iron and the barium doping, and prove compatible with mixed coatings as in the case of the iron/gold coated nanotubes. Myriad uses could be found for these, including use in biomedical fields for target delivery of drugs or resonance of the gold nanoparticles for tumor treatment and use as an opacity agent.

CHAPTER 4

NANOENHANCED FABRICATION METHODS FOR RADIATION SHIELDING

4.1 Introduction

Additive manufacturing and 3D printing provide the potential for easily fabricated custom structures that can achieve desired complex geometries. This chapter demonstrates a method for the introduction of metallic powders into 3D printing filament using off-the-shelf equipment with no modification required. Through this method, custom shielding may be achieved towards low cost housings and disposal shielding for generated wastes, potentially from nuclear fallout.

When first conceived in the 1990's, 3D fabrication was a powder-based laser sintering method used for fabrication of metal and ceramic parts. Because this necessitated the use of large equipment and was rather expensive to run, new methods were created to achieve rapid production without the need for such large equipment. One such iteration is the current state of 3D printing that uses fused deposition of thermopolymers to fabricate the desired object. These thermopolymers have no melt point; instead, they achieve melt-flow in the presence of heat, but rapidly return to room temperature once removed from the heat. As such, current versions of 3D printers utilize filaments of these thermopolymers to lay successive thin layers(~200μm thick) atop one another until the construct is achieved. Desired constructs are modeled in a computer

aided design (CAD) program, then interpreted by the 3D printers software. In recent years, these machines have become widely available for consumer consumption, and are capable of to fabricate nearly any desired object rapidly, cheaply, and with an amazing degree of accuracy with only input of the modeled file from the manufacturer. Current research and market efforts are to fabricate filaments with unique desired characteristics per filament to enable a wide range of manufacturing options to be available to consumers and researchers alike.

As pertains to nuclear shielding, many considerations must be made dependent upon the nuclear material being shielding. Nuclear materials emit several different species of radiation, each having a unique interaction with matter with which it comes in contact. Each of these species present must be kept in mind as a containment system is being considered to ensure that the shielding material is well suited to the job it must perform. For this reason, discussion of radiological sources and specific interactions with matter of alpha, beta, gamma, and neutron radiation is presented prior to presentation of current research efforts.

In the present work, the ability to introduce powdered metal additives into commercial fabrication methods is achieved. Further, these filaments were capable of printing up to 25wt% doping, and showed significant shielding properties of the nuclear material they were tailored to shield.

4.2 Radiation Sources

The four major types of radiological sources that will be dealt with in this body of work are alpha, beta, gamma (electromagnetic radiation), and neutron. The alpha and beta emissions are classified as charged particle radiation, while the gamma and neutron

radiation is classified as uncharged particle radiation. These types or radiation can be either ionizing or non-ionizing, both of which are of interest in relation to this work.

Each radioactive isotope contains different signatures in its emitted radiation. These signatures vary by isotope in half life, type of radiation emitted, and the associated energy of these emissions. The "radioactivity" of an isotope describes the decay rate of the particular isotope. This property can be expressed mathematically as

$$\frac{dN}{dt} = -\lambda N, \tag{4.1}$$

where dN/dt is the change in number of radioactive nuclei, N is the number of radioactive nuclei you begin with, and λ is the decay constant. Units associated with this are typically referred to as Curies (Ci), where one curie is 3.7×10^{10} disintegrations per second.

The half life of materials also varies depending on the isotope. The half life is defined as the time it takes for half of the original radioactive nuclei to decay. Because the radioactivity of a material remains relatively constant over time, the decay of nuclei in the source is an exponentially decreasing function. The decay mechanic of a material governs what species of emitted radiation will be produced. Depending on the source, multiple species and/or energies of radiation can be emitted as the material follows its decay path to lowest potential energy. The energy spectra of the released radiation is highly dependent and characteristic of the parent nucleus. When discussing the energy of emitted radiation, the conventional unit used is electron-volts (eV).

4.2.1 Alpha Particle Sources

Alpha particles are defined as nuclei of helium atoms (^{4}He nuclei), and are typically produced by heavy nuclei. These heavy nuclei are energetically unstable, and

thus emit an alpha particle in an attempt to reach a more stable internal equilibrium. Thus, by the emission of two protons and two neutrons, the daughter nuclei is at a more favorable energy than the mother nuclei. The decay process can be described as

$$ {}^{A}_{Z}X \rightarrow {}^{A-4}_{Z-2}Y + {}^{4}_{2}\alpha \tag{4.2} $$

where X is the mother nuclei and Y is the daughter nuclei. After alpha decay, the daughter is a completely different element than before the decay due to the emission of protons.

To ensure conservation of momentum in the situation described in Eq. 4.2, the daughter nuclei and alpha particle released must have equal but opposite momentum. Due to the difference in size, the alpha particle is able to go much farther due to this release momentum than the daughter nucleus from the recoiling momentum. While alpha emitting sources can be considered mono-energetic, small changes in detected energy can result from different probabilities of varying energies for the recoil daughter nucleus, leading to a different emission energy for the alpha particle.

4.2.2 Beta Particle Sources

Beta decay, the process of emitting a fast electron, begins in the nucleus of an atom, and, depending on the occurrence in the nucleus, can occur one of two ways. In beta minus decay, the most common method, a neutron in the nucleus is converted to a proton. This occurs due to the nuclei attempting to reach the optimal ratio of protons to neutrons within the nucleus, and can be described as:

$$ {}^{A}_{Z}X \rightarrow {}_{Z+1}{}^{A}Y + \beta^{-} + \bar{\nu} \tag{4.3} $$

where X is the mother nuclei and Y is the daughter nuclei. The antineutrino $\bar{\nu}$ is added to the equation for conservation of mass, energy, and charge in the decay process. Conversely, beta plus decay is the release of a positron and neutrino when a proton in the

nucleus is turned into a neutron. Because the mass of a neutron is greater than a proton, beta plus decay absorbs energy instead of releasing energy as in beta minus decay due to the decay in mass, and can be described as:

$$ {}^{A}_{Z}X \rightarrow {}_{Z-1}{}^{A}Y + \beta^{+} + \nu \tag{4.4} $$

where again X is the mother nuclei and Y is the daughter nuclei, and again the neutrino ν is added for conservation purposes. Both the neutrino and antineutrino produced can effectively be said to have no mass, and in both decay modes the daughter nucleus Y will negligible recoil momentum.

Each beta decay has a characteristic energy associated with it known as the Q-value. Thus, the resulting electron or positron produced from the decay will have an energy somewhere between zero and this Q-value, which is the fixed decay energy of the process. This Q-value assumes that both the mother and daughter nuclei are at ground state; should either the mother or daughter nuclei be at an excited state when the decay occurs, gamma rays will also be produced upon the beta decay, and may alter the Q-value for the overall process. As an example of the beta decay process, shown in Figure 4-1 is the beta emission spectrum of ^{36}Cl.

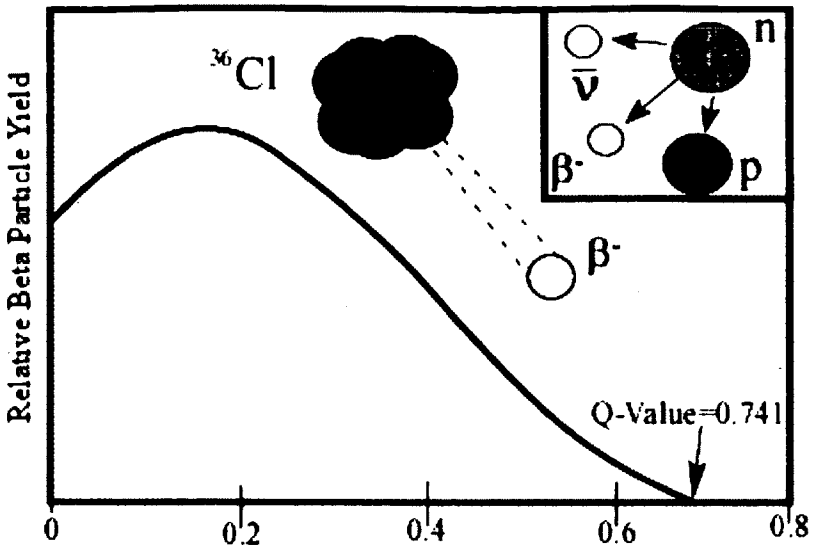

Figure 4- 1: Beta emission spectrum of ^{36}Cl.

Sometimes this broad energy spectrum is undesirable, as in the energy calibration of an electron detector. In this case, a source that undergoes internal conversion is preferred due to the near monoenergetic characteristic electrons produced. The internal conversion process begins with an excited nuclear state, which can occur from previous decays. Because of the resulting excitation of the daughter nucleus, the nucleus must lose energy, and as such if gamma emission (the common decay mode in such a situation) is inhibited, the resulting excitation energy can be directly transferred to one of the orbital electrons, resulting in its emission. This resulting emission will have a characteristic energy of the excitation energy less the binding energy of the electron, producing the characteristic near monoenergetic electron desired.

4.2.3 Electromagnetic Radiation

When dealing with nuclear reactions, two main types of electromagnetic radiation are of interest: gamma rays and X-rays. Gamma rays are produced as a direct result of a

nuclear reaction, while X-rays are produced by the decay of an electron from an excited state. Both of these types of electromagnetic radiation can be considered photons with different energies, and thus different wavelengths. This energy can be described by:

$$E_p = h\nu = \frac{hc}{\lambda} \tag{4.5}$$

where E_p is the energy of the photon, h is Planck's constant ($4.135 \text{ X } 10^{-15}$ (eV•s)), ν is the frequency of the photon, c is the speed of light, and λ is the wavelength of the photon. Because the gamma rays produced are of pure energy, this is a preferred method of decay of excited nuclei either before or after other modes of decay. The energy of the gamma ray produced will essentially be the energy required to decay from the excited state to the ground state, leading to very characteristic emissions. While beta sources may have a half life of hundreds of days, a resulting daughter nuclei that is left in an excited state will decay to ground state within picoseconds through the gamma process. Because of the characteristic monoenergetic gamma rays produced through this decay mode, any variation in detection arises solely due to the resolution of the detector illustrated in Figure 4-2.

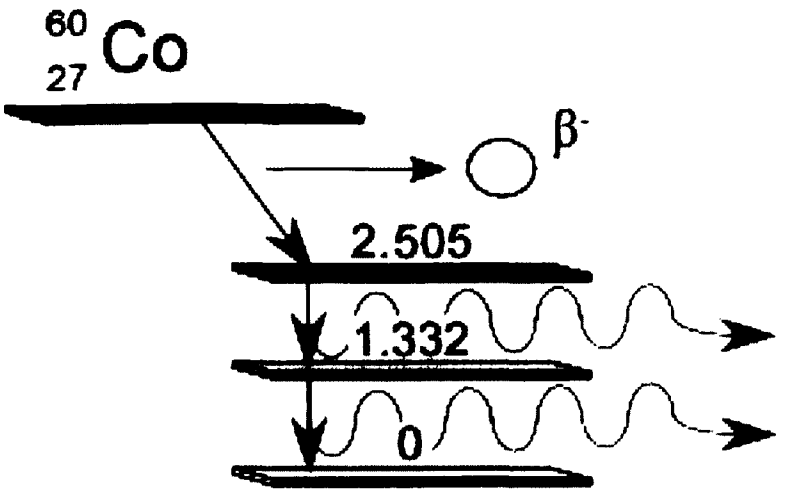

Figure 4- 2: Decay scheme of ^{60}Co.

Another source of gamma radiation is annihilation radiation. When β^+ decay occurs, the generated positron typically only travels a few millimeters. Because of this, the positron's path may be stymied from the inherent encapsulation around the source. Should the positron's energy be sufficiently low at the end of its path, the positron will recombine with a present electron in the absorbing material, resulting in the annihilation of both. The result of this is the generation of two oppositely directed 0.511 MeV photons known as annihilation radiation. This radiation then adds to any present gamma radiation from normal decay, superimposing a peak of 0.511 MeV onto any gamma radiation already produced by the daughter product of subsequent beta decay.

Gamma rays can also be produced following a characteristic nuclear reaction, resulting in much higher energy gamma rays produced than those following a beta decay. When an alpha particle interacts with a target material such as ^{9}Be or ^{13}C, a new element (^{12}C and ^{16}O, respectively) can be produced along with a neutron. The resulting daughter nucleus of such a reaction will be left in an excited state, and thus release gamma

radiation to fall to ground state. Gamma rays may also be produced from the absorption of thermal neutrons by a nucleus, and can have energies as high as 9 MeV [112].

When the orbital electrons of an atom are disrupted from their normal configuration, the atom may exist in an exited state. To compensate for this, the electrons rearrange themselves to bring the atom back to its ground state. When an excited electron falls from an excited state to a lower energy state, a characteristic X-ray photon is produced with an energy equal to the difference of the excited and final state of the electron. The highest energy X-ray photons are obtained when an electron transitions from an upper shell to the K-shell, the closest shell to the nucleus. Multiple decay modes resulting in X-rays are shown in Figure 4-3.

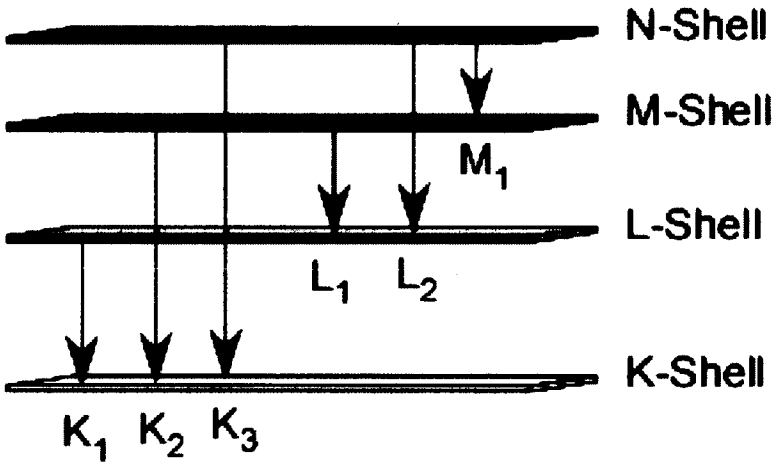

Figure 4- 3: Electron orbital decay transitions.

The greater the atomic number of an element, the more electron shells the element will have, and thus stronger X-rays can be obtained by the excitation and decay of electrons in heavier elements. This excitation can occur in several ways. One method for

this excitation is from external radiation. When an external radiation source is used to excite a target material, characteristic X-rays can be produced. Depending on the weight of the nuclei of the target material, a softer or harder X-ray can be obtained by offering the electrons a greater number of shells through which to decay. As described above, a higher Z element can result in a higher energy X-ray photon. Another method for excitation is by radioactive decay via electron capture. When a K-shell electron falls to the nucleus and combines with a proton, a neutron is formed. While the valence band of the atom now has the requisite number of electrons, there is a vacancy in the innermost K-shell that must be filled for the atom to reach equilibrium. As such, once an electron falls to fill this gap, an x-ray is produced characteristic to the decay of the electron filling the hold. Internal conversion may also result in X-rays being produced. When an orbital electron is emitted from the internal conversion process, a vacancy is left behind. Because the K-shell electrons are most readily converted, it is the K-series X-rays that are most prominent.

4.2.4 Neutron Radiation

While choices abound for beta and gamma sources, neutron sources are much different in that they do not conveniently exist as byproducts of other radioactive decay processes. A nuclei with excitation beyond the binding energy of the neutron in the nucleus must be created. As such, the possible choices to create this excitation are limited to either spontaneous fission or by inducing a stimulated nuclei as the by product with some incident particle from a more conventional decay process.

Spontaneous fission is the splitting of a heavier nucleus into two smaller nuclei, and can result in several byproducts such as alpha and beta particles, gamma rays, and

one or more neutrons. Spontaneous fission occurs primarily in the heavy nuclei of transuranic nuclei, with ^{252}Cf being the most common with a half-life of 2.65 years. Neutron sources must be enclosed in an absorption medium to block the byproduct charged particles, only allowing the gamma and neutron radiation to escape. Because these byproducts are a part of the spontaneous event, the emitted neutrons from a source such as ^{252}Cf result in a large energy spectra with a specific Q-value (endpoint energy) for the material.

Neutrons can also be produced through several different nuclear reactions using a radiation source to excite the nucleus of the target material. In one case, alpha particles can be used to bombard a target material of ^{9}Be to induce a high neutron yield. Equation 4.6 shows this reaction, which has a Q-value of +5.71MeV.

$$^{4}_{2}\alpha + {}^{9}_{4}Be \rightarrow {}^{12}_{6}C + {}^{1}_{0}n \tag{4.6}$$

For this reaction, the neutron yield is determined by the thickness of the beryllium and the energy of the bombarding alpha particles. In determining the optimal thickness of beryllium with consideration of the alpha particle energy, the beryllium must not be thick relative to the penetration of the alpha particle, or the target material will simply block the alpha particles instead of reacting. When this is the case, there is only a 0.01% chance of producing a neutron. Because of this low probability, a highly active alpha source must be used to increase the number of neutrons being emitted from the target. As such, these neutron sources are typically made as metallurgical alloys consisting of the alpha emitter (typically actinide elements) and beryllium to ensure no loss between the alpha emission and the interaction with the beryllium nucleus.

Another case of nuclei excitation by external radiation is the emission of neutrons through gamma stimulation of target nuclei. As in the previous case, a target material is

combined with a gamma emitter to generate the neutrons desired. Only two materials are practical in this application: ^{9}Be and ^{2}H. The reactions (Q = -1.666 MeV and -2.226 MeV, respectively) involving these two are given in Equations 4.7 and 4.8.

$$^{9}_{4}Be + h\nu \rightarrow {}^{8}_{4}Be + {}^{1}_{0}n \tag{4.7}$$

$$^{2}_{1}H + h\nu \rightarrow {}^{1}_{1}H + {}^{1}_{0}n \tag{4.8}$$

To induce the emission of the neutron desired, a gamma ray with an energy of at least the Q-values previously stated must interact with the target material. If the gamma rays used to created the desired neutron are monoenergetic, the neutrons emitted will also be nearly monoenergetic (variations occur due to angle of incidence of the gamma ray acting on the nucleus and kinetic degradation of neutron energy in escaping the emission medium). A disadvantage of these types of sources is the low chance of neutron emission per gamma ray excitation; only about one gamma ray in 10^{5}-10^{6} will react to generate a neutron.

A third type of nuclear reaction induced neutron emission is the use of accelerated charged particles. Using ionized deuterium accelerated to a potential of 100-300 keV, targets of deuterium or tritium can be used to produce neutrons by Equations 4.9 and 4.10.

$$^{2}_{1}H + {}^{2}_{1}H \rightarrow {}^{3}_{2}He + {}^{1}_{0}n \tag{4.9}$$

$$^{2}_{1}H + {}^{3}_{1}H \rightarrow {}^{4}_{2}He + {}^{1}_{0}n \tag{4.10}$$

These reactions have Q-values of 3.26 MeV and 17.6 MeV, respectively, and produce near monoenergetic neutrons per reaction: 3 MeV for the first, and 14 MeV for the second.

4.3 Radiological Interactions with Matter

In considering a shielding platform for these species of radiation, the type of radiation, the energy of the radiation, and the material of the detector or moderator must be considered. The absorption range of the medium depends on the thickness of the absorbing material and the elements the absorber consists of, which in turn dictates how much energy the particle will transfer to the medium. This is one major concern in miniaturizing these devices as absorption is purely a function of the material and the thickness of the media being used, leading to restrictions on size should a specific shielding material be desired. If the absorption range is too small, the impinging radiation only imparts a portion of the original energy if any at all.

4.3.1 Alpha Particle

Alpha particles interact with matter primarily through the Coulombic forces present due to the charge of the alpha particle (positive charge) and the electrons (negative charge) of the material it is passing through. Upon entering any medium, the alpha particle immediately reacts with numerous electrons simultaneously. Each electron feels an impulse from the attractive Coulomb force as the positively charged alpha particle passes through leading to two potential interactions depending on the proximity of the alpha particle to the electrons: excitation, wherein the electron is stimulated to a higher potential, or ionization, resulting in the removal of the electron from the atom. The energy imparted to these electrons results in a decrease in velocity of the alpha particle, and because of the simultaneous pull from the orbitals in all directions as the alpha particle passes, the alpha particle will have a linear path through the material. Due to these heavy interactions with present electrons in the medium the alpha particle is

travelling through, energy is lost quite readily. Common penetration depths for alpha particles are on the order of a few centimeters in air, and can be blocked completely by the outer layer of skin or a sheet of paper.

4.3.2 Beta Particle

Beta particles also lose their energy through Coulombic forces, however it is at a much lower rate than alpha particles, and in no way follows a linear path through absorbing materials. These large deviations in the electrons path are possible because of the equality of the fast electron and the orbital electrons with which the beta particle interacts, enabling a much larger portion of energy to be lost in a single encounter or electron-nuclear interactions to occur which abruptly change the electron's direction.

Beta particles that have a lower energy are quickly absorbed by materials that have small thicknesses, which leads to a much greater initial drop in the number of transmitted betas through an absorbing material, as depicted in Figure 4-4.

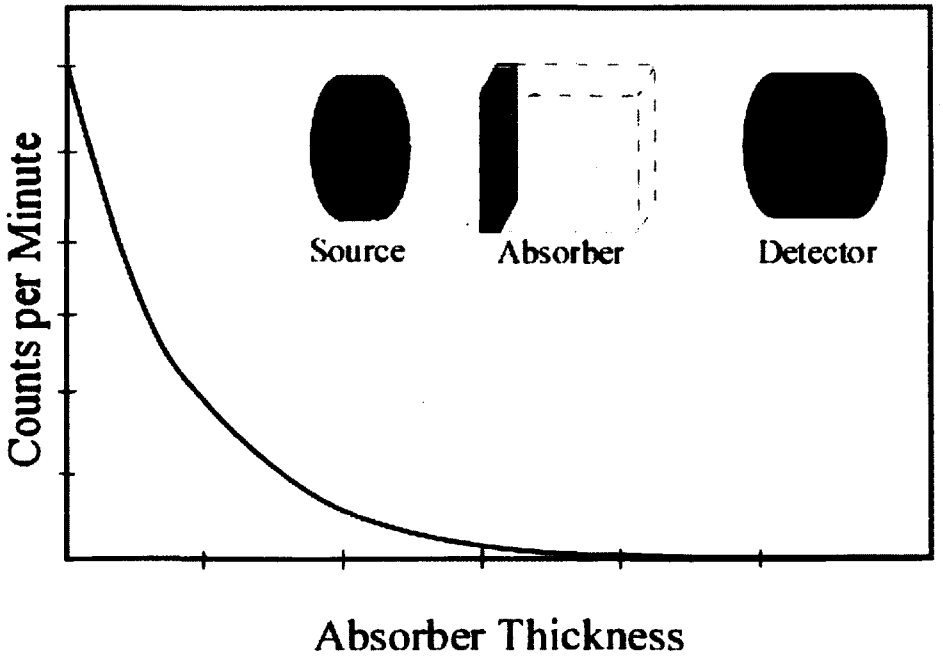

Figure 4- 4: Range of beta particles in a medium.

Because of the meandering path of the electrons through the material, an immediate drop in betas detected occurs in even very thin absorbing materials. As this thickness increases, more beta particles are scattered by the interactions with the orbital electrons, leading to an even greater drop in betas reaching the detection medium. For the majority of beta emissions, the emission curve of beta emission has a near-exponential shape. The range of most beta sources can be approximated as

$$\frac{I}{I_0} = e^{-nt} \tag{4.11}$$

where I is the counting rate of a detector with an absorbing material between the emitting source and detector, I_0 is the counting rate of a detector with no absorbing material, t is the thickness of the absorber, and n is the absorbing coefficient. The generated curve from 4.11 gives an exponential decay due to the rapid absorption of lower energy betas, leaving only higher energy betas to make it through the absorption material to the detector. The same case can be made for positrons emitted from β^+ emission as the mass of the positron and electron are about the same, leading to the same impulse and energy transfer through a medium. The only difference for positrons is the emission of annihilation radiation as described previously at the end of the positrons tract leading to a 0.511 MeV photon being released which is very penetrating compared to the penetration depth of the positron, and thus can lead to energy deposition far from the origin of the photon.

4.3.3 Gamma Radiation

Gamma rays and X-rays have numerous interactions with matter, but for the purposes of detection and moderation, only the three primary interactions will be discussed: photoelectric absorption, Compton scattering, and pair production. Each

process leads to the partial or complete transfer of energy from the incident photon to an electron in the absorbing medium. The result of this energy transfer is a disappearance of the photon or a scattering of a significant angle, changing the rays path completely. This differs from the previous two forms of radiation in that it is not a gradual decay of energy, but a sudden loss of energy without the alteration of speed.

In photoelectric absorption, the incident photon reacts with the absorber atom by completely imparting its energy to the absorber atom. This in turn releases a photoelectron, typically from the K-shell of the atom, with an energy characterized by

$$E_{e^-} = h\nu - E_b \tag{4.12}$$

where E_{e^-} is the energy of the electron, E_b is the binding energy of the photoelectron, and $h\nu$ is the energy of the gamma ray. Because an electron is emitted through this process, a vacancy in the absorbing atom remain, and is quickly filled through either electron capture or the rearranging of the electron configuration in the atom. The filling of this vacancy can produce one or more characteristic X-ray photons.

Compton scattering occurs between the incident gamma photon and electron in the absorbing medium, and is the typical process through which gamma photons interact with a medium. The incident gamma photon collides with an orbital electron of the absorbing atom and can transfer any portion of its energy from a small amount to all of it to the electron. The collision results in a path change as shown in Figure 4-5.

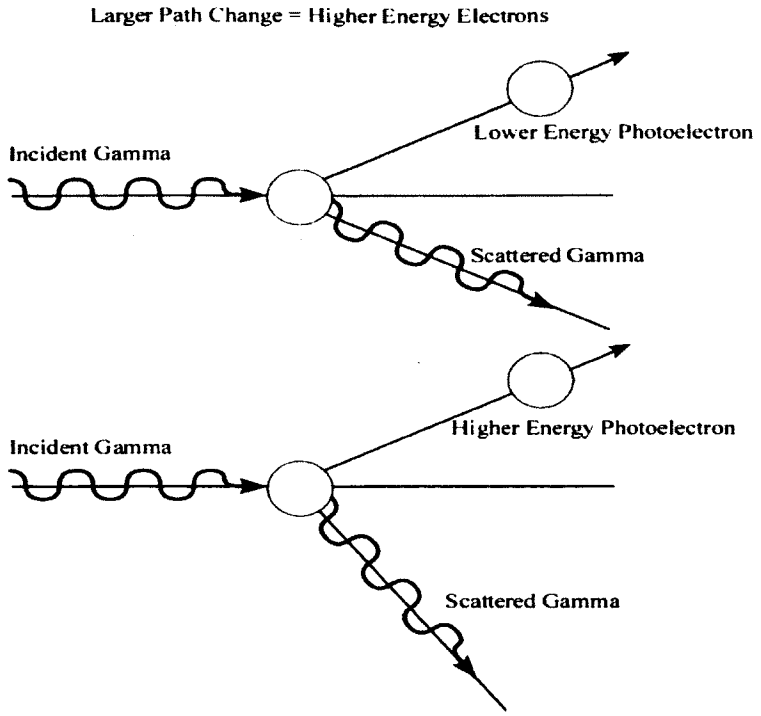

Figure 4- 5: Compton scattering.

The angle of deflection of the resulting gamma photon is the basis for the energy imparted to the emitted photoelectron. Through Compton scattering, any angle of deflection of the incident gamma ray is possible. In the extreme case where the gamma is completely reflected, the gamma ray retains a small portion of its initial energy.

A scattered gamma photon then goes on to either interact again with another electron in the medium or to completely escape without depositing the remaining energy.

Pair production is an interaction that is only possible when the incident photon has an energy exceeding twice the rest-mass energy of an electron (1.02 MeV). As the energy of the gamma photon increases, this type of interaction becomes more likely, especially in the many-MeV range. In pair production, the gamma ray photon disappears completely upon interacting with the coulomb field of a nucleus and results in the

production of an electron and positron. Because the pair production requires 1.02 MeV to generate the electron-positron pair, any energy above this threshold goes solely into kinetic energy shared by the pair. The positron will then undergo annihilation once sufficient energy has been lost through kinetic reactions by recombining with an electron, and produces two annihilation gamma rays. The electron can be subsequently detected, however it will vary in energy depending upon the energy of the incident gamma ray and how much the electron has slowed down before being detected.

Gamma ray attenuation in a medium can be expressed exponentially by

$$\frac{I}{I_0} = e^{-\mu t} \tag{4.13}$$

where I_0 is the original number of gamma rays emitted from a source, I is the number of detected gamma photons, t is the thickness of the absorption medium, and μ is the linear attenuation coefficient. A mean free path for gamma ray photons can then be obtained by

$$\lambda = \frac{\int_0^\infty x e^{-\mu x} dx}{\int_0^\infty e^{-\mu x} dx} = \frac{1}{\mu} \tag{4.14}$$

and is simply the reciprocal of the linear attenuation coefficient. Typical values for the mean free path are on the order of a few millimeters to tens of centimeters depending on the solid material. Because the linear attenuation coefficient varies by the density of the absorption medium, a more useful and more widely used mass attenuation coefficient can be expressed as

$$mass\ attenuation\ coefficient\ = \frac{\mu}{\rho} \tag{4.15}$$

where ρ is the density of the medium. Use of the mass attenuation coefficient then changes the attenuation equation to

$$\frac{I}{I_0} = e^{-\frac{\square}{\rho}\rho t} \tag{4.16}$$

where the addition of the density coefficient must be added to maintain the equation.

4.3.4 Neutron Particle

Neutron radiation is similar to gamma radiation in that it is uncharged, and thus cannot react via coulomb forces to reduce energy. Unlike gamma radiation, neutrons can travel through many centimeters of matter before any interaction occurs, leading to difficulties in shielding. Upon interaction, the neutron reacts with the absorbing nucleus, and can either totally disappear due to absorption or result in secondary radiation, or can simply lose energy and change path. Neutrons are classified by denoting them as either fast or slow for the purposes of interaction. Slow neutron classification is any energy below 0.5 eV. This denotation arises from the cadmium cutoff where the neutron absorption cross section for cadmium changes significantly.

For slow neutrons, the significant interactions include elastic scattering with absorber nuclei and a large set of neutron-induced secondary reactions. Because the energies of slow neutrons are so small, very little energy can be imparted via scattering. Thermal neutrons have an average energy of about 0.025 eV. Of greater importance in shielding neutrons are the neutron-induced secondary reactions that can take the form of gamma emission (n,γ), beta emission (n,β), alpha emission (n,α), and positron emission (n,p).

The shielding of fast neutrons relies more primarily on the scattering reaction due to the greater energy able to be imparted from the incident neutron to a nucleus. For elastic scattering, the neutron loses energy for every reaction of moderating material, slowing the neutron down. The most efficient nuclei for moderating neutrons is

hydrogen due to similar size of the nucleus (one proton) to the size of the neutron. Inelastic scattering is also a possibility for fast neutrons if the energy of the neutron is sufficiently high enough, wherein the recoil nucleus is elevated to an excited state and decays through the emission of one or more gamma rays. Inelastic scattering results in a greater fraction of neutron energy being lost than in elastic scattering.

Transmission of neutrons through a material is similar to gamma rays, however it is preferable to discuss the absorbing nuclei in terms of their neutron cross section. This neutron cross section is the probability a neutron will react with a given nucleus at a fixed neutron energy. Neutron cross section is measured in barns (10^{-28} m^2), and will include the primary mechanism for neutron interaction (elastic/inelastic scattering, radiative capture, etc.). In terms of moderating neutrons, it is favorable to discuss the macroscopic cross section of a material rather than the cross section of each individual atom, which is given by

$$\Sigma = N\sigma \tag{4.17}$$

where N is the number of nuclei per unit volume, and σ is the cross section of those nuclei. For practical use, this equation can be expanded to

$$\Sigma_{tot} = \frac{\rho N_A}{A}\sigma_{tot} \tag{4.18}$$

where ρ is the density of the material, N_A is Avogadro's number, and A is the atomic mass of the element. For a compound material, Σ_{tot} is the summation of the macroscopic cross section of each element within the compound. Neutron attenuation will fall off exponentially, as given by

$$\frac{I}{I_0} = e^{-\Sigma_{tot} t}, \tag{4.19}$$

and the mean free path can be calculated the same as for gamma rays, resulting in

$$\lambda = \frac{1}{\Sigma_{tot}}. \tag{4.20}$$

For slow neutrons, the mean free path may be on the order of a centimeter or less. For fast neutrons, the thickness could be as much as tens of centimeters depending on the energy of the neutron and the moderator used.

As stated, the lack of charge for neutrons present a difficulty of sensing this type of radiation. For the purposes of detection and shielding, downgrading of fast neutrons to thermal equilibrium can be advantageous as secondary reactions with target nuclei occur. For the purposes of this document, the ^{10}B, ^{6}Li, and ^{157}Gd reactions will be discussed as they are pertinent to the absorption of neutrons.

The ^{10}B(n,α) reaction is the most popular reaction for the conversion of slow neutrons directly into detectable alpha particles. The reaction can take two paths given as

$$^{10}_{5}B + ^{1}_{0}n \rightarrow \begin{cases} ^{7}_{3}Li + ^{4}_{2}\alpha \\ ^{7}_{3}Li^{*} + ^{4}_{2}\alpha \end{cases} \tag{4.21}$$

where the first is the generation of the lithium daughter nuclei in its ground state (2.792 MeV), and the second is the generation of the lithium daughter nuclei in its excited state (2.310 MeV). For this reaction, thermal neutrons cause 94% excited lithium to be produced with only 6% of ground lithium being produced. Because the neutron used to incite this reaction has such a low energy, the generated Q-values for both the ground and excited state lithium and the accompanying α particle are primarily resultant from the reaction itself, causing any information about the incident neutron to be lost. The daughter lithium atom and recoiling alpha particle must always be emitted in exactly opposite directions for conservation of momentum. The thermal neutron cross section for

^{10}B is 3840 barns. It drops rapidly with increasing neutron energy, and is proportional to the reciprocal of the neutron velocity. A resonance occurs when the neutron energy approaches about 500keV, leading to large fluxuations in cross sectional area.

The ^{6}Li(n,α) is another popular reaction for the detection of slow neutrons. This reaction proceeds only to the ground state of the daughter atom, and is given as

$$^{6}_{3}Li + ^{1}_{0}n \rightarrow ^{3}_{1}H + ^{4}_{2}\alpha \qquad (4.22)$$

with an overall Q-value of 4.78 MeV. The tritium atom and alpha particle have energies of 2.73 MeV and 2.05 MeV, respectively. The thermal neutron cross section for this reaction is 940 barns, about one-third that of the ^{10}B, and has a large resonance peak above neutron energies of 100 keV.

Lastly, the ^{157}Gd reaction results in emission of both gamma rays and conversion electrons. ^{157}Gd has a thermal neutron cross section of 255,000 barns, one of the highest cross sectional areas of known atoms. The most significant secondary emission of neutron capture by ^{157}Gd is a 72 keV conversion electron that is emitted 39% of the time. The range of this electron in a typical Gd-containing material is about 20μm. The conversion efficiency of such a layer of Gd can be as high as 30%, much higher than the <5% efficiency found in either ^{10}B or ^{6}Li layers.

In terms of shielding applicability of these materials to blocking of neutrons, the complete absorption of the thermalized neutrons is desired such that the secondary reaction products can be successfully shielded. Typical moderating material includes plastics such as polyethylene which has a high hydrogen content. This allows for elastic scattering, which is more probably than inelastic scattering, and allows for the incident neutron to impart as much as half of its energy into the target hydrogen nucleus. For this reason, the use of one of the aforementioned materials incorporated into a primarily

plastic shielding can allow for the necessary moderation of fast neutrons and the consumption of thermal neutrons with predictable secondary decay products that can be further shielded by successive layers.

4.4 Design and Objectives

This research examines the ability to fabricate metallic doped 3D printing filaments using commercially available equipment, printability of these fabricated filaments, and the shielding capabilities of the fabricated objects. The following sections give a more in depth breakdown of the objectives to be achieved.

4.4.1 Filament Extrusion Objective

A method of introducing metallic additives into thermopolymer filaments via commercial fabrication will be developed. Further, the ability to fabricate 3D printing filament that is the proper diameter and of use in commercial fused deposition 3D printers will be developed.

4.4.2 3D Printing Objective

The ability to 3D print a custom extruded metallic doped filament will be demonstrated. This method will utilize commercially available 3D printing equipment, and take consideration such that no modification of the 3D printing equipment need be performed. Further, upper thresholds of printability of doped filaments will be examined to show limitations of the developed doping method.

4.4.3 Radiological Testing Objective

The functionality of the shielding properties of fabricated objects will be tested using appropriate radiological sources. Feasibly, neutron testing with be foregone due to lack of access to a proper neutron test facility.

4.5 Fabrication

To achieve the metal additive doped constructs for shielding, multiple steps had to be considered. First, because the constraint of no modification of commercially available equipment was decided upon, a method for dispersing additive into the filaments had to be developed. The filaments also had to be manufactured to the proper diameters and additives retained through the filament extrusion process without inhibiting the printability. Once the filaments were achieved, printing of simple constructs had to be accomplished using a commercial 3D printer with no modification.

4.5.1 Metal Coating of Pellets

One of the main challenges in introducing additives into the extruding process using a tabletop extruder is to ensure suspension of additives such that a gradient of dopant is not achieved. This results from the powder falling through the beads, leading to a dopant heavy filament being extruded first with a lighter doping of filament resulting on the back end. To achieve dispersion of additive into the PLA, several methods were attempted. The first method to achieve an even dispersion of dopant was to uniformly mix two powders, however this was not a readily viable option due to the lack of commercially available PLA powder. The method then evolved into using commercially available PLA pellets and manufacture a powder from them. In this pursuit, two methods were explored: grinding and freeze-fracturing. PLA is a very elastic polymer, and as such, all efforts in grinding the pellets resulted in minimal production of powder due to the pellets simply bouncing off the blades. Freeze-fracturing via liquid nitrogen also proved fruitless as PLA is a thermopolymer; once removed from the liquid nitrogen, the

PLA rapidly returned to room temperature such that any attempts to fracture the pellets were performed on pellets done at room temperature.

To enable dispersion of the desired additives through the use of commercially available PLA pellets, a coating method using KJL 705 silicone oil was developed. The silicone oil showed thermal stability for temperatures common to the extrusion of the PLA (170-180 °C) and allowed for surface suspension of particulate on the pellets. The coating material was arbitrarily chosen as it was readily available. Any material that enables this surface suspension of particulate will work, but may necessitate additional considerations. PLA was chosen as it is the most widely used polymer for commercial 3D printing.

The developed coating process was comprised of five basic steps, and for this discussion, a batch of 20 grams of PLA pellets will be will be used with the KJL 705 silicone oil. The beads must first be coated in silicone oil, however consideration on the amount of oil used must be taken into account as too much oil will lead to clumping and inhibition of meltflow of the plastic. For the sample of 20 grams of PLA pellets, 15μL of oil was used to fully coat the pellets via vortexing. After vortexing but prior to the introduction of additives, the beads must be placed in a new contained as coating of the initial container with oil has occurred. Without this transfer, significant loss of the additive will occur along the wall of the container. Once the oil coated beads are placed in a new container, the additive is introduced, and the mixture is again vortexed to allow for complete coating of the beads. Uptake of additives will vary through this method due to particle size. Visually, this process is shown in Figure 4-6, errors in the process are shown in Figure 4-7, and successfully coated pellets are shown in Figure 4-8.

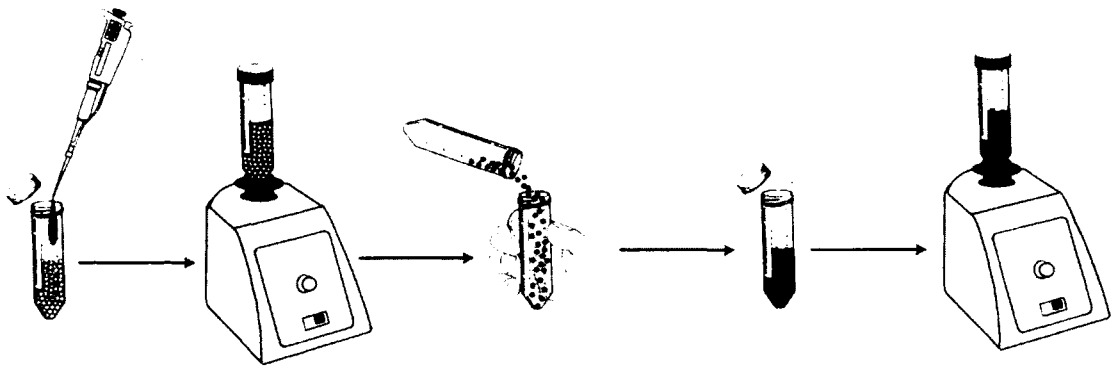

Figure 4- 6: Process of coating pellets with additives.

Figure 4- 7: Failure to change coating tube (left) and too much oil used (right).

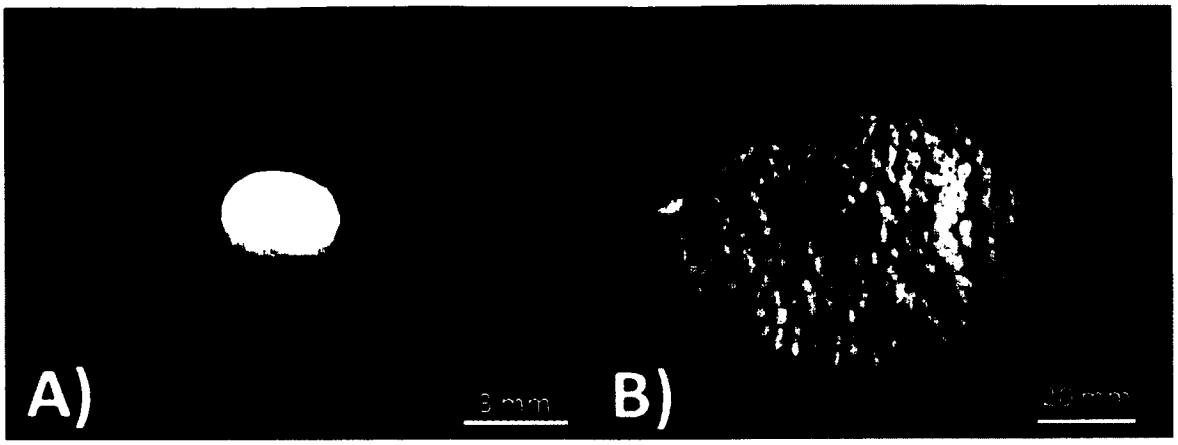

Figure 4- 8: Individual and batch coating of beads with barium sulfate.

Additives used with this method must be of sufficiently fine particle size; nanoparticles or nanostructures such as halloysite nanotubes are readily applicable for this method, however preprocessing of larger grain materials may be necessary to achieve successful fabrication with this method. One method of this preprocessing is ball milling which necessitates the use of higher density balls than the material being milled and can result in minor contamination. Sufficiently high doping of filaments (~5wt%) should overcome any contamination concerns. Other methods such as chemical processing may also be used provided a dry particulate is the end result.

This method was used to create metallic coatings of 5wt%, 10wt%, 15wt%, 20wt%, and 25wt% on PLA pellets. The pellets were coated in 10-15 μL in 20 gram batches using 50 mL sterile and disposable plastic test tubes. Using these weights, this meant that each successive 5wt% was equivalent to 1 gram of additive.

4.5.2 Layer-By-Layer Coatings

The coating procedure described above in Section 4.5.1 works well for the first ~5wt% coating without loss of additive. To overcome this barrier, this process was repeated in successive runs, allowing for uptake between 3.5-5wt% for each successive coating. This successfully allowed for coatings up to 25wt% for each of the metallic additives, but beyond this threshold, too much oil was involved to the point that the meltflow of the PLA was inhibited.

4.5.3 Filament Extrusion

An ExtrusionBot filament extruder was used to extrude the coated PLA pellets into filaments. The metal die used was 1.75 mm in diameter as this is the common filament size used in most commercial 3D printers. The proper extrusion temperature for uncoated PLA pellets is roughly 170 °C for the filament to maintain a 1.75 ± 0.1 mm diameter at a rate of a few feet per minute. Temperatures other than 170 °C can be used for extrusion, however these will affect the extrusion rate and the obtained diameter of the filament. A common problem in filament extrusion using this type of extruder is stretching or thinning of small sections of filaments during small batch manufacturing. These problems arise due to the small amount of backpressure on the auger system, leading to a lower backpressure at the extrusion die. Weight of extruded portions can also lead to stretching, but can be controlled through a constant pressure on the extruded filament as it exits the die. Further, a metal ramp for the filament to follow after it has left the die can lead to increase cooling, and reduce the load of already extruded filament on plastic leaving the extrusion die. Such a setup is shown in Figure 4-9.

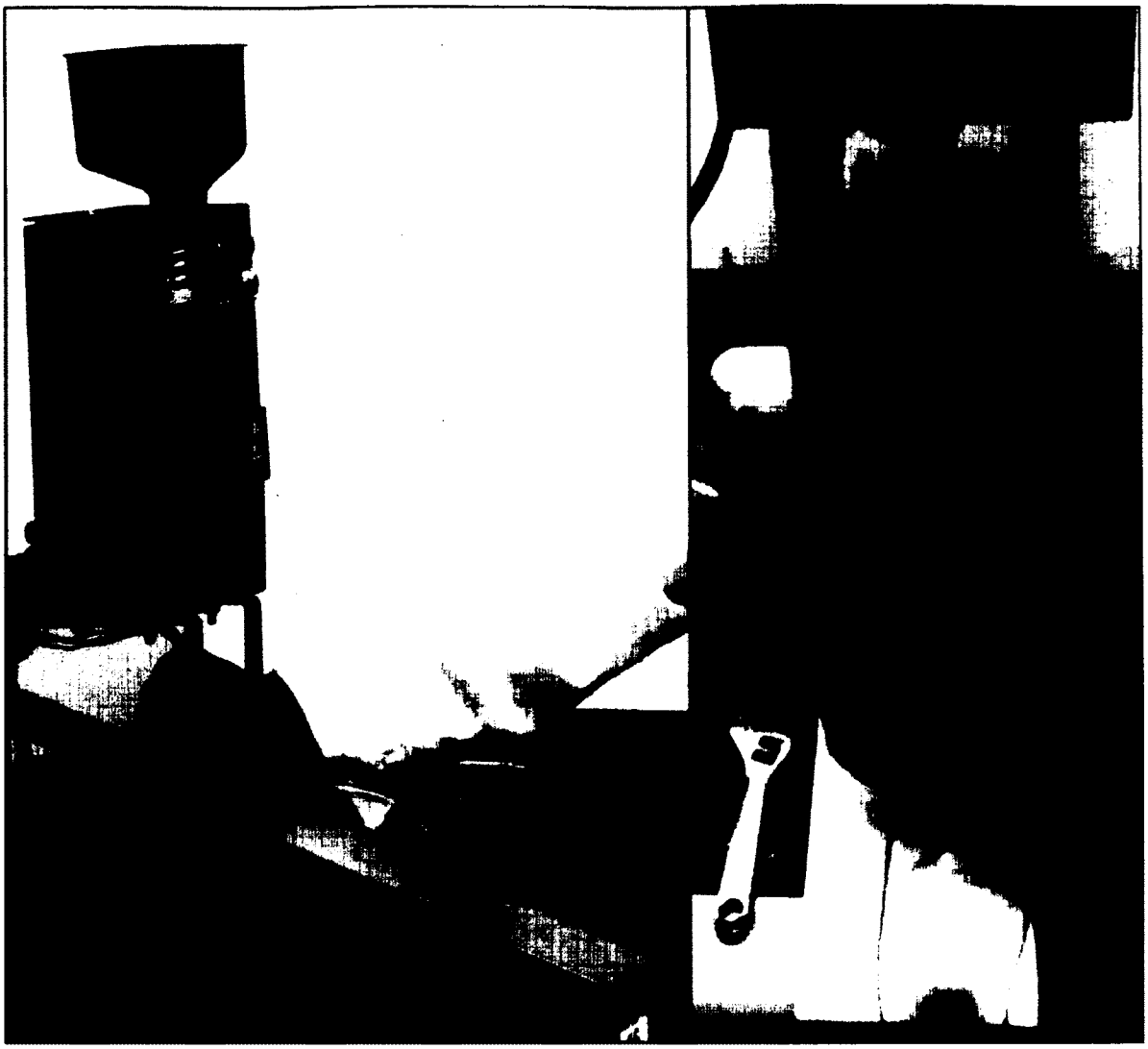

Figure 4- 9: Small batch filament extrusion with metal ramp.

Excess temperatures during extrusion may cause a condition referred to as "thermal runaway" wherein meltflow rates are increased, leading to issues with filament diameter. Further, introduction of additives or excess of coating oil can also cause this issue, and may dictate real-time adjustments during extrusion to maintain desired filament diameter. Excess oil in particular can lead to filament bubbling, leading to irregular surfaces, or oil sheaths, leading to inhibited printability. Batches of raw PLA

should be extruded to ensure temperatures of the machine are accurate as heating sensor discrepancy can lead to compromised filaments.

To maintain the filament extruder, purging of the system must be done to flush any lost additive and remaining coated pellets out of the system. This purging must be done with the die both on and off; with the die removed, a large amount of material is able to pass rapidly out of the machine. With the die on, there is greater back pressure, allowing for cleaning of any remnants left in the die.

4.5.4 Construct Design and Printing

Constructs for printing were design in Solidworks and saved as .STL files. They were opened in the Makerware software program that is used with MakerBot 3D printers, then fabricated on a MakerBot Replicator 2X. Shown in Figure 4-10 is the .STL file for the squares fabricated for radiation shielding.

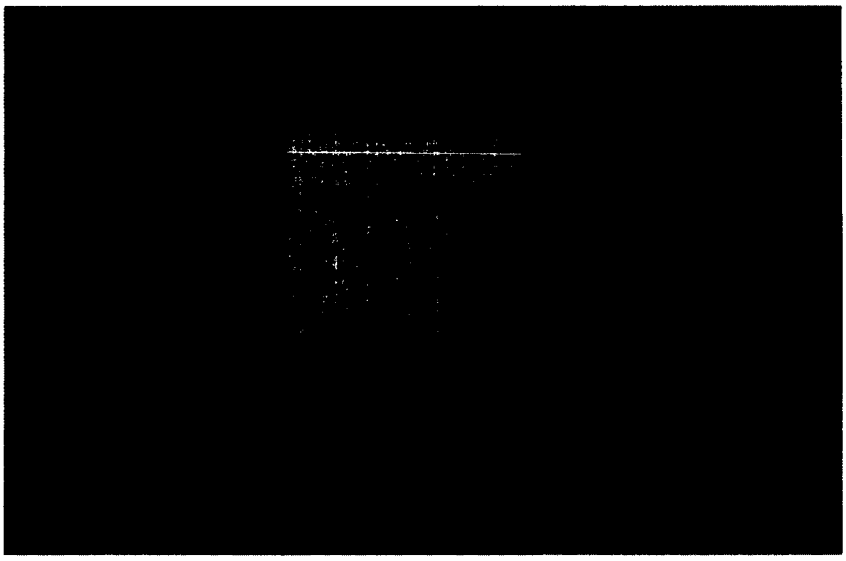

Figure 4- 10: .STL file of radiation shielding squares.

The squares were 1"X1" in size, and 1 mm thick to allow for stacking of the shielding. Printing was done at 220 °C, the common temperature for printing undoped PLA, and the construct was set to print at 100% fill.

4.6 Testing

This project required the use of a wide range of equipment and experimental protocols. It was critical to fabricate test control constructs prior to experimental constructs to prevent contamination. Manufacturing of filaments was performed in a fume hood, and experiments were run in as sterile conditions as possible. The equipment and experimental setup basic calibration testing and controls are described below.

4.6.1 Pellet Coating and Extrusion Process

To ensure proper retention of additives onto the surface of the pellets prior to extrusion, pellets were visually inspected to confirm even coating and lack of powder remaining in mixing tubes. Methods for pellet coating were checked by weight to ensure proper doping of additive was achieved..

Extruded filaments were visually checked for uniformity and consistent coloring based upon the additive. A digital caliper was used to confirm proper diameters were achieved (1.75 ± 0.05 mm). The initial and final portions of the filament (about two inches) were discarded to avoid improper doping between batches.

Three ExtrusionBot filament extruders were used during this project. Raw PLA pellets were forced through all machines initially to overcome any contamination within the machine that may have occurred during the fabrication process. Metal additives were run on the same machine from 5wt% to 25wt% in steps of 5wt% to ensure over doping did not occur for the smaller batches. Between fabrication batches, the extruder was

purged with raw PLA pellets until clear PLA filament was achieved, indicting full purging of any leftover additives. The hopper and tubing that served as the feed to the system were vacuumed to pick up any loose particles. For these purges, much higher temperatures were used (~220 °C) to ensure a more viscous meltflow was achieved as this served to pick up greater amounts of leftover additive in the machine.

4.6.2 Printer Testing and Controls

Prior to printing constructs, the 3D printer was calibrated and returned to factory setting to ensure minimal manufacturing error was introduced into the system. The MakerBot Replicator 2X used was purchased from the manufacturer and used for printing purposes of this project. All control constructs were manufactured prior to any doped constructs to avoid contamination within the print head. Constructs of sequentially higher doping were printed at a time, with purging of raw PLA done between each print. Print heads were changed between each dopant batch to ensure no cross contamination occurred. Before printing of doped filaments, the printer was used to manufacture multiple small constructs and these weights were compared to see inherent manufacturing error within the process. These constructs showed weight differences between 1%-5% for a sample batch of ten objects.

4.6.3 Radiation Testing of Squares

Radiation testing of the fabricated squares was done using tailored species of radiation. For the iron doped squares, a 0.5 MeV ^{90}Sr was used with a Geiger counter for measurements. The source was placed 10 mm away from the detection head and squares placed in the space in between. Background was negligible due to the detector being set on 10X. Statistics were performed on the source to test the spread of CPM obtained.

Statistical analysis was also performed on the squares of 5wt%, 15wt% and 25wt% for thicknesses of 1 mm (one square) and 3 mm (three squares randomly selected).

The barium doped squares were tested on the X-ray imaging machine at LSU Health. Lines of varying doping percent were lined up successively next to each other. Testing was also done on 2 and 3 mm of 25wt% while the rest of the doping percentages remained at 1mm thick to see the difference in opacity increased thickness would make.

4.7 Results and Discussion

Methods to create and manufacture 3D printable metal doped filaments in small batches were developed in phases to prove the concept was viable and to test the limitations of the method. First, the results of coating PLA pellets with three different dopants (iron oxide, barium sulfate, and gadolinium oxide) will be presented and discussed. Next, the extrusion and testing of these coated pellets will be discussed, and observations of the manufacturing will be presented. Finally, the manufacture of 1"X1"X1 mm squares will be shown, and their performance in shielding specific radiations will be presented.

4.7.1 Pellets

The basic manufacturing process described in detail in Section 4.5.1 was used for each material for doping percentages of 5wt%-25wt%. The coating materials were ground with a mortar and pestle as much as possible to reduce clumping due to humidity. Using proper amounts of coating material is critical to prevent clumping during the coating process or manufacturing problems during the extrusion process. The optimal oil per layer of coating ranged from 10-20 μL of oil for 20 g batches of pellets. Initial attempts that used higher amounts between 100-500 μL of oil resulted in significant

clumping of the pellets, coating of subsequent test tubes, and uneven retention of additives on the surface of the pellets. The low amount of oil only enabled about 3-5wt% retention of additive per layer, and use of a layer-by-layer technique enabled coating up to 15wt% for iron oxide and 25wt% for barium sulfate and gadolinium oxide.

To achieve greater iron oxide dopant concentration in the filament (20-25wt%), the manufacturing process had to be modified. First, a batch of 15wt% filament was extruded, then cut up into small pieces. These pieces were then subjected to the same oil/additive coating method, and enable manufacture of the desired 20-25wt% for iron oxide doping. This was necessary due to the small amount of iron capable of being coated above 15wt%, and the coating oil required to reach 20-25wt% drastically affected the extrusion process. Barium sulfate and gadolinium oxide were found to have higher retention rates on the pellets. This was attributed to both compounds being desiccant in nature, allowing additional coating onto the surface of the pellets due to natural humidity in the air.

Excess oil, as previously discussed, affected the coating of the pellets greatly, but also resulted in extruding problems. If the oil was not in great excess, but in significant amount during the extrusion process, warping of the filament could occur, or a shiny sheath along the filament exterior could be seen. This sheath proved to inhibit printing of the filament, and occasionally block the extrusion process. For greater amounts of oil, bubbling of plastic would occur during extrusion, leading to a liquid pouring out of the extrusion dye rather than a solid or semi-solid filament. This was attributed to a drastic buildup of oil in the melting zone of the extruder, subjecting the plastic to much higher

temperatures than expected. The proper coating process previously discussed was highly correlated to the success of later 3D printing.

Due to the constraint of no modification to commercial equipment, the coating process is critical to achieve the small batch extruded doped filaments. As previously discussed, the addition of powder and pellets directly to the extrusion system will not work, leading to a gradient of doping and no way to know the actual level of dopant within the filament. To achieve a consistent metal dispersion within the polymer, the oil coating method was used either singly of in a layer-by layer fashion for groups consisting of 5wt%-25wt% in steps of 5wt% for iron oxide, barium sulfate, and gadolinium oxide. Shown in Figure 4-11 is a single pellet and 20 gram batch coated in iron.

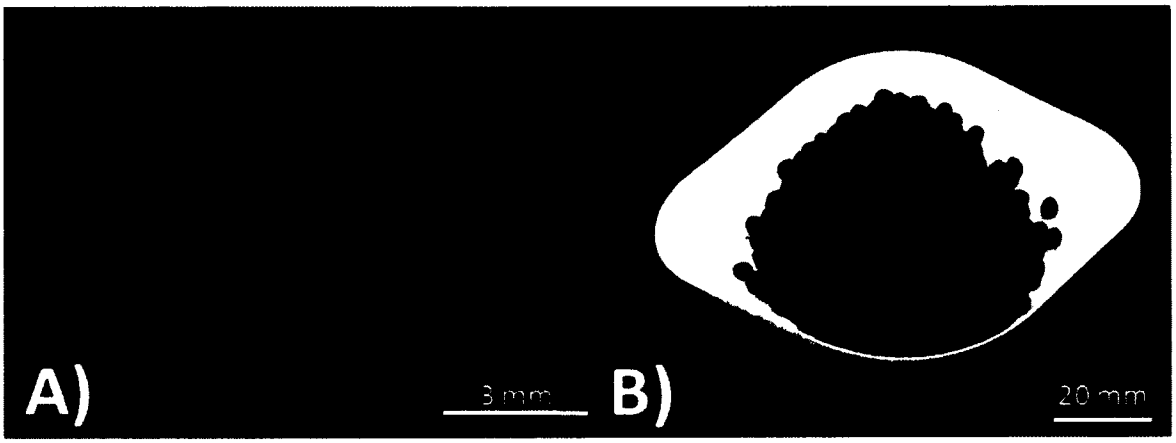

Figure 4-11: 10wt% iron oxide coated PLA (A) single pellet and (B) 20g batch.

The iron oxide proved to coat the pellets thoroughly. For subsequent coatings of the iron oxide, successively more oil was needed to achieve surface suspension. This is primarily due to the tendency of the iron to not clump, leaving the only mechanism for surface coating to be the oil. Figure 4-12 and 4-13 show single pellet and 20 gram batch coatings of barium sulfate and gadolinium oxide, respectively.

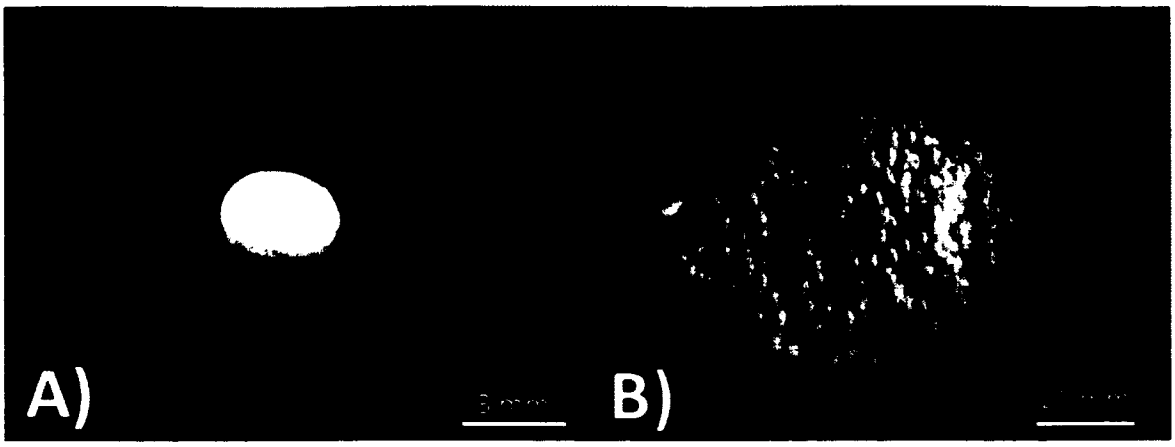

Figure 4-12: 20wt% barium sulfate coated PLA (A) single pellet and (B) 20g batch.

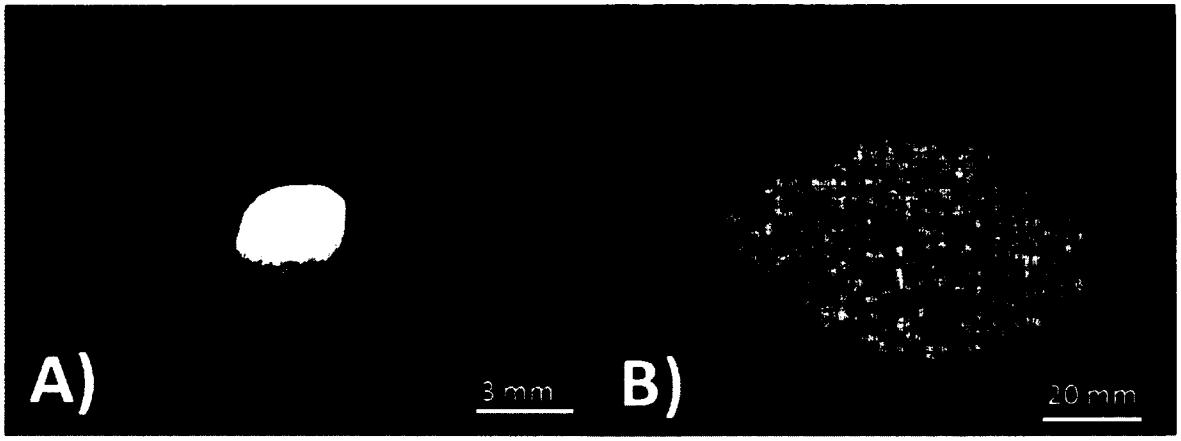

Figure 4-13: 10wt% gadolinium oxide coated PLA (A) single pellet and (B) 20g batch.

Due to the desiccant nature of .both barium sulfate and gadolinium oxide, inherent humidity in the ambient conditions led to greater coating of both these materials on the surface of the PLA with less oil needed than with iron oxide. This also aided in the extrusion of the filaments as less oil decreased the chances for problems during the extrusion, and did not necessitate coating and re-extrusion of cutup filaments.

4.7.2 Extruded Filaments

The controls and coated pellets were extruded into 1.75±0.05 mm diameter 3D printing filaments for fused deposition fabrication. An ExtrusionBot filament extruder was used, and only temperature modifications were made to suit different filaments as necessary. The majority of extrusion was done between 170° and 175 °C. For the 20 gram batches fabricated in the previous section, about 1-1.5 meters of filament was obtained. The first foot extruded was discarded to avoid any improper doping amounts as this proved to typically extrude clear plastic initially from the purge PLA and make a gradient to the full doped filament. The final foot of the filament was also discarded as the diameter for this portion of the extrusion was typically too small to be printed due to the lack of consistent back pressure. Shown in Figure 4-14 are the filament obtained for (left to right) raw PLA, iron oxide doped filament, barium sulfate doped filament, and gadolinium oxide doped filament.

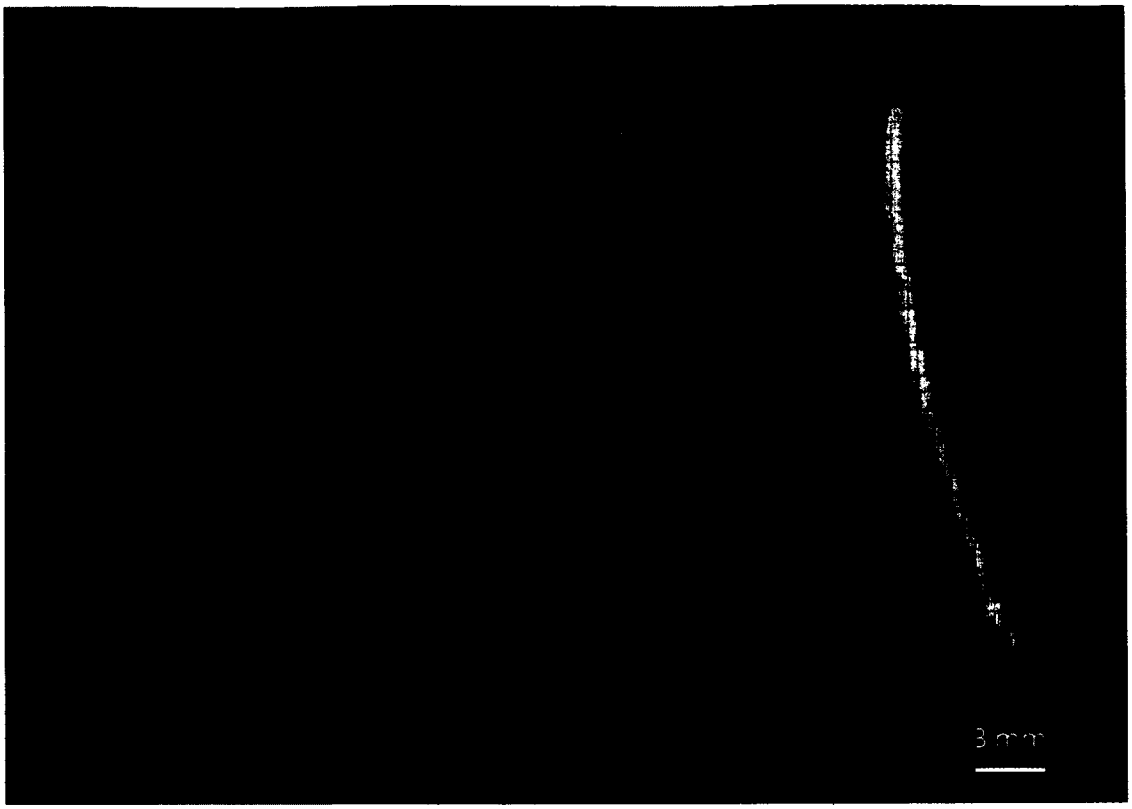

Figure 4-14: (left to right) Raw PLA, iron oxide doped 25wt%, barium sulfate doped 25wt%, and gadolinium oxide doped 25wt% extruded filaments 1.75 mm in diameter.

4.7.3 3D Fabricated Squares

Once the filaments were extruded, they were used to print 1"X1"X1 mm squares. All printing was performed on the Makerbot 2X 3D printer. Printing heads were changed prior to printing of different doped materials to avoid contamination. Further, purging of the print head was performed after each print to ensure no clogging occurred.

4.7.3.1 *3D Printed Control Squares*

Raw PLA filaments that had been extruded on the ExtrusionBot filament extruder were used to print control squares for testing against the doped squares. Shown in Figure 4-15 are these squares. It should be noted defects in each square are attributed to both the

removal of the squares from the print bed (curvature) and inherent issues with the printing process (visual differences in clarity) can be seen in these squares.

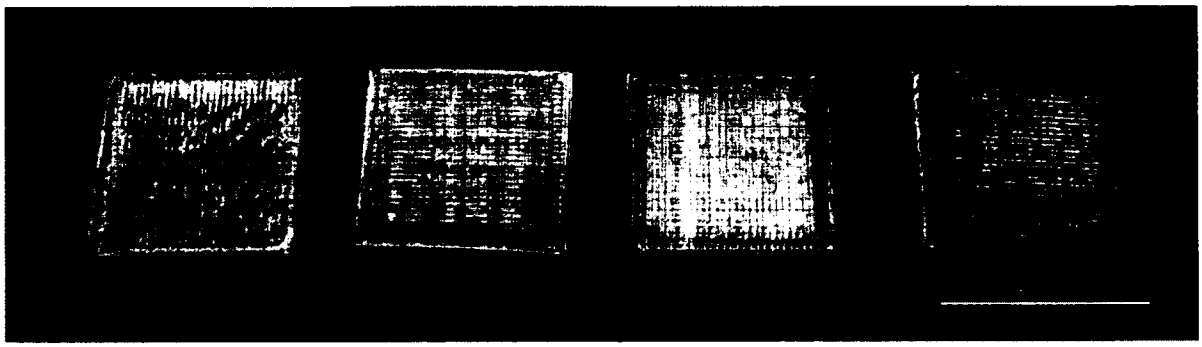

Figure 4- 15: Printed undoped PLA squares.

4.7.3.2 *Iron Oxide Doped 3D Printed Squares*

Iron oxide filaments ranging from 5-25wt% were printed under the same conditions after being extruded. Shown in Figure 4-16 are these squares with a raw PLA square for comparison. The doping percentage increases by 5wt% from left to right. Differences in print quality are attributed solely to the print head as the filament was measure for correct diameter prior to printing and found to be 1.75 mm ± 0.05 mm.

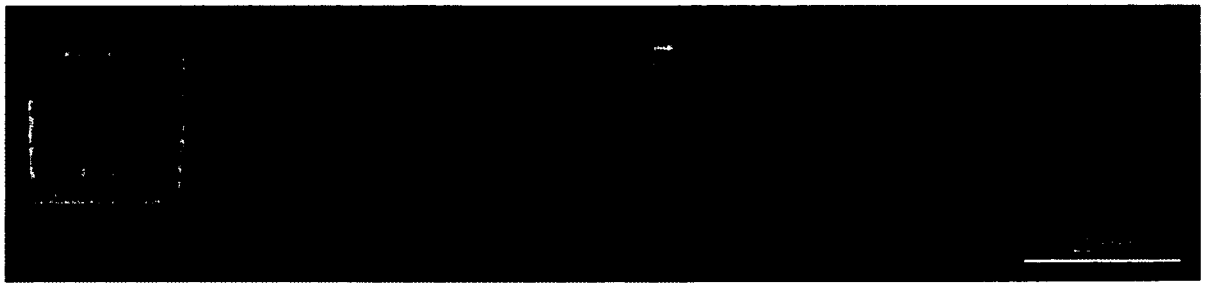

Figure 4- 16: Iron oxide doped squares 0-25wt% (left to right).

4.7.3.3 *Barium Sulfate Doped 3D Printed Squares*

Barium sulfate filaments ranging from 5-25wt% were printed under the same conditions after being extruded. Shown in Figure 4-17 are these squares with a raw PLA square for comparison. The doping percentage increases by 5wt% from left to right. Differences in print quality are attributed solely to the print head as the filament was measure for correct diameter prior to printing and found to be 1.75 mm ± 0.05 mm.

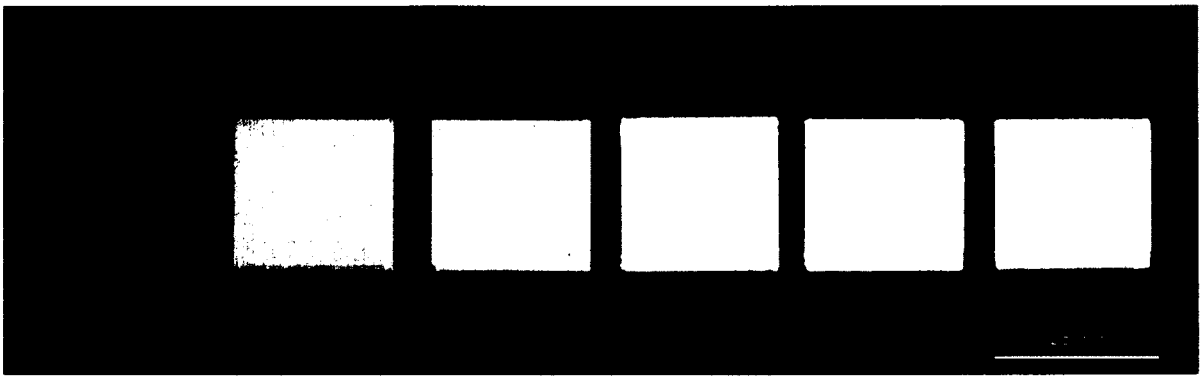

Figure 4-17: Barium sulfate doped squares 0-25wt% (left to right).

4.7.3.4 *Gadolinium Oxide Doped 3D Printed Squares*

Gadolinium oxide filaments ranging from 5-25wt% were printed under the same conditions after being extruded. Shown in Figure 4-18 are these squares with a raw PLA square for comparison. The doping percentage increases by 5wt% from left to right. Differences in print quality are attributed solely to the print head as the filament was measure for correct diameter prior to printing and found to be 1.75 mm ± 0.05 mm.

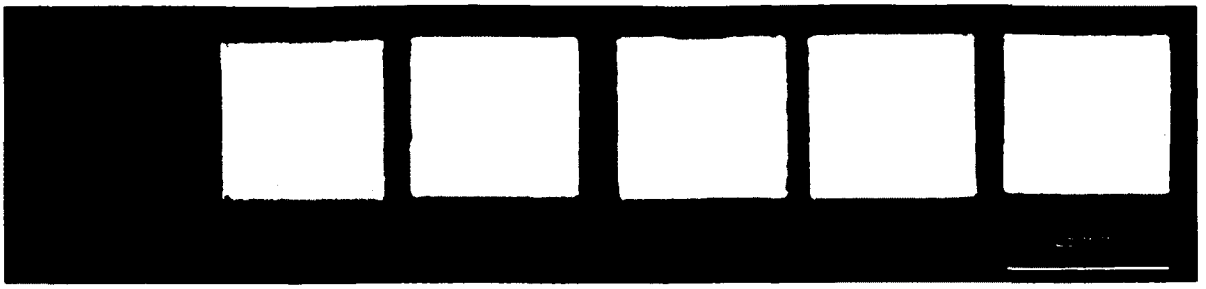

Figure 4- 18: Gadolinium oxide doped squares 0-25wt% (left to right).

4.7.4 Radiation Testing

In dealing with multiple types of radiation, a modular platform is desired that could overcome complex geometries. The method presented above is not constrained to the additives shown below. The iron oxide doped squares were used to test shielding of beta radiation, the barium sulfate doped squares to shield x-ray's, and the gadolinium was untested due to lack of access to a neutron source.

4.7.4.1 *Beta Shielding Via Iron Oxide Doped 3C Printed Squares*

Shielding for the iron doped squares was performed using a 0.5 MeV ^{90}Sr beta source. All measurements were performed using a Geiger counter. Statistics were first performed on the source by placing the source 10 mm away from the detection head. A reading is taken, the detector is removed, the signal is quenched, then the detector head is placed back 10 mm away from the source and another data point taken. This was done 10 times, and the source was found to have an average of 4860 ± 110 counts per minute (CPM).

Once the source was profiled, the source and detector were place 10 mm apart and stabilized to ensure neither would move during the testing. The squares for testing were

then placed in between the source and detector to measure the detected CPM. Shown in Figure 4-19 are the results for each doping percentage for a 1 mm thickness.

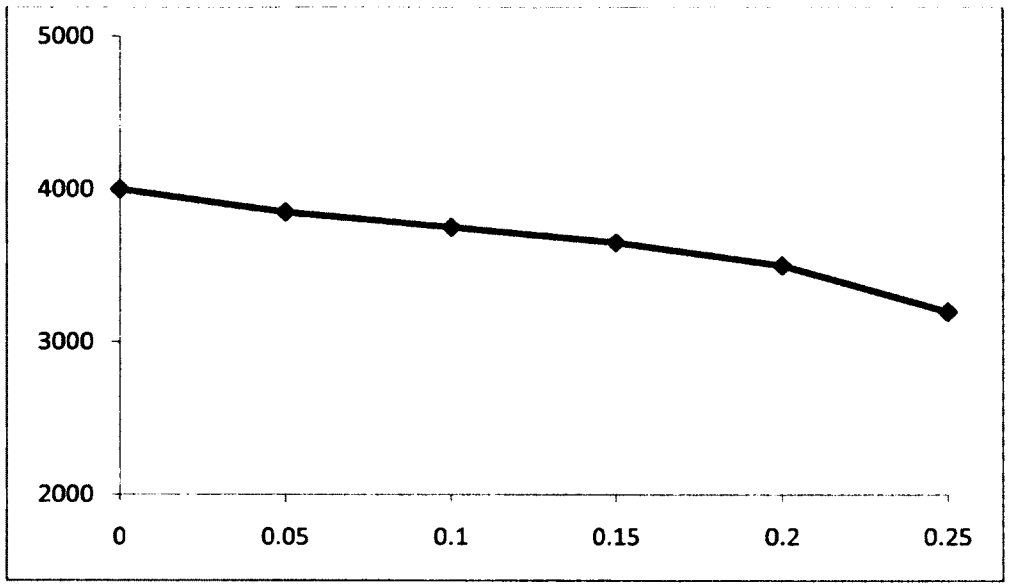

Figure 4-19: Shielding of ^{90}Sr source for 1 mm 0-25wt% iron oxide squares.

As expected, the outgoing signal of the beta radiation decreases with an increase of iron oxide. This shows not only the compatibility of this platform with shielding, but also the retention of additives through the filament manufacturing and printing process. Shielding data was then taken on successively thicker amounts of shielding material to test the response of the system. Shown in Figure 4-20 are the results for 1-5 mm thick blocking of 0-25wt% of printed material.

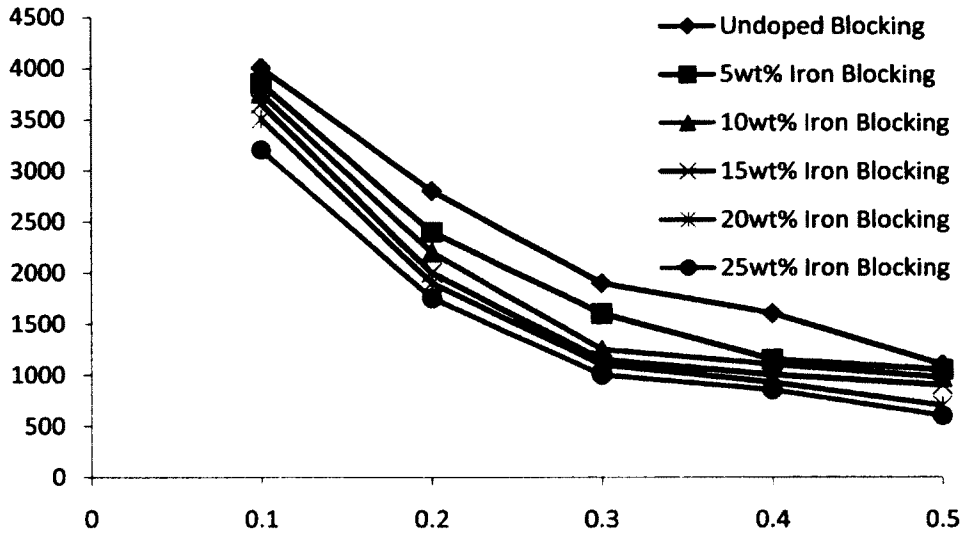

Figure 4-20: Shielding data for varied thicknesses of iron oxide doped PLA.

This data shows proves the retention of additives through the filament extrusion and printing process, and shows that greater shielding can be obtained by successively higher amounts of iron oxide. Further, it also shows that through an increase in thickness of the shielding medium, greater attenuation of the signal can be achieved.

Shielding data was also taken on 1 and 3 mm thicknesses for raw PLA and 5wt%, 15wt%, and 25wt% doping percentages and statistics performed. For 1 mm, 5 unique squares were tested for the deviation in the printing process. For the 3 mm testing, 3 squares were randomly selected and assembled to test the deviation in signal attenuation. Shown in Figure 4-21 and 4-22 is this data with statistics performed to show the deviation in signal attenuation for each of these samples.

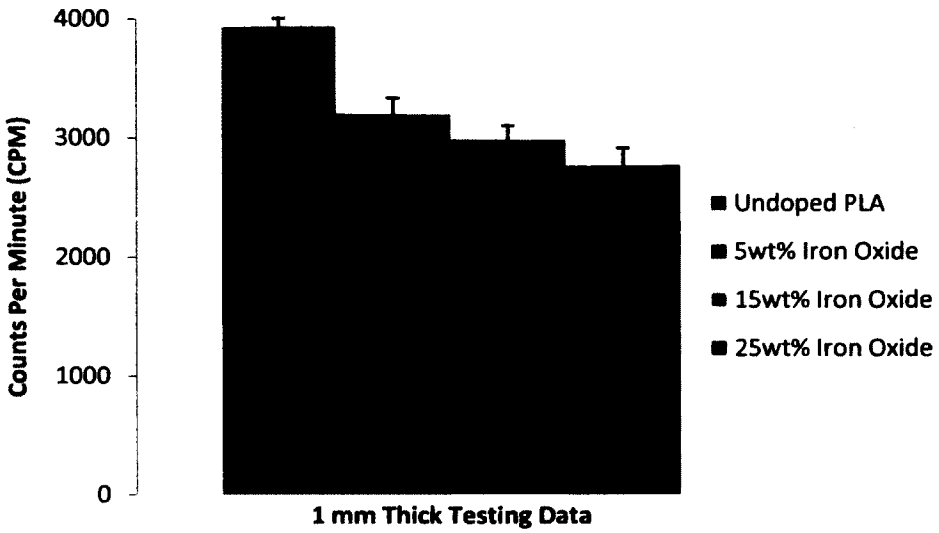

Figure 4-21: Shielding of 1 mm of raw PLA, 5wt%, 15wt%, and 25wt% iron oxide doped PLA.

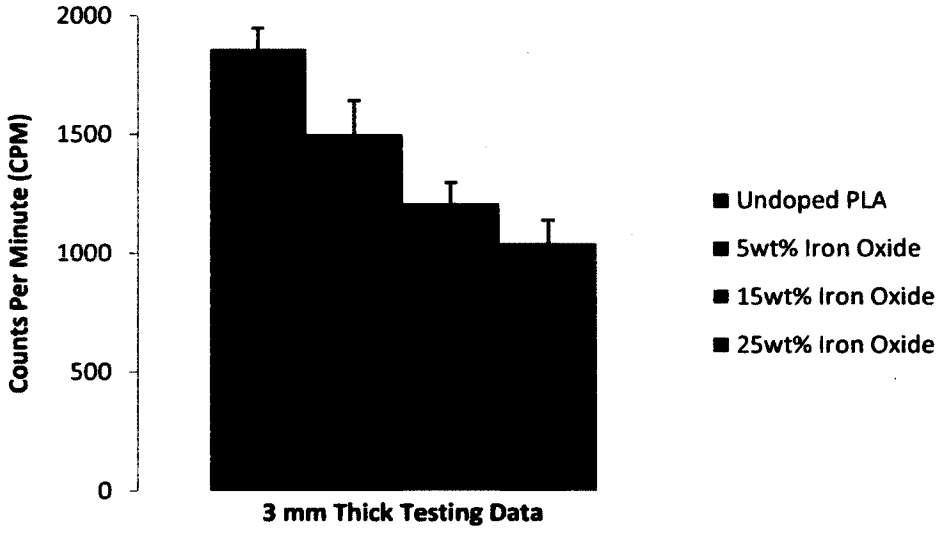

Figure 4- 22: Shielding of 3 mm of raw PLA, 5wt%, 15wt%, and 25wt% iron oxide doped PLA.

Statistics showed slight fluctuations in the shielding capabilities for both the 1mm and 3 mm sample batches. For both sets, a tighter deviation was found for the raw PLA, which is attributed to the tighter layers being achieved during the printing process. Relatively small deviations were also obtained for the iron oxide doped samples. This may in part be due to fluxuations in the source and in part due to printed layers not being as tightly bound as those found in the raw PLA.

Through this testing, it can be seen that the increase in iron contributes greater shielding properties, and that through the manufacturing of the filaments and subsequent printing, the doped material was maintained at successively higher levels. Further, it can also be seen that the increase in thickness also lends greater shielding to the system. Both of these attributes are due to the parameters seen in Equation 4.11 where the increase in n and t leads to a decrease in particles transmitted through the material.

4.7.4.2 *X-Ray Shielding Via Barium Sulfate Doped 3D Printed Square*

Barium sulfate was chosen as it is biocompatible and is already commonly used as contrast agent in medical imaging. This is due to the relatively high mass attenuation coefficient for energies found in common medical isotopes (15-150 keV). Shown in Figure 4-23 is the NIST mass attenuation graph for elemental barium.

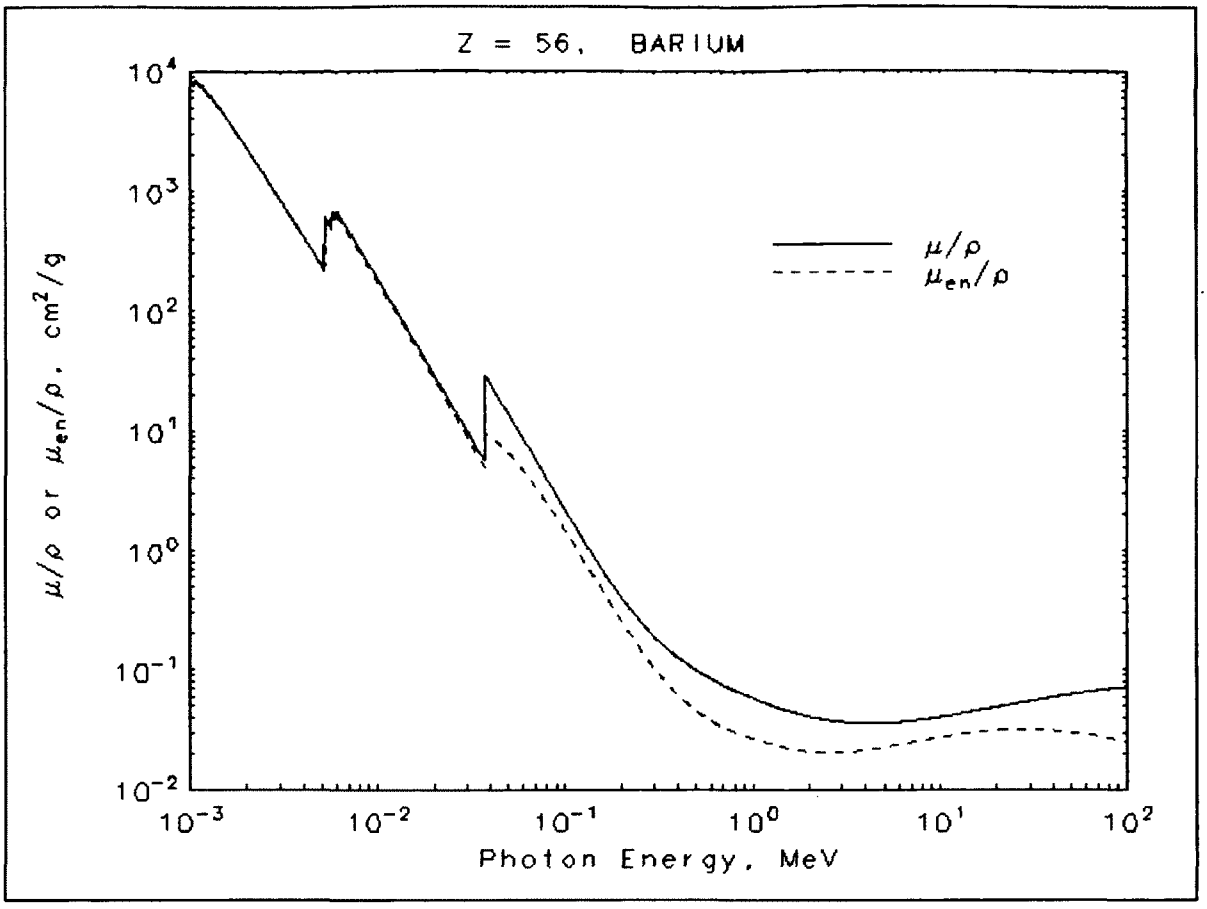

Figure 4- 23: NIST mass attenuation vs. photon energy for elemental barium [113].

For characterization of this material, four isotopes were identified that are commonly used in medical treatment. For X-rays/CT scans, technetium-99m is used with a characteristic 140 keV gamma rays that are about the same wavelength as those emitted by conventional X-ray diagnostics. For implanted radiation therapy, three isotopes were chosen that are commonly: palladium-103 (20.8 keV), iodine-125 (28.5 keV), and cesium-131 (30.4 keV).

4.7.4.2.1 X-ray Imaging

Testing of this material was done using a medical X-ray imaging machine that used tecnetium-99m as its source. Raw X-ray data is shown in Figure 4-24-4-25.

Figure 4- 24: Raw X-ray data 1mm thick for (left to right) 0-25wt% barium sulfate doped PLA and 25wt% gadolinium oxide (upper right corner).

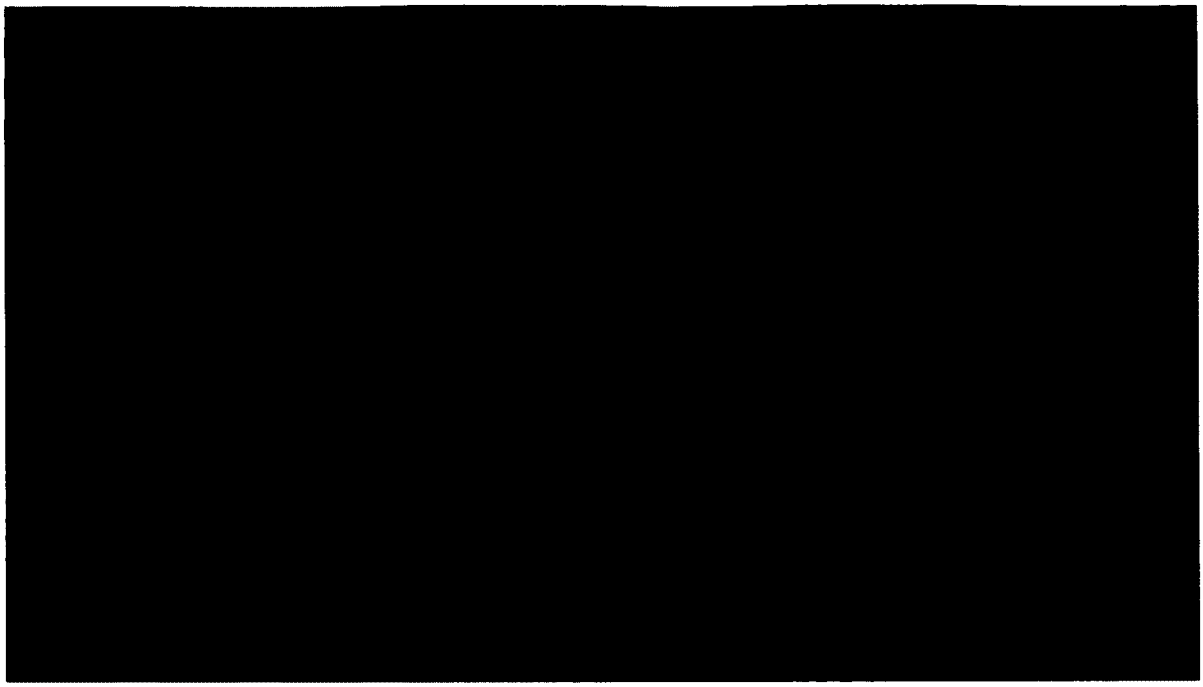

Figure 4- 25: X-ray of 2 mm and 3 mm thick 25wt% barium sulfate doped PLA.

As expected, the increasing of barium content in the PLA led to an increase in opacity. Further, inherent machining errors within the fabrication process can be seen such as holes formed from incomplete layers due to the thin nature of the square tested. This also demonstrates the greater opacity of elements with high mass attenuation coefficients as the upper right corner (25wt% gadolinium oxide) shows to be less opaque than the 25wt% barium sulfate. The increase in opacity can allow for an implant marker to be developed with customized opacity for imaging/tracking through the lifetime of the implant, allowing for ease of removal once the lifetime has expired. The print head can be modified such that errors found in the square printing will not occur for the implant, leading to a more complete sheet of opacity or customized design, as desired.

4.7.4.2.2 Modeled Shielding of Common Implanted Medical Isotopes

The three previously discussed commonly implanted radioisotopes are used for the treatment of inoperable cancers such as prostate cancer in the form of brachytherapy seeds. These seeds are small pillars that contain the given radioisotope to be implanted, and are fabricated with designed shielding such that the dose received is moderated to the standards of the treatment. Figure 4-26 shows a picture of these seeds.

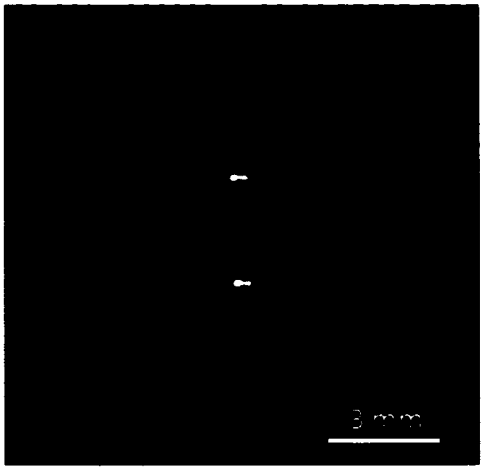

Figure 4- 26: Dummy brachytherapy seeds.

One problem with this therapy is radiation emitted out the top of the seed once implanted that can irradiate healthy tissue, leading to subsequent problems. For the common energy ranges associated with these isotopes, barium has a very strong mass attenuation coefficient. To determine this coefficient, NIST calculated values were used to model the shielding effect of barium sulfate doped PLA. First, the amount of each

element in PLA and barium sulfate had to be found. The chemical structure of PLA is $C_3H_4O_2$, and barium sulfate's is $BaSO_4$.

To find mass attenuation coefficients for the specific energies involved with each isotope, linear extrapolation had to be done as coefficients were only given for discrete energy levels. For linear extrapolation, the following formula can be used:

$$y(x_*) = y_{k-1} + \frac{x_* - x_{k-1}}{x_k - x_{k-1}}(y_k - y_{k-1}) \tag{4.23}$$

where $y(x_*)$ is the value desired, x_* is the energy to be used, x_{k-1} is the lower bound of the energy range for which there are values, x_k is the upper bound for the energy range for which there are values, y_{k-1} is the mass attenuation coefficient for the lower bound, and y_k is the mass attenuation coefficient for the upper bound. For a sample calculation, Palladium-103 will be used to find the blocking potential of raw PLA ($C_3H_4O_2$) and doping percentages of 5-25wt% Barium Sulfate ($BaSO_4$) in steps of 5wt%. Extrapolation must be done for each element; for a sample, extrapolation of barium will be performed. First, the end point mass attenuation coefficients for 20 keV and 30 keV are 29.38 cm^2/g and 9.904 cm^2/g, respectively. Plugging these into the equation, we find a mass attenuation coefficient for 20.8 keV:

$$y(20.8) = 29.38 + \frac{20.8-20}{30-20} * (9.904 - 29.38) = 28.3019 \frac{cm^2}{g}. \tag{4.24}$$

Doing similar calculations for the other elements, we find the mass attenuation coefficients to be 6.3404 cm^2/g for sulfur, 0.4271 cm^2/g for carbon, 0.3685 cm^2/g for hydrogen, and 0.8261 cm^2/g for oxygen. With these numbers, we can now find the blocking potential for each compound using the chemical formulas. For PLA ($C_3H_4O_2$), the overall blocking potential can be found as

$$3 * 0.4271 + 4 * 0.3685 + 2 * 0.8261 = 4.4075 \frac{cm^2}{g} \tag{4.25}$$

and barium sulfate ($BaSO_4$) can be found as

$$28.3019 + 6.3404 + 4 * 0.8261 = 37.9467 \frac{cm^2}{g}. \tag{4.26}$$

Using these numbers, the overall blocking potential of palladium-103 can now be found for the doping percentages of PLA. First, a sample calculation will be done for the raw PLA for squares of 1 mm thickness. The unit for thickness in the first equation are given in centimeters, thus $l = 0.1$ cm will be used. Also, as PLA density can vary from 1.21-1.43 g/cm^3, the median value of 1.32 g/cm^3 will be used. Here, it is found that

$$I = 20.8 * e^{-(4.4075*1.32*0.1)} = 11.6251\ keV \tag{4.27}$$

a reduction in energy of about 44%. Next, the same calculation can be done for a doping percentage of barium. Here, 25wt% barium sulfate doped PLA will be used. Using a density of 4.50 g/cm^3, we find

$$\begin{aligned} I &= 20.8 * e^{-(0.75*4.4075+0.25*37.9467)*(0.75*1.32+0.25*4.50)*0.1)} \\ &= 1.3901\ keV, \end{aligned} \tag{4.28}$$

a reduction of about 93%. Shown in Figure 4-27, 4-28, and 4-29 are plotted graphs showing blocking potential of 1 mm of shielding of raw PLA to 25wt% barium sulfate for each of the three isotopes.

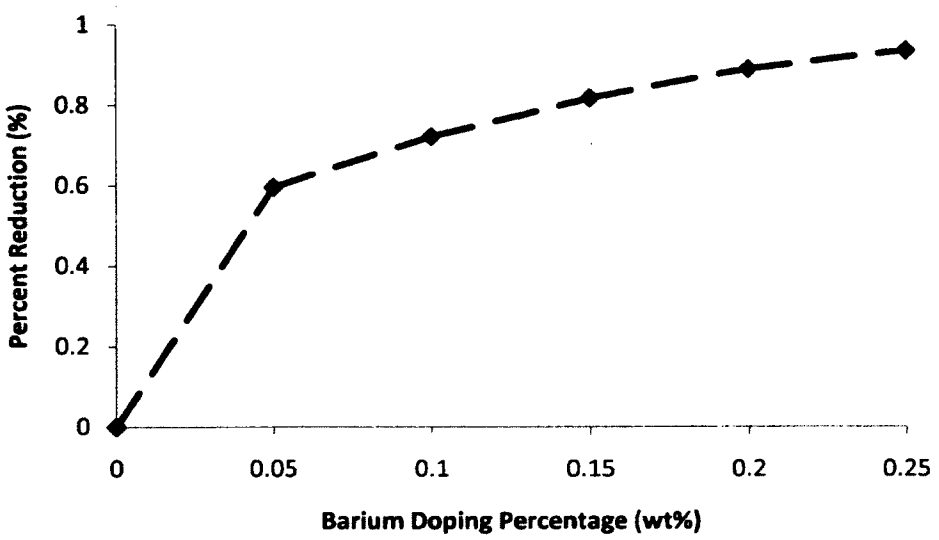

Figure 4- 27: Shielding of palladium-103 for 1 mm thick barium doped PLA.

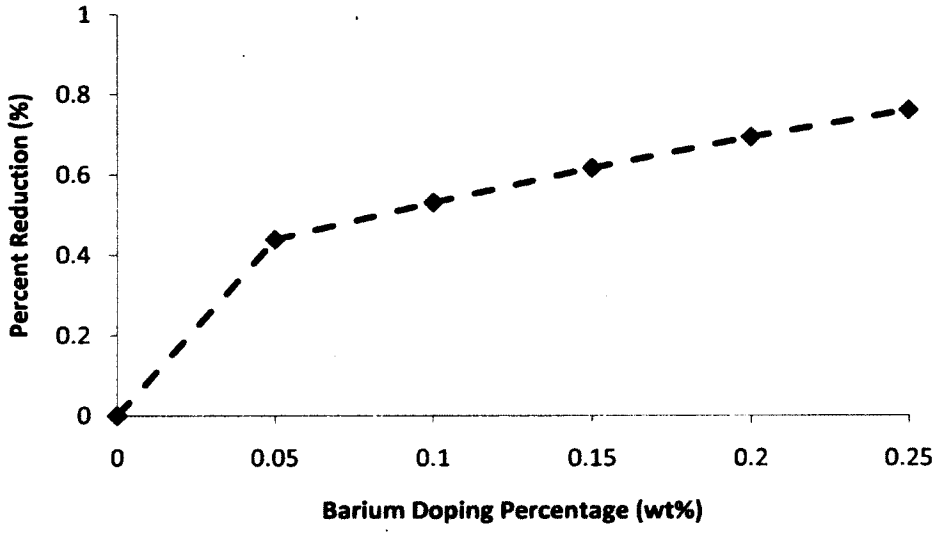

Figure 4- 28: Shielding of iodine-125 for 1 mm thick barium doped PLA.

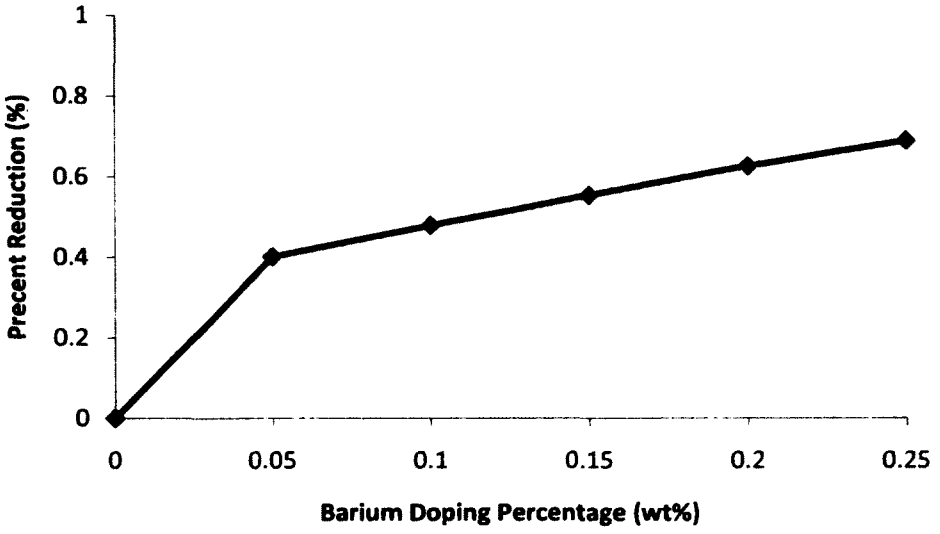

Figure 4- 29: Shielding of cesium-131 for 1 mm thick barium doped PLA.

Due to the low energy of palladium, outgoing radiation shows to be almost completely shielded by 1 mm of 25wt% barium. As the isotopes grow in energy, 1 mm of shielding is less effective. For cesium, the highest energy isotope, 1 mm of 25wt% barium doped PLA shows to reduce the signal by 68%. Should greater attenuation of radiation be needed, shielding can be achieved through using thicker material.

4.8 Conclusion

A modular method of dispersing metal nanopowders into 3D printing filament was achieved without the need for modification or fabrication of proprietary extrusion or printing equipment. The method proved to work for a range of metal compounds and weight percentages, achieving 25wt% doping before extrusion and printability were inhibited. Resolution was also maintained accurately, leading to the conclusion of the viability of the dispersing method for introducing these additives on commercially available equipment.

Radiation shielding properties of the iron oxide and barium sulfate doped 3D printed squares were tested against a ^{90}Sr and a medical X-ray imaging machine, respectively, and showed characteristic blocking of the radiation as would be expected for the doping percentages used. Further, increasing of both doping percentages and thickness for the barium sulfate doped squares led to an increase in opacity using medical imaging equipment. This proves a promising venue for tagging of medical implants for ease of locating once the implant needs to be removed. Finally, simple modeling was done for the barium sulfate doped squares, showing a potential application as blocking material for implanted radiation therapy.

CHAPTER 5

FABRICATION AND ELECTRICAL CHARACTERIZATION OF 3D PRINTED AND CAST CONDUCTIVE STRUCTURES

5.1 Introduction

The ease with which common 3D printing material was doped with metal in the previous chapter gave rise to the idea of fabricating a conductive 3D printing filament without requiring modification of the manufacturing equipment. By doping the printing plastic with a conductive powder to a sufficient weight percent, conductivity could be achieved from the inherently insulating polymer. While this has been accomplished previously using polycaprolactone (PCL), the fabrication of such a filament required the manufacture of a proprietary extruder.

In the present work, the ability to introduce graphene powder into commercial fabrication equipment is achieved. Further, these filaments were capable of printing up to 20wt% doping, however only doping between 15-20wt% proved conductive. Below this threshold, the insulating properties of the host plastic were not overcome. The polymer used (PMMA) also lead to an investigation of the graphene in commercial bone cements to test for conductivity. Successively low resistances were obtained with higher doping percentages of graphene. Increased graphene content did have an effect on the mechanical properties, leading to less rigid structures at higher weight percentages.

5.2 Design and Objectives

The experimental design will look at the effects of adding conductive dopants to both the filament extrusion/printing process and the casting process of commercially used bone cements. These structures will be tested for various electrical characterizations as appropriate for the structure. The following sections breakdown the design objectives into specific areas.

5.2.1 Filament Extrusion Objective

A method of introducing the conductive additive will be explored. This method will examine polymer choice and the effects of introducing such an additive on the extrusion process. Further, the ability to fabricate 3D printing filament that is the proper diameter and of use in commercial fused deposition 3D printers will be developed.

5.2.2 3D Printing and Additive Manufacturing Objective

The ability to 3D print a custom extruded conductive filament will be demonstrated. This method will utilize commercially available 3D printing equipment, and take consideration such that no modification of the 3D printing equipment need be performed.

5.2.3 Bone Cement Casting Objective

Fabrication of conductive bone cement constructs will be demonstrated. This method will use commercially available PMMA/MMA bone cements without barium added to test the effects of a conductive additive on the fabrication and electrical characteristics of these bone cements. Observations on the influence of the dopant to the casting process will be discussed.

5.2.4 Resistance Characterization Objective

Resistivity will be characterized for both 3D printed constructs and bone cement structures. A multimeter and a resistive Wheatstone bridge will be used.

5.2.5 Capacitance Characterization Objective

Capacitance will be characterized for both 3D printed constructs and bone cement structures. A capacitance meter and a capacitive Wheatstone bridge will be used.

5.2.6 Piezoresistivity Characterization Objective

Piezoresistivity will be characterized for both 3D printed and bone cement structures. A set angle of deformation will be chosen such that all samples will be deformed uniformly, and resistance measurements will be taken via multimeter.

5.3 Fabrication

To achieve the conductive constructs, multiple steps had to be considered. First, because of the constraint of no modification to the equipment, a method of dispersing the conductive additive into the filament had to be considered. The filaments also had to be manufactured to the proper diameters and an additive concentration had to be such that the conductivity was achieved without inhibiting the printability. Once the filaments were achieved, printing of simple constructs had to be accomplished using a commercial 3D printer with no modification. For the PMMA/MMA bone cements, the additive had to be considered such that conductivity was achieved without inhibiting the polymerization of the PMMA/MMA, inhibiting the mechanical properties of the bone cement.

5.3.1 Graphene Coating of Pellets

As stated before, one issue with the introduction of additives the potential for a gradient to be achieved during the filament process, especially where a bulk plastic pellet and a powdered additive are used. To achieve the introduction of the graphene into the filament, the above stated method was attempted with surface suspension via silicone oil being used. This worked for about 7wt% doping of the graphene onto the surface of the pellets, however many issues were found with this method of introduction of the graphene.

First, the density of the graphene powder is so low that the amount needed to achieve the 5wt% doping of filament entailed the use of three layer-by-layer coatings of silicone. Secondly, beyond this threshold, the oil did not stick to the three layers of graphene because it is very slippery. Finally, the amount of static generated in the vortexing process led to large amounts of lost graphene. Upon extrusion of these 5wt% pellets, the resulting filaments were found to still be insulating, leading to the conclusion that significant losses of the graphene occurred in both the coating and extrusion process.

5.3.2 PMMA/Graphene Powder Extrusion

In previous work, the extrusion of PMMA powder was found to be achievable using the ExtrusionBot by only modifying the extrusion temperature to extrude at 90 °C rather than the 175 °C required for PLA. To this end, PMMA filaments were extruded at varying doping percentages (0-25wt%) of graphene via mixing of the PMMA powder with the graphene powder, then vortexing. This ensured and even dispersion of material through the sample.

5.3.3 Construct Design and Printing

To characterize the various electrical characteristics of printed constructs, two differing layouts were manufactures. The first was a simple square pillar 10 mm tall and 5 mm in width and depth. Because the electrical characteristics may vary depending upon the fabrication of the object two different orientations of the pillar were printed, one horizontal and one vertical as shown in Figure 5-1.

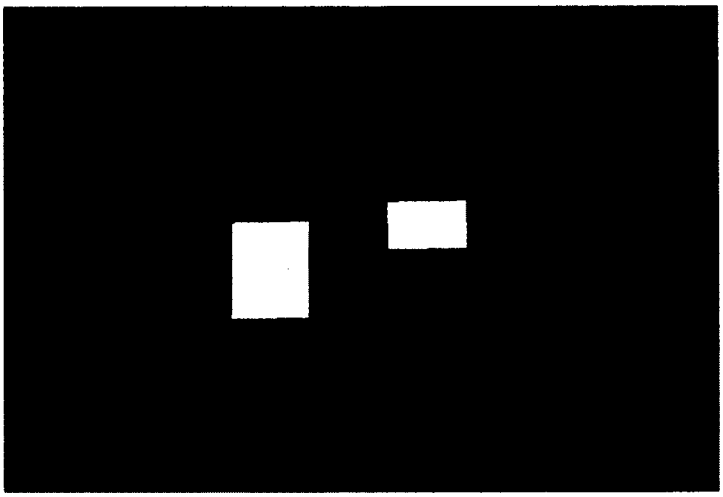

Figure 5-1: CAD representation of horizontal (left) and vertical (right) printed pillars.

To characterize the piezoresistivity of a printed body, a design that could easily bend was necessary. Varying layer thickness from 0.2-1 mm were fabricated of the design shown in Figure 5-2. This was decided upon due to the ease with which the leads of a multimeter could be attached to the extensions from the body, and then bending around the center of the bridge could be performed. Dimensions for this object are 15 mm long extensions with a 20 mm long bridge portion.

Figure 5-2: Construct for testing piezoresistivity of 3D printed conductive structure.

5.3.4 Casting of Conductive Bone Cements

As PMMA is the basis for bone cements, it was also desired to test how the introduction of graphene into a normally cast PMMA/MMA bone cement would affect the conductivity of the structure. To this end, two different constructs were fabricated via casting of the PMMA/MMA/graphene mixture: a 12 mm high, 6 mm diameter pillar and a dog bone fabricated for piezoresistivity testing with specifications of 75mm in length and 5 mm thick and are shown in Figure 5-3. The other dimensions were taken from literature that are commonly used in the mechanical testing of these bone cements.

Figure 5-3: Cast PMMA/MMA/graphene bone cement dog bone (left) and pillars (middle and right).

Varied doping percentages were used ranging from 0-25wt% graphene. In considering these doping percentages, a 10 gram batch of graphene/PMMA was used with the ratios of material varied accordingly. To these mixtures, 5 mL of MMA monomer was added to achieve the polymerization for 0-20wt%. For 25wt%, this amount of MMA was found to be too low to achieve full polymerization, so for this set of samples, 6 mL of MMA was used instead. During the curing process, the MMA monomer evaporates from the sample, causing mild shrinkage throughout the body. This

was found to be on the order of 1.5 mm ± 0.3 mm for the 0-20wt%, and 2.5 mm ± 0.4 mm for the 25wt%. The curing time for undoped bone cements is on the order of one hour. With the introduction of the graphene, this time was increased to about 24 hours for full curing. This is most likely due to the inhibited polymerization of the PMMA/MM due to the added graphene. 5wt%, 10wt%, and 25wt% showed to have the rigidity comparable to the control bone cements. 15wt% and 20wt% batches proved to be more flexible, leading to a conclusion that full polymerization was not achieved for the PMMA/MMA. All samples, both pillars and dog bones, were cast from the same batch of PMMA/MMA/graphene. Variances found in data is due to the uneven dispersion of graphene throughout the bulk material.

5.4 Testing

This project required the use of the equipment described in Chapter 4 for the filament extrusion and printing, and wax molds with which to cast the PMMA/MMA/graphene mixtures. As PMMA is naturally insulating, no controls could be manufactured for a baseline other than to confirm the extruded and cast PMMA was in fact insulating. Measurements for bulk conductivity were taken every step along the manufacturing process to ensure conductivity was achieved. Filament extrusion proved to only be conductive at doping percentages above 15wt%. Casting of the bone cements found measurable resistances for the cast PMMA/MMA mixtures at 5wt% doping.

5.4.1 Pellet Coating and Extrusion Process

As discussed above, the PLA pellet coating process discussed in Chapter 4 was initially used to attempt the fabricate the conductive filaments desired. Issues arose in the retention of the graphene powder, leading to a maximum doping of the PLA through this

method to be restricted to about 5-7wt%. At this low doping concentration, conductivity was not achieved, thus a different method for manufacturing the conductive filaments had to be developed.

5.4.2 PMMA Powder Extrusion

PMMA powder was vortexed with the graphene powder to ensure and even dispersion of the graphene into the powdered polymer. Extrusion was achieved through the use of the ExtrusionBot filament extruder at 175 °C. Initial filaments (0-10wt% graphene) were very course to the touch and showed variations in thickness of about 1.75 ± 0.125 mm; for 15-20wt% of graphene the filaments were found to have a smooth surface with diameters of 1.75 ± 0.05 mm, the same as that found in commercial filaments. Extrusion problems were encountered at 25wt%, where the amount of graphene severely overcame the amount of polymer in the batch, leading to inhibited filament extrusion. Initial and final portions of the filament were again discarded to avoid improper doping between batches.

5.4.3 Printer Testing and Controls

Prior to printing constructs, the 3D printer was calibrated and returned to factory setting to ensure minimal manufacturing error was introduced into the system. The MakerBot Replicator 2X used was purchased from the manufacturer and used for printing purposes of this project. All control constructs were manufactured prior to any doped constructs to avoid contamination within the print head. Constructs of sequentially higher doping were printed at a time, with purging of raw PLA done between each print. Print heads were changed between each dopant batch to ensure no cross contamination occurred. Before printing of doped filaments, the printer was used to manufacture

multiple small constructs and these weights were compared to see inherent manufacturing error within the process. These constructs showed weight differences between 1%-5% for a sample batch of ten objects.

5.4.4 Resistance Testing of Filaments and Constructs

To ensure conductivity was achieved during the manufacturing process, a multimeter was used to measure resistance for the filaments after extrusion and of the construct after printing. Filaments were found to only be conductive for 15wt% and 20wt%, with the extrusion of the 25wt% being a failure. One inch sections of filament were cut off of the bulk filament to test the resistance of the filament over a set amount of filament, and when a measurable resistance was obtained, the filament was claimed conductive.

For the constructs, simple resistivity measurements were taken for the bulk using a multimeter to ensure conductivity was achieved. After this, a resistive Wheatstone bridge was developed to measure the resistance of the bulk construct. A schematic for this circuit is shown in Figure 5-4, where R1 and R4 are set value resistors, R3 is the measured construct, and R2 is a variable resistor. For this circuit, when the variable resistor matches the resistance of the construct, the measured output voltage will be zero, and can then be calculated using the relationship $R_3 = R_4 * (\frac{R_1}{R_2})$.

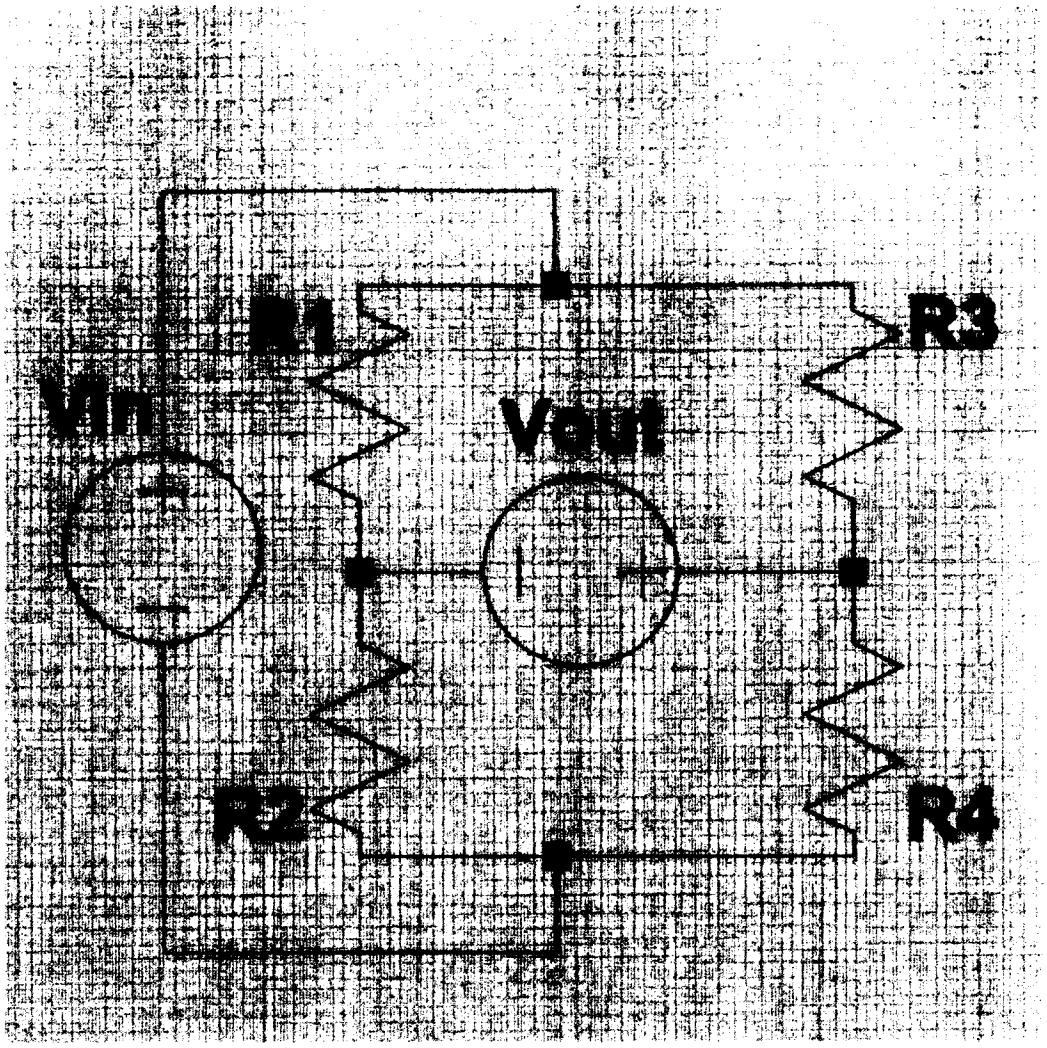

Figure 5-4: Schematic for a resistive Wheatstone bridge.

5.4.5 Capacitance Testing of Printed Constructs

Due to the nature of manufacturing the 3D printer uses, characterization of capacitance between layers is useful when designing a printed circuit using this material. To this end, a capacitive Wheatstone bridge was used, and capacitance along different faces were measured using the circuit shown in Figure 5-5 where C1 is a set value capacitor, Cx is the measured construct, R1 is a set value resistor, and Rvar is a variable

resistor. As with the resistive version, the output voltage of the circuit will be zero when the impedance for the top half of the circuit is equal to the impedance of the bottom half. Once a zero voltage is obtained, the capacitance of the construct can be found using the relationship $C_x = C_1(\frac{R_1}{R_2})$.

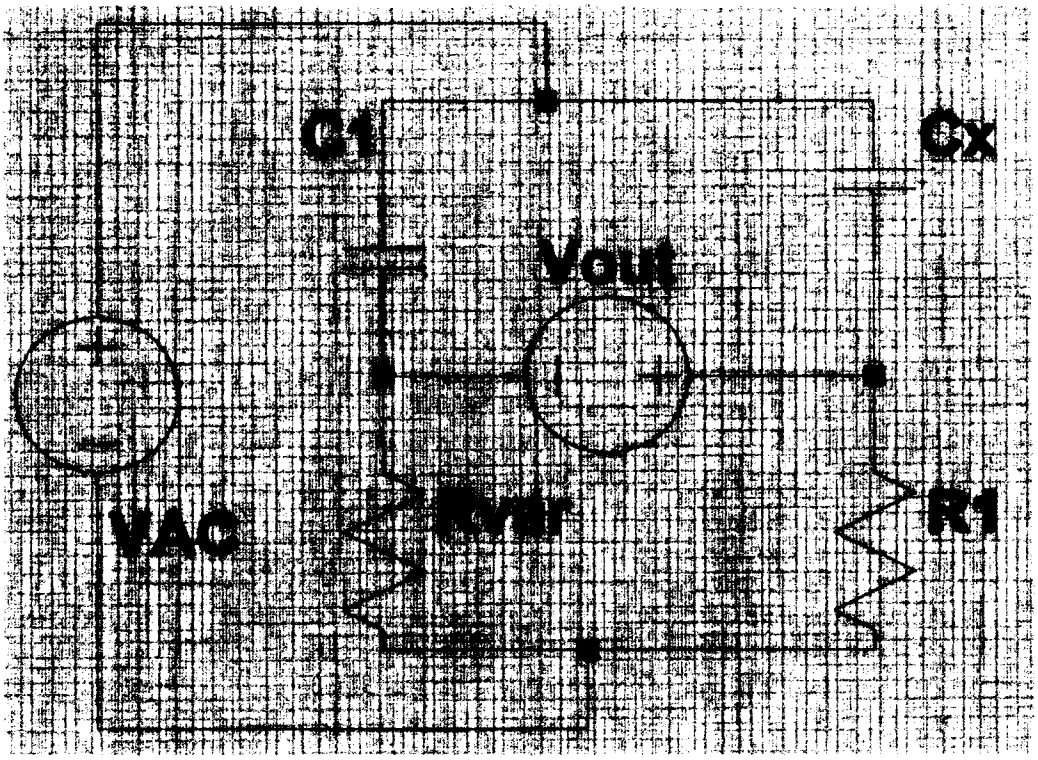

Figure 5-5: Schematic for a capacitive Wheatstone bridge.

5.4.6 Piezoresistivity Testing of Printed Constructs

Piezoresistivity testing of the printed constructs was performed using a multimeter due to the ease with which the construct could be measured. A set angle of deformation was used to ensure all samples were deformed uniformly. Testing was performed on five

samples of varying thickness ranging from 0.2 mm (one printed layer) to 1 mm (five printed layers).

5.4.7 Resistance Testing of Graphene Doped Bone Cements

Testing of the conductive bone cements was done using only a multimeter. This was due to the varied sizes of constructs. For the pillars, resistance measurements were taken across the top and bottom for a full body measurement. For the dog bones, resistance measurements were taken on the larger pads of the dog bone at the sample place for each sample so as to measure the bulk resistivity of the construct.

5.4.8 Piezoresistivity Testing of Graphene Doped Bone Cements

Piezoresistivity was measured for the dog bone constructs at all loading percentages. Each dog bone was flexed to an angle of (insert here) and resistivity measurements were taken from the pads again. Electrical tape was used on the caliper to ensure resistance measurements were only across the body of the cast dog bone. Finally, resistance measurements were again taken on the dog bone after being relaxed from flexing to see how the resistance characteristics had changed.

5.5 Results and Discussion

Methods to create and manufacture 3D printable conductive filaments and castable conductive bone cements were developed. First, the results of the coating of PLA method will be discussed as pertains the introduction of graphene. Next, the fabrication and extrusion of the PMMA/graphene mixture will be discussed, and observations of the manufacturing process will be presented. Casting of the PMMA/MMA/graphene doped bone cements will also be discussed. Finally the

manufacture of 3D printed constructs and the cast bone cements will be shown, and characterization of their resistivity and capacitances will be performed.

5.5.1 Graphene Coated Pellets

The manufacturing process discussed at length and used for the coating of metal powders in Chapter 4 was initially used to see the applicability towards graphene powder with the intention of extruding a conductive PLA based filament. Issues arose in the low density of the graphene that required large amounts of additive to be used to achieve a desired weight percentage, as well as a low retention of material beyond 5wt% doping. Significant losses also occurred during the vortexing process due to static electricity generated between the powder and the plastic container. 5wt% pellets were extruded, however no measurable resistivity was achieved of the filament. This is primarily due to the low uptake of the amount of material, limiting the amount that can be doped.

5.5.2 PMMA/Graphene Extrusion

To overcome issues with the retention of the graphene with the PLA oil coating method, a method was devised to use PMMA powder as the plastic as previous work has shown the extrusion and printability of this material. For this work, 20 grams of PMMA powder was measured out, then graphene powder was added by weight to fabricate filaments at varied doping percentages of 5-25wt% in steps of 5wt%. Shown in Figure 5-6 is a mixture of PMMA and graphene at 10wt%.

Figure 5-6: PMMA powder mixed with 10wt% graphene.

5.5.3 Extruded Filaments

Previous work has shown the incompatibility of powdered extrusion using the ExtrusionBot. PMMA has proven the exception with viable filaments being achieved within the diameter needed. This is primarily due to the amount of powder used, and that it has a lower density than PLA (1.18 vs. 1.32). This lower density leads to a larger amount of material being used during the fabrication process, providing additional backpressure to the extrusion system necessary for the fabrication of the filament. All extrusion was performed at 175 °C for these filaments.

During extrusion, the first foot was discarded to avoid any improper doping amounts as this filament proved similar to the last in a gradient of dopant being achieved initially before going to a more uniform filament. The final foot was also discarded as

the diameter was too small for proper printing specifications. For the 20 gram batches fabricated, about 1-1.5 meters of usable filament were obtained that were of the proper diameter (1.75 ± 0.05 mm).

During the extrusion process, there were noted visual differences of the filaments as pertained to the doping percentage. 0-10wt% filaments proved to be rough to the touch, and visually they had streaks along the body from contact with the extrusion dye. As the percentage of graphene increase to 15-20wt%, a smooth filament was obtained that also had a shiny exterior. Finally, the 25wt% extrusion proved a failure as a proper diameter could not be obtained, and the filament was too soft to the touch, leading to fracturing of the filament into unusable sections. This problem at 25wt% is primarily due to the amount of graphene that was used to dope the filament to this concentration; by volume, the graphene overtook the PMMA, leading to an unbalanced mixture that did not allow for full encapsulation of the graphene within the PMMA, and average diameters of about 2.1 mm ± 0.1 mm. Only the 15wt% and 20wt% filaments showed conductivity. Lower thresholds than this were unable to overcome the insulating nature of the PMMA. Shown in Figure 5-7 are the manufactured filaments.

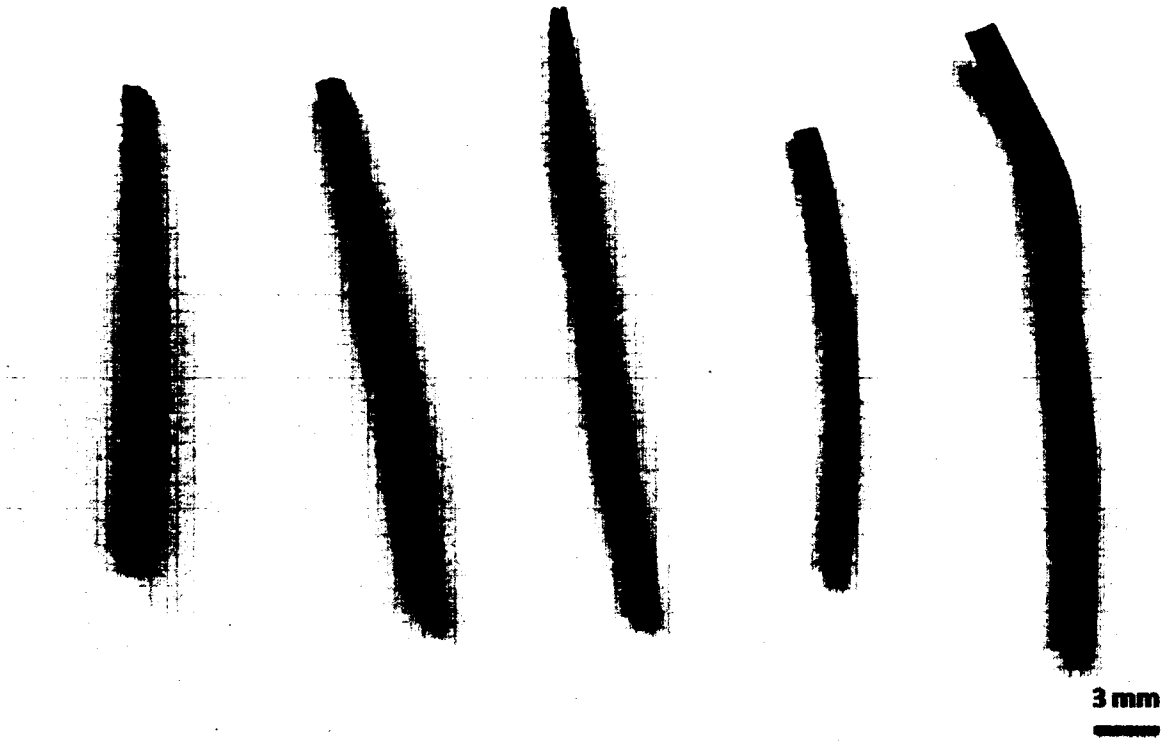

Figure 5- 7: Extruded graphene doped PMMA filaments.

The resistance of these extruded filaments was tested to ensure conductivity was achieved. As previously discussed, 0-10wt% proved to be completely insulating, however as the doping level reached 15wt%, a measurable resistance was achieved. Ten one-inch segments were cut from the filament to statistically quantify the characteristics of both the 15wt% and the 20wt%, and were found to have resistances of 1.43 MΩ ± 0.4 MΩ and 59 kΩ ± 7 kΩ, respectively.

5.5.4 3D Fabricated Constructs

Once the filaments were extruded, they were used to print the constructs described and shown in Section 5.3.3. All printing was performed on the Makerbot 2X 3D printer at 190 °C. Print heads were changed prior to printing of the different levels of

doped materials. Purging of the print head was also performed after each print to ensure no clogging occurred. Shown in Figures 5-8 and 5-9 are sample constructs for 15wt% and 20wt%, respectively. Of note is the significant lower quality of the 15wt% which was a result of poor adhesion during the printing process attributed to slower cooling than the 20wt%.

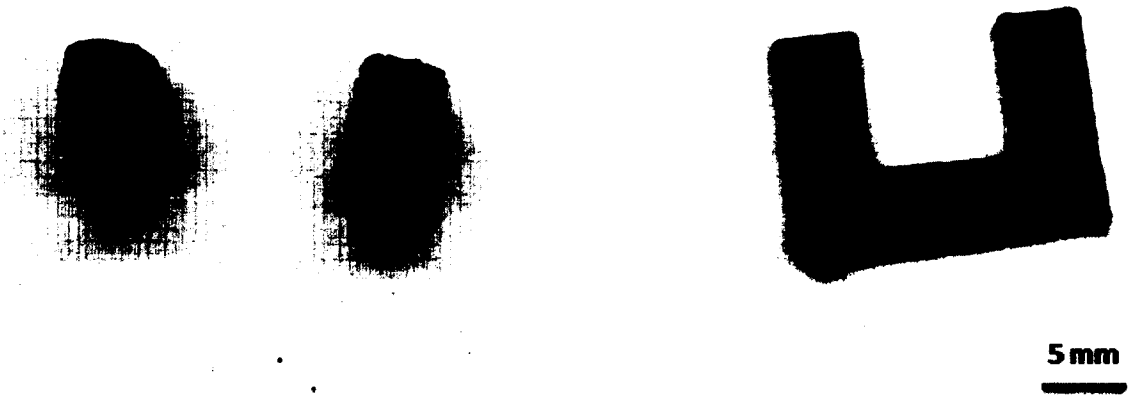

Figure 5- 8: 15wt% graphene doped PMMA constructs.

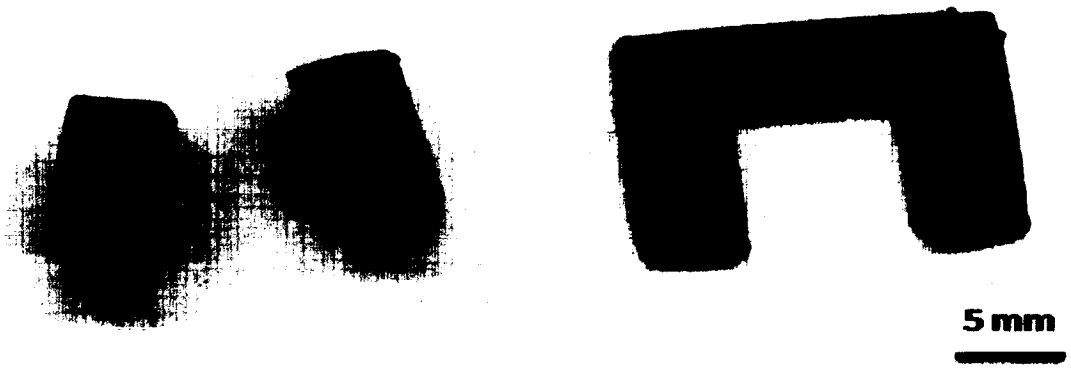

Figure 5- 9: 20wt% graphene doped PMMA constructs.

5.5.4.1 *3D Printed Square Pillars*

To characterize the difference in electrical characteristics of the printing process, 10 mm high, 5 mm width square pillars were printed in two configurations as described in Section 5.3.3. The two different configurations were to test how the stacking of layers through the printing process affected the electrical characteristics when measurements were taken across different faces. A 5 V DC power supply was used to characterize the resistances using the resistive Wheatstone bridge previously discussed in Section 5.4.4. The 15wt% proved to print in a lower resolution than the 20wt%, most likely due to a lower adhesion to the printing platform. Shown in Figure 5-10 are printed pillars for the 15wt% and 20wt% filaments printed in both configurations.

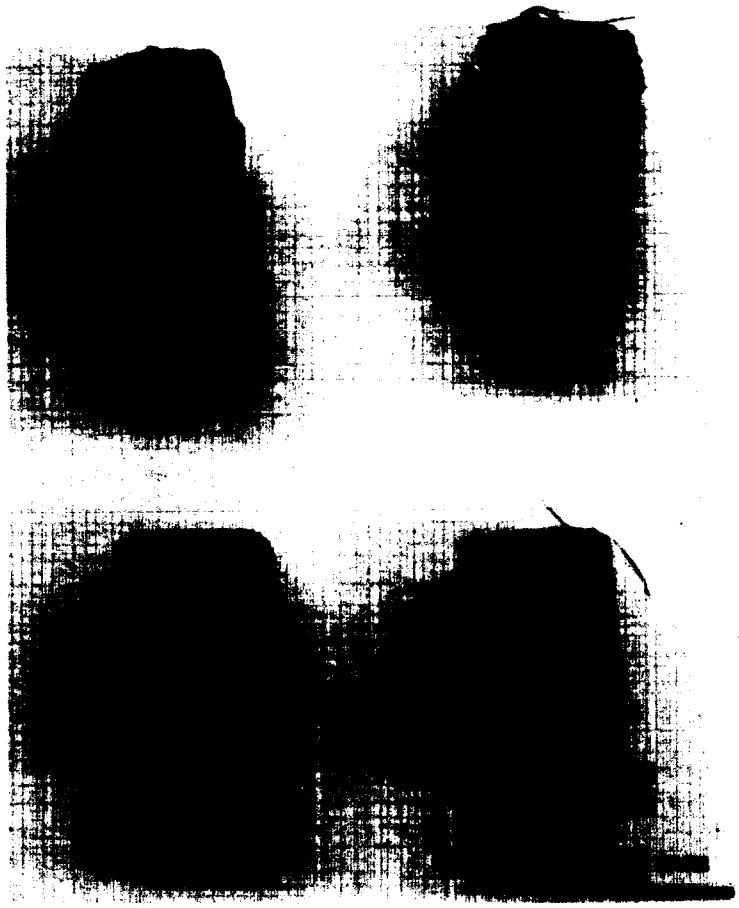

Figure 5-10: 3D printed pillars for electrical characterization for 15wt% (top) and 20wt% (bottom) printed horizontally (left) and vertically (right).

5.5.4.1.1 Resistance Testing of Vertically Printed Pillars

Because of the different geometries obtained for each of the pillars, multiple resistance measurements were taken on differing faces to ensure proper characterization of the sample. For the vertically printed pillars, measurements were taken across the length of the body and taken across the mid section. These differing measurements were done to see how the stacking of the conductive layers of polymer affected the resistance of the printed construct. These measurements are shown in Figures 5-11 and 5-12.

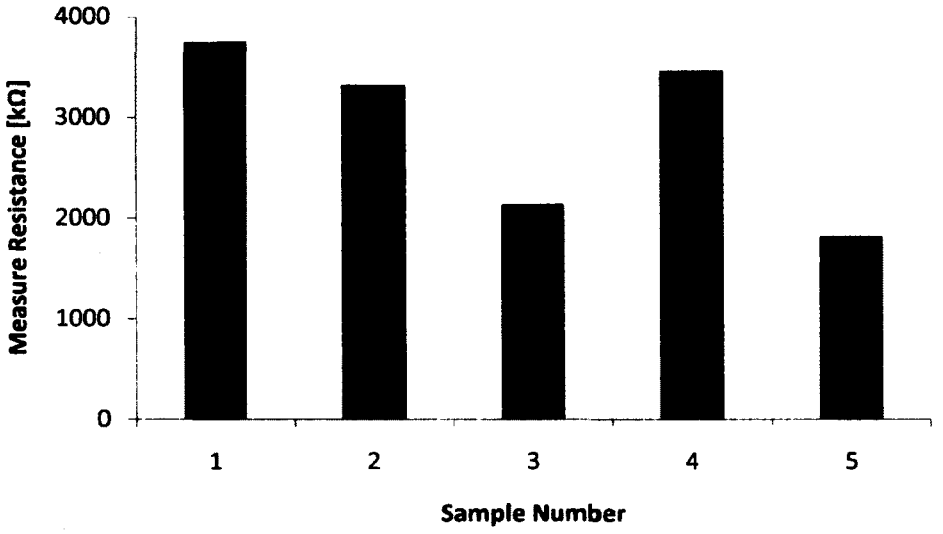

Figure 5- 11: Resistance measured across length of the 15wt% vertical printed pillar.

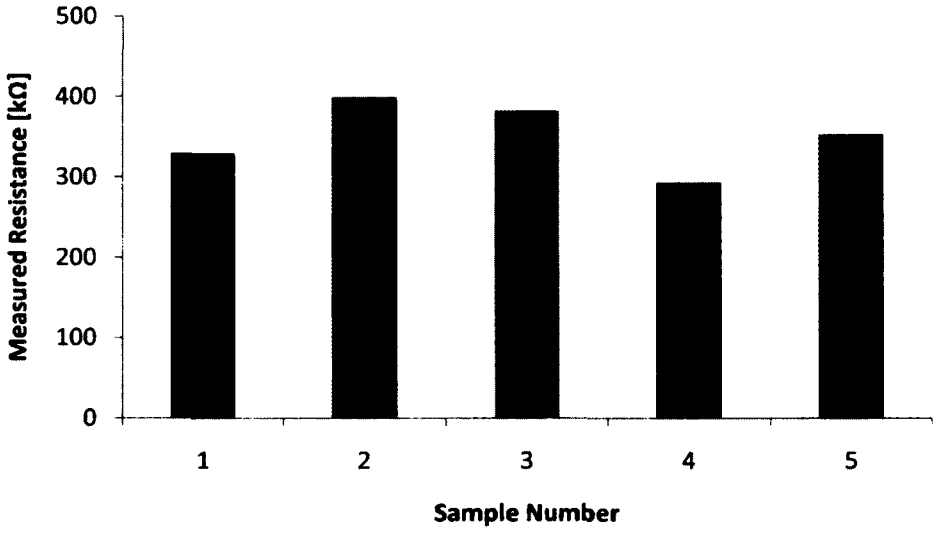

Figure 5- 12: Resistance measured across the middle of the 15wt% vertical printed pillar.

Relatively high variances in resistance measurements were obtained when measuring along the length of the pillar. Much higher resistances were found for this

measurement as compared to the middle measurements due to the orientation of the printed layers and the increased thicknesses. The same measurements were performed for the 20wt%, and are shown in Figures 5-13 and 5-14.

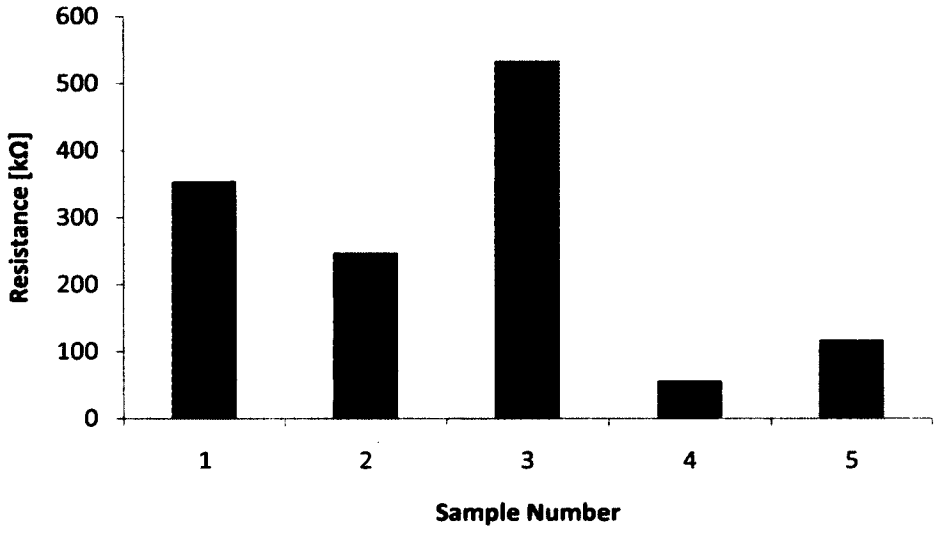

Figure 5- 13: Resistance measured across the length of the 20wt% vertical printed pillar.

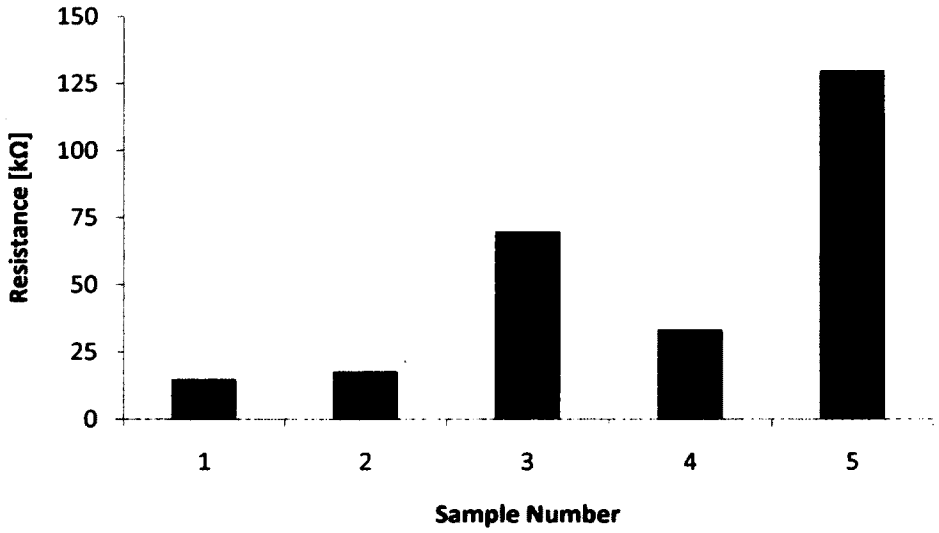

Figure 5- 14: Resistance measured across the middle of the 20wt% vertical printed pillar.

Again higher resistances were found for the length measurements than those across the body, but the results show a significant decrease in resistance for the constructs printed at 20wt% rather than 15wt%. This is partially due to the greater increase in conductive additive and partially due to printing defects that occurred. As previously mentioned, adhesion was greater for the 20wt% than the 15wt%, leading to a higher quality of printing.

5.5.4.1.2 Resistance Testing of Horizontally Printed Pillars

For the horizontally printed pillars, measurements were taken across the length of the pillar, and across the two shorter sides due to the differences in layer alignment. Figures 5-15, 5-16, and 5-17 show resistance measurements for the pillars printed at 15wt%.

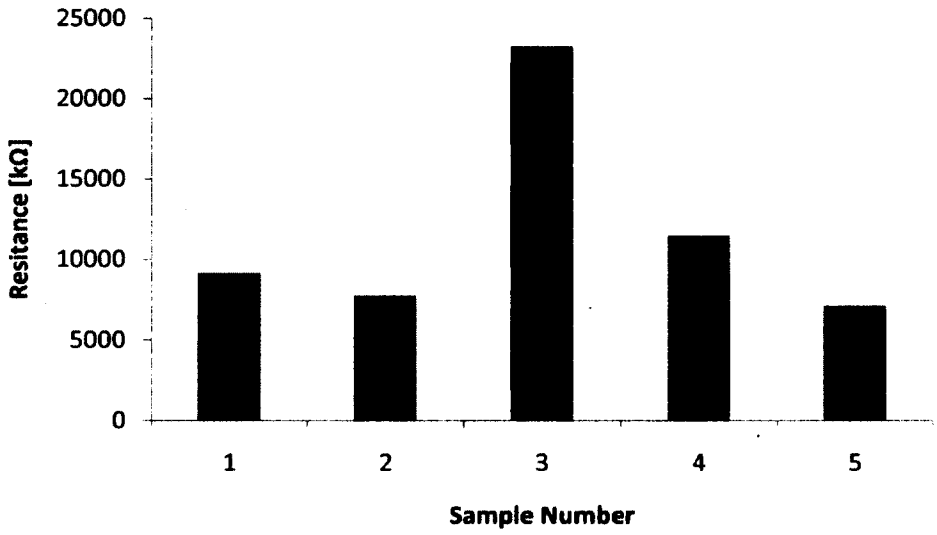

Figure 5- 15: Resistance measured across length of the 15wt% pillars.

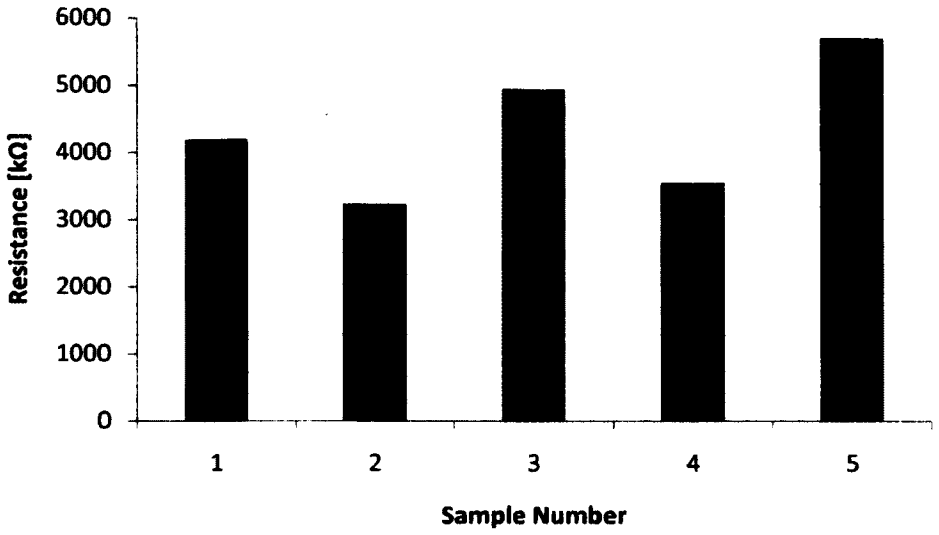

Figure 5- 16: Resistance measured across the printed face of the 15wt% pillars.

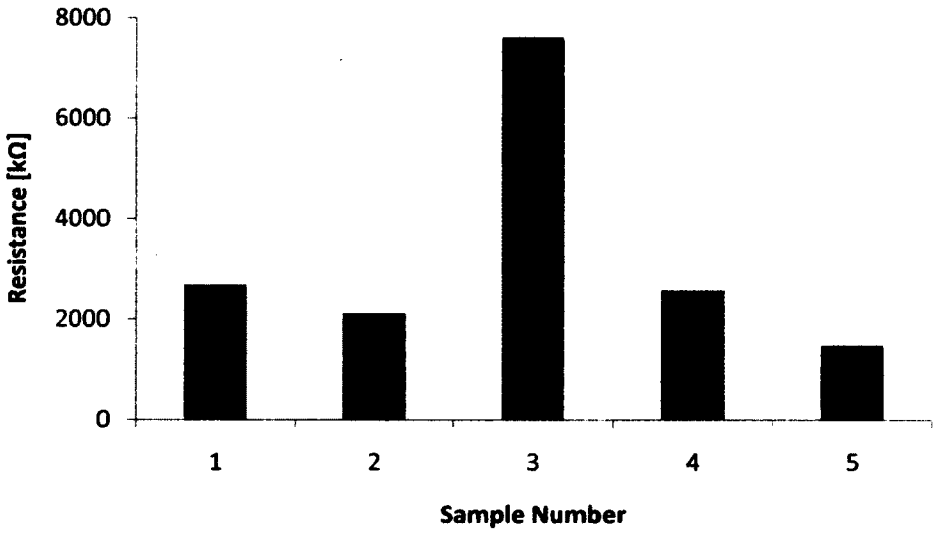

Figure 5- 17: Resistance measured across the perpendicular printed face of the 20wt% pillars.

Again resistance was highest along the longest portion of the printed structure, as expected. The lowest resistance was the shorter side of the pillar perpendicular to the stacking of printed layers. This is due to the tighter bonding of the printed filament per

layer than those in different printed layers, leading to a more cohesive conductive network throughout the printed object. All resistances measured were over 1 MΩ. This is partially due to the amount of dopant barely overcoming the inhibiting properties of the polymer and partially due to the poor print quality of the constructs manufactured. For comparison of these qualities, the same tests were performed for 20wt% constructs, with results shown in Figures 5-18, 5-19, and 5-20..

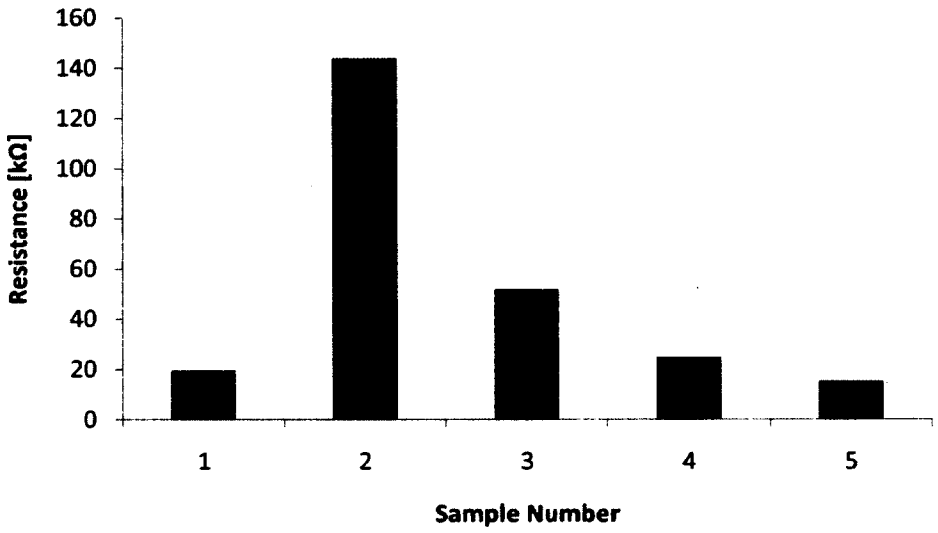

Figure 5- 18: Resistance measured across length of the 20wt% pillars.

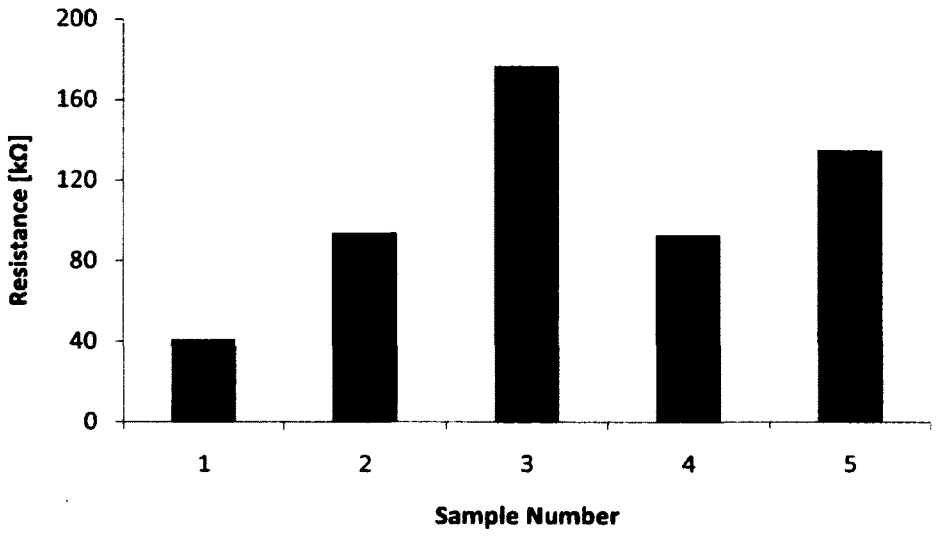

Figure 5- 19: Resistance measured across the printed face of the 20wt% pillars.

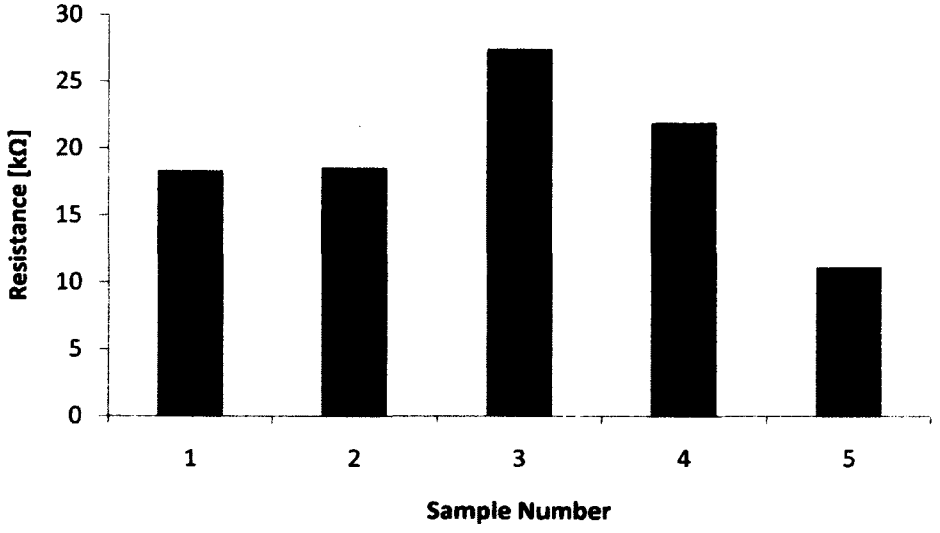

Figure 5- 20: Resistance measured across the perpendicular printed face of the 20wt% pillars.

With the increase in graphene and different orientation of printing, the resistance characteristics for the 20wt% changed drastically for the pillars. While the majority of the data shows that the highest resistance was found for the measurements taken across

the print face (Figure 5-19) and the lowest resistance found for the perpendicular face (Figure 5-20), very low resistances were found for the length of the pillar and outlying data was found for sample 2. These lowered resistances are again due to tighter bonding between adjoining filament per layer as opposed to filament laid in different layers. The outlying data for sample 2 is attributed to internal print defects. Visual inspection and parameter measurement shows no variation between the other samples, however errors during printing internal to the construct (layer defects, etc.) could explain this jump in resistance.

5.5.4.1.3 Capacitance Testing

Capacitance testing was also performed on the pillar samples across multiple faces to see if any capacitance was found between the printed layers. A 5 V AC power source was used at 60 Hz. Capacitance was tested among multiple faces as described in the previous section. In measuring the capacitances, the 15wt% did not exhibit any capacitance in the body of the printed constructs, most likely due to the low conductivity of the filament used for printing along with inherent print defects that did not lead to fully encapsulated voids around which charge differentials could be stored. This in turn did not lead to any building of charge between any inherent voids in the material. The 20wt% exhibited measurable capacitances that varied depending upon the face that was measured. These measurements were performed on both the vertically and horizontally printed squares. The capacitances found for the vertically printed are shown in Figures 5-21 and 5-22.

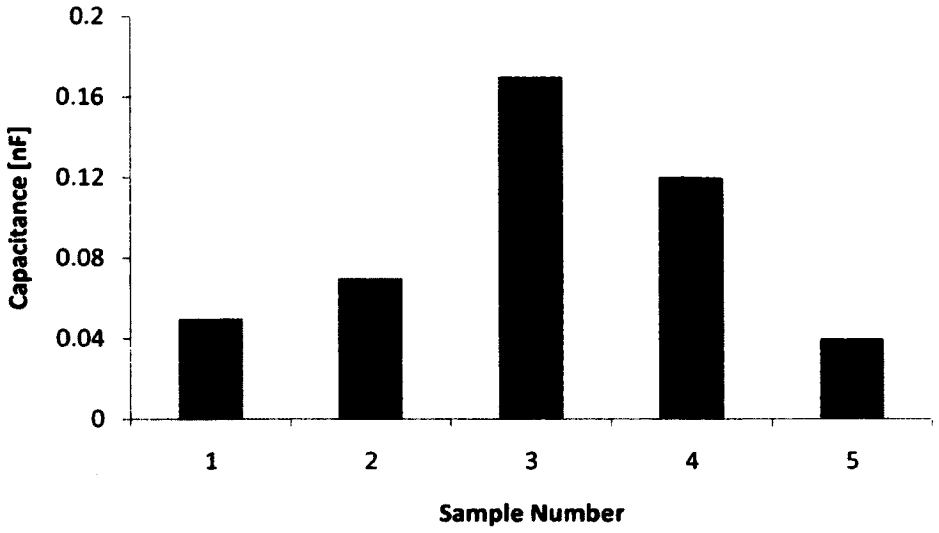

Figure 5- 21: Capacitance measured for vertical print along length of pillar.

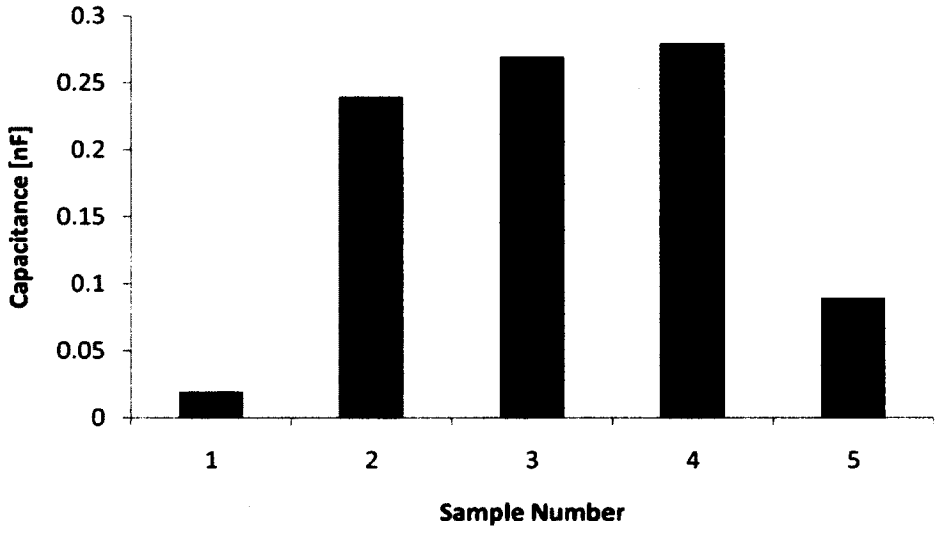

Figure 5- 22: Capacitance measured for vertical print along middle of pillar.

Significantly higher capacitances were found for the shorter faces measured as would be expected for the shorter distance. Another cause of this is most likely due to the larger amount of stacked filaments in the perpendicular direction to that of the printed

planes wherein charge may accumulate along the voids found in adjoining filament strands. These measurements were also taken for the horizontally printed pillars and this data is shown in Figures 5-23, 5-24, and 5-25.

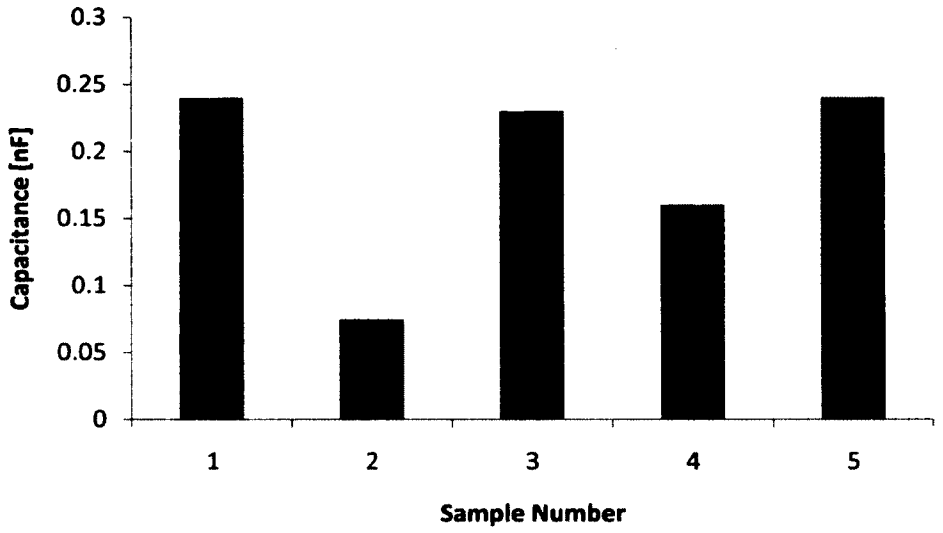

Figure 5- 23: Capacitance measured across length of the 20wt% pillars.

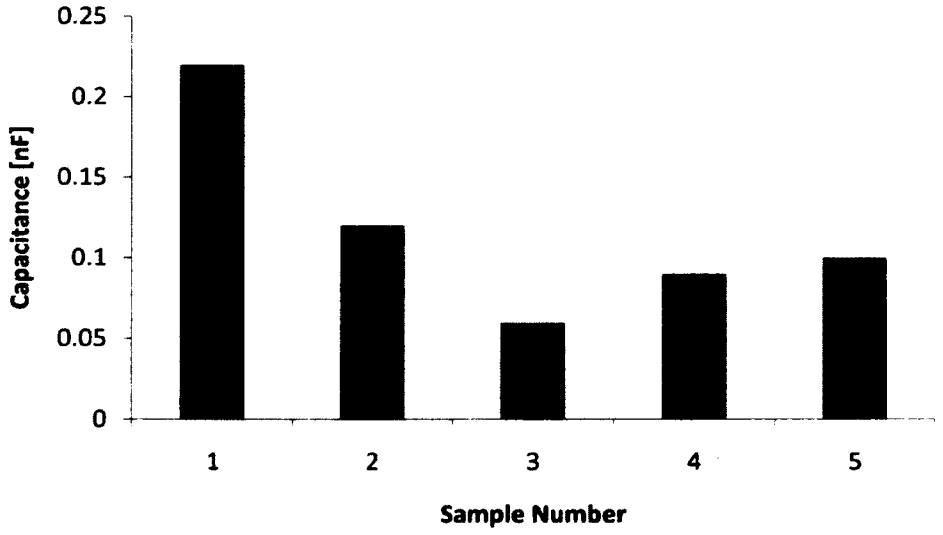

Figure 5- 24: Capacitance measured across the printed face of the 20wt% pillars

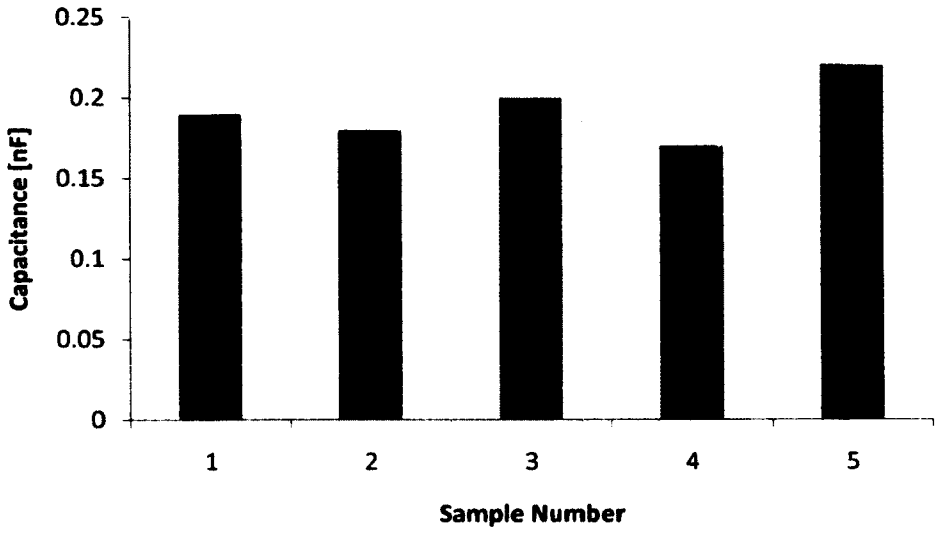

Figure 5- 25: Capacitance measured across the perpendicular printed face of the 20wt% pillars.

Here again the smallest capacitance is found for the measurements taken along the printed planes with the measurements taken in areas perpendicular to the print direction showing markedly higher measured capacitances. For this sample batch, the majority of measurements taken along the length of the pillar rather than the shorter perpendicular side showed higher capacitances. This is correlated with the lower resistances found previously for this sample batch. Further, the higher resistances measure for this batch of samples is directly correlated to the found capacitances: where there is a peak in resistance there is trough in capacitance due to the lack of conductivity between adjoining layers, leading to minimal charge buildup. Where lower resistances are found, charge accumulation is also found leading to the higher capacitance measurements between the adjoining layers perpendicular to the printed layers.

5.5.4.2 *3D Printed Piezoresistivity Bridges*

The piezoresistivity bridges were printed for the 20wt% filaments at varying thicknesses ranging from 0.2-1 mm. These thicknesses are based off of the layer height for the 3D printer where 0.2 mm corresponds to one layer of printed material. Bridges could not be printed for the 15wt% due to the poor quality of the filament. The filament tended to curl, reattaching itself to the print head, leading to inhibited printability. The columns printed better due to the small x- and y-direction movements during the print, leading to better attachment of the filament to the printing platform. The printed constructs are shown in Figure 5-26 for the 20wt% with increasing thicknesses from left to right. The limitations of the 3D printer can readily be seen for those constructs that have very few layers. As the thickness increases, these are overcome through the successive layers.

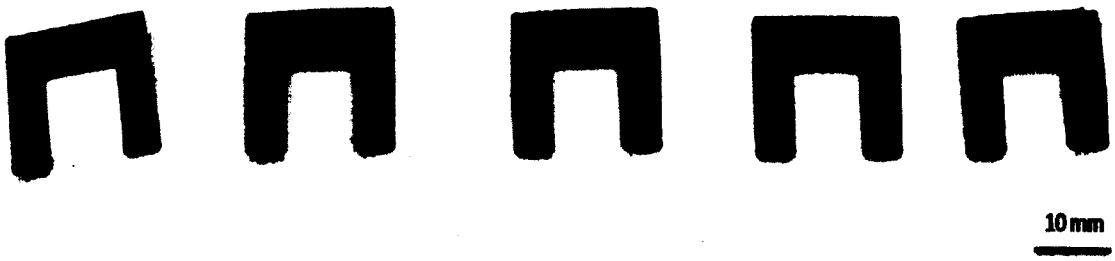

Figure 5-26: 3D printed piezoresistivity bridges for 20 wt% graphene doped PMMA filament.

Baseline measurements were taken prior to deformation to get a measurement with which to compare against. Once baseline measurements were taken, each bridge was flexed to a 90 degree angle to ensure significant flexing. Measurements were then taken by multimeter using the two extended portions from the construct. All flexing

occurred at the middle of the bridging portion between the two extension for each construct to ensure all constructs had the same curvature at the same point along the body for comparison. After flexing, measurements were then taken on the relaxed construct to see whether permanent altering of the resistance occurred. Shown in Figure 5-27 are the piezoresistance measurements taken for these constructs.

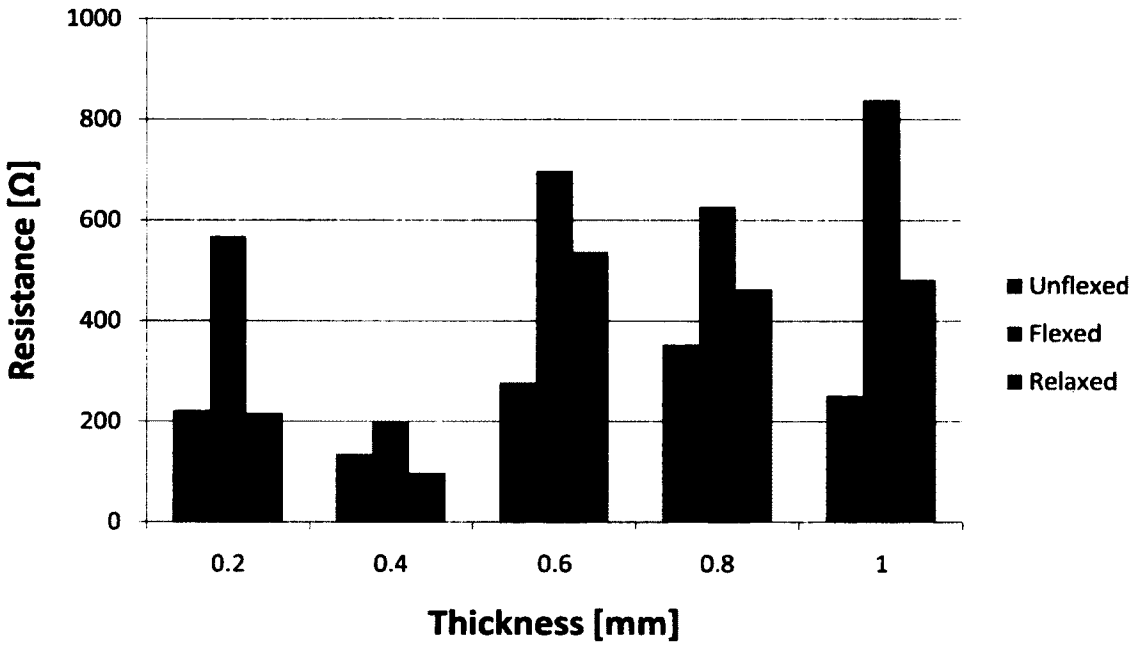

Figure 5-27: Resistances for unflexed, flexed, and relaxed resistances for printed bridges.

Flexing of the constructs showed significant increases in resistance for all structures, then relaxation resistance proved to be dependent on the thickness of the object. For thinner objects (0.2-0.4 mm), a decrease in resistance was found and attributed to the flexible nature of the thinner print. For greater thicknesses (>0.4 mm) a permanent increase in resistance for the relaxed over the unflexed constructs was found. The increase in resistance from flexing is attributed to separation of the printed layers, leading to lesser contact for the conductive network. Upon relaxation, these layers are no

longer tightly bonded from the printing process, resulting in a permanent increase in resistance.

5.5.5 Conductive Bone Cement

Due to the ease with which the PMMA and graphene powder was mixed, it was desired to see the effect of the graphene dopant on the fabrication of commercial bone cements that use a mixture of PMMA powder and MMA monomer to polymerize the PMMA powder into a desired object. This has found wide use in the medical field as these constructs are not biodegradable, thus they can be used for reinforcement or delivering loaded chemicals to targeted areas. Fabrication of conductive bone cements is a first step in developing embedded sensor platforms into this material for potential real time monitoring of the implant in situ for the patient.

5.5.5.1 *Resistance Measurements*

Resistance measurements were taken for both the pillars and the dog bones. A multimeter was used, and resistance measurements taken across the length of the pillars and at the pads for the dog bone. Four samples were used for each pillar set and three samples used for each dog bone set to ensure statistical analysis could be performed on each group of samples.

5.5.5.1.1 Pillar Resistance Measurements

All cylindrical pillars were fabricated with 6 mm diameters and 12 mm lengths, the ASTM standard for strength testing of bone cements. Shown in Table 5-1 are the results for each pillar set fabricated at varied weight percentages of 5-25wt%.

Table 5- 1: Graphene doped bone cement pillar resistance measurements (kΩ) for 5-25wt%.

5wt%	10wt%	15wt%	20wt%	25wt%
320	421	300	2.4	1.1
305	620	135	2.6	0.49
475	525	184	1.2	0.95
1,100	255	224	2.7	0.96

The resistances measured had relatively high variances. This is primarily due to difficulty in the dispersion of the graphene throughout the PMMA/MMA mixture once the MMA is introduced. The graphene tended to clump, and as the MMA monomer added is in such a low quantity, overcoming this clumping is difficult. Once the bone cement has set, the resistance measurements have very little fluxuation, showing that the conductive networks within the cast bone cement are rigidly set. This leads to the conclusion that once cured, the bone cements will have a reliable resistance that can be accounted for in sensor development should no load be applied.

5.5.5.2 *Piezoresistivity Measurements*

For the piezoresistivity measurements, all dog bones were subjected to a 20 degree curvature to test how the resistance was affected from the flexing. Resistance measurements were taken prior to the flexing of the dog bones to provide a baseline measurement. Next, the dog bones were placed in a caliper with electrical tape over the measuring arms to ensure the measurements taken were for the body of the bone cement. The dog bones were then slowly bent to the desired angle of deformation and a reading taken via multimeter. As stated previously, the 5wt%, 10wt%, and 25wt% were rigid structures while the 15wt% and 20wt% were more flexible. This lead to some dog bones breaking during the flexural testing. After data was taken during flexing, the dog bones

were removed from the caliper and measurements were taken to see whether a permanent change in the resistance occurred. Shown in Figures 5-28 and 5-29 are the results for the varying doping levels before, during and after the flexural testing.

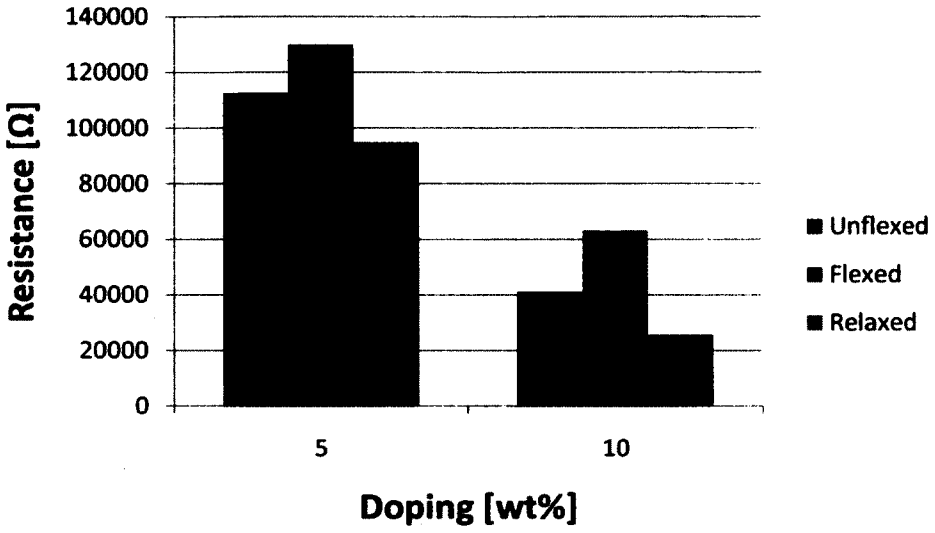

Figure 5-28: Unflexed, flexed, and relaxed resistances for 5-10wt% bone cement dog bones.

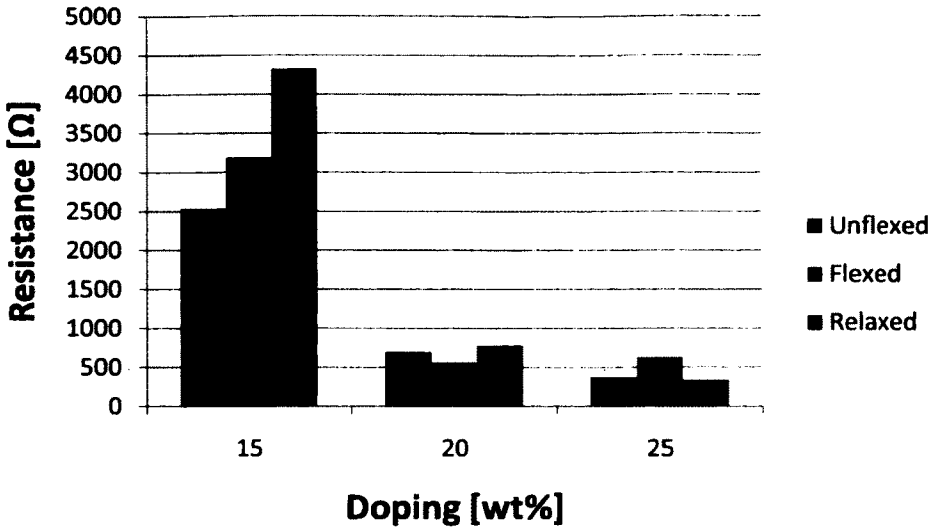

Figure 5-29: Unflexed, flexed, and relaxed resistances for 15-25wt% bone cement dog bones.

While the data above shows little correlation, it must be kept in mind when examining it the nature of the dog bones and the problems with even dispersion throughout the sample batch. For the 5wt%, 10wt%, and 25wt%, the more structurally sound and fuller polymerized samples, flexing of the sample led to an increase in resistance. This is due to the separation of conductive networks within the bone cement during the flexing. Once relaxed, nearly all of these samples showed lower resistances than prior to flexing. This would be due to greater contact amongst the conductive networks within the bone cements, leading to better conduction throughout the bulk sample.

For the 15wt% and 20 wt%, the more flexible samples, an increase in resistance was observed during flexing, again attributed to the separation of the conductive networks. Once relaxed, all dog bones from these two sample groups experienced higher resistances. This is most likely due to unreacted MMA monomer within the sample

leaking out of the bulk and covering the conduction sites for the bone cements, leading to less conductive networks overall for the bulk sample.

5.6 Summary

A method of manufacturing graphene doped 3D printing filament was achieved through the use of PMMA powder. This method proved to be viable for doping percentages ranging from 0-20wt% graphene. Beyond this, filament viability was inhibited. Only filaments of doping percentages 15-20wt% proved to be conductive. Both proved to print, however resolution was poor for the 15wt% filament, most likely attributed to difficulty in cooling for the material.

Electrical characterization was performed for printed constructs to measure the resistance, capacitance, and piezoresistivity of the constructs. It was found that the 15wt% printed constructs had very high associated resistances as compared to the 20wt%, however no measurable capacitance was found. This was attributed to the lack of conductivity of the printed filament that did not lead to charge buildup within the material. The 20wt% printed constructs proved to have much better measure resistances, especially along the faces perpendicular to the print direction. This is attributed to the cohesive conductive networks found per printed layer. Higher measurable capacitances were found for these perpendicular faces over the faces parallel to the print direction. This was attributed to the higher resistance building up charge in the inherent voids formed in the print process. Further, for the outlying samples that showed to have much higher resistances due to internal printing defects, the associated capacitance for that measurement was at a minimum. Piezoresistivity for printed constructs was also measured using 3D printed bridges ranging in thickness from 0.2-1 mm in steps of 0.2

mm (the resolution of the 3D printers z-axis). The 15wt% filament proved to be ineffective in printing larger constructs than the pillars previously described due to adhesion problems with the filament. The 20wt% proved to effectively print the constructs, and showed piezoresistive responses for flexing of the constructs. The flexed constructs showed an increase in resistance over the unflexed constructs, and a permanent increase in resistance was found after flexing. This is attributed to the separation of printed layers, wherein the layers touch but are no longer tightly bound as they were post-printing pre-flexing.

As to the bone cements, a method for making and characterizing the resistance of these structures was demonstrated. Further, testing was performed to see how flexural load bearing affects the resistance of bulk samples. It was found that even dispersion of the graphene powder throughout the cast samples was hard to achieve. When a force was applied, every sample testing experienced an increase in resistance. For the samples that experienced a more full polymerization, and were therefore more rigid bodies, the sample then exhibited less resistance throughout the bulk material after being relaxed from flexing. For those samples that were not fully polymerized, increases in resistance were found for both flexing and permanent increases in resistance found after relaxation. This is attributed to unreacted MMA monomer leaking from the bulk and covering the contact sites, leading to less available conductive networks overall.

CHAPTER 6

CONCLUSIONS AND FUTURE WORK

6.1 Conclusions

It is clear that additive manufacturing, though still in its infancy, has wide applicability to a number of areas of manufacturing. The ability to 3D print constructs doped with a desired additive without requiring industrial scale fabrication equipment is very promising to the versatility of this manufacturing method, however inherent errors in the printing process dictate careful characterization of the printed object. Combining this with nanotechnology can lead to new and improved systems using mixtures of the various compounds to enhance desired attributes. Further, the ability to use halloysite nanotubes in a modular fashion similar to 3D printing may lead to unique and yet undiscovered results. Overall, three core conclusions can be made from the projects and objects presented in this work.

A modular method of coating halloysite nanotubes via dry sintering was discovered that shows promising use for sensors or customized medical treatment platforms or experimental works. This method is important to show that significant amounts of material can be placed on the exterior of these tubes in a low cost manner that does not require the use of wet chemical processes. Imaging and EDAX confirmed retention of the additives in singular and mixed coatings for iron, barium, copper, nickel, lithium, and gold. Further, it was found that where a metal acetylacetonate was not

commercially available, a metal acetate could be used in its place with only minor adjustments to the fabrication process. Magnetic response was characterized for the iron coated nanotubes, and showed successively higher magnetization for increased amounts of deposited iron. A saturation of iron uptake around 2.5 parts iron acetylacetonate to 1 part halloysite. Opacity testing was done of the barium coated halloysite and showed large increases in opacity over undoped commercial bone cement. Finally, laser testing was done for the raw, iron coated, gold coated, and iron/gold coated halloysites. This showed that the gold nanoparticles deposited onto the exterior of the halloysite had increased resonant responses over the other coatings. For a mixed coating such as the iron/gold, greater amounts of gold need to be deposited to maintain a resonant response.

A method of dispersing powdered additives into PLA filament was developed and characterized for iron oxide, barium sulfate, and gadolinium oxide. This method proved viable using commercially available filament extrusion and 3D printing equipment without modification, and proved viable for doping percentages up to 25wt%. Radiation testing of the iron oxide showed retention of the iron through the extrusion process by successive blocking of a beta source signal. Barium sulfate retention was proven via medical X-ray that showed an increase in opacity was obtained for successively larger amounts of barium sulfate.

A method of fabricated conductive 3D printing filament was developed using PMMA and graphene powders. This method proved viable on commercially available equipment without modification. Conductivity was only obtained for 15wt% and 20wt%; percentages below this were insulating in nature, and 25wt% filament showed problems during the filament extrusion process. These filaments were used on a commercially

available printer, and while both showed to be printable, significantly higher resolutions were obtained for the 20wt% over the 15wt%. Electrical characterization was done for printed constructs to investigate associated resistances, junction capacitances, and piezoresistive response. Resistances were found to vary depending upon the print quality of the construct and the orientation of printed layers relative to the measuring point. Junction capacitances were found on the order of 20 pF for the 20wt% constructs, an important design consideration when considering the use of these constructs in electrical circuits. A piezoresistive response was found for the printed structures where a higher resistance was obtained during flexing. Post flexing a permanent increase in resistance was found, and this is attributed to the separation of the printed layers. Conductive PMMA/MMA bone cements were also fabricated at varied weight percentages, and were found to be conductive for 5-25wt%. Mechanical properties were inhibited for 15-25wt% for these structures, attributed to incomplete polymerization of the PMMA/MMA mixture. Set resistances were found for these structures. When flexed, a piezoresistive response was found that showed an increase in resistance during flexing with a permanent increase in resistance after relaxation. This is attributed to unreacted MMA leaking into microfractures, inhibiting the conductive networks within the structure.

6.2 Future Work

This work can be best described as proof of principle, especially as pertains to the 3D printing. While a viable method of dispersing additives was developed, better dispersion and higher weight percentages can almost certainly be achieved through the use of proprietary or modified equipment. Further, characterization of the gadolinium oxide as a thermal neutron regulator should be performed to complete the multistack

design for a printed shielding construct. All aspects of the fabrication process could be optimized and improved, however this will most assuredly require modification of both the filament extrusion equipment and the 3D printing equipment. Through these modifications, careful consideration for resolution and material response must be considered such that neither is compromised during the modification.

REFERENCES

[1] ASTM, "Standard Terminology for Additive Manufacturing Technologies," in *F2792* vol. F2792-12a, ed. Book of Standards Volume 10.04, 2013.

[2] K. K. Jain, *The Handbook of Nanomedicine*, 2nd ed.: Springer, 2012.

[3] N. G. Veerabadran, R. Price, and Y. M. Lvov, "Clay nanotubes for encapsulation and sustained release of drugs," *Nano,* vol. 2, pp. 115-120, 2007.

[4] J. Smith, "How It Is Made: 3D Printing Filament," C. Kraft, Ed., ed. Make Magazine, 2015.

[5] (2012, February 24). *NAE Grand Challenges for Engineering* [Web Site]. Available: http://www.engineering.uiowa.edu/14-grand-challenges

[6] E. P. Agency. (2011, February 24). *Low-Level Radioactive Waste*. Available: http://www.epa.gov

[7] B. Berman, "3-D printing: The new industrial revolution," *Business horizons,* vol. 55, pp. 155-162, 2012.

[8] (2015, March 31). *This drivable car was 3D printed in 44 hours* [Article]. Available: http://www.businessinsider.com/car-3d-printing-local-motors-strati-2015-2

[9] S. P. Hunger, X. Lu, M. Devidas, B. M. Camitta, P. S. Gaynon, and N. J. Winick, "Improved survival for children and adolescents with acute lymphoblastic leukemia between 1990 and 2005: a report from the children's oncology group," *Journal of Clinical Oncology,,* vol. 37, p. 8018, 2012.

[10] (2014, February 24). *PacTec*. Available: http://www.pactecinc.com/

[11] D. Li, K. Xie, R. Wolff, and J. L. Abbruzzese, "Pancreatic cancer," *The Lancet,* vol. 363, pp. 1049-1057, 2004.

[12] E. S. Darley and A. P. MacGowan, "Antibiotic treatment of gram-positive bone and joint infections," *Journal of Antimicrobial Chemotherapy,* vol. 53, pp. 928-935, 2004.

[13] (2015, February 24). *EPA Response to 2014 Radioactive Release at the Waste Isolation Pilot Plant (WIPP)*. Available: http://www.epa.gov/radiation/wipp/index.html

[14] H. O. Pierson, *Handbook of Chemical Vapor Deposition: Principles, Technology, and Applications*, 2 ed. Norwich, New York: William Andrew Publishing, LLC, 1999.

[15] C. F. Powell, "Chemical Vapor Deposition," in *Vapor Deposition*, ed New York: John Wiley & Sons, 1966, pp. 249-276.

[16] F. G. Celii and J. E. Butler, "Diamond Chemical Vapor Deposition," *Annual Review of Physical Chemicstry,* vol. 42, pp. 643-684, 1991.

[17] M. Kumar and Y. Ando, "Chemical Vapor Deposition of Carbon Nanotubes: A Review on Growth Mechanism and Mass Production," *Journal of Nanoscience and Nanotechnology,* vol. 10, pp. 3739-3758, 2010.

[18] S. Huang, M. Woodson, R. Smalley, and J. Liu, "Growth Mechanism of Oriented Long Single Walled Carbon Nanotubes Using "Fast-Heating" Chemical Vapor Deposition Process," *Nano Letters,* vol. 4, pp. 1025-1028, 2004.

[19] A. Reina and X. Jia, "Large Area, Few-Layer Graphene Films on Arbitrary Substrates by Chemical Vapor Deposition," *Nano Letters,* vol. 9, pp. 30-35, 2009.

[20] D. Wei, Y. Liu, Y. Wang, H. Zhang, L. Huang, and G. Yu, "Synthesis of N-Doped Graphene by Chemical Vapor Deposition and Its Electrical Properties," *Nano Letters,* vol. 9, pp. 1752-1758, 2009.

[21] Y. Zhang, L. Zhang, and C. Zhou, "Review of Chemical Vapor Deposition of Graphene and Related Applications," *Accounts of Chemical Research,* vol. 46, pp. 2329-2339, 2013.

[22] H. Liu, L. Feng, J. Zhai, L. Jiang, and D. Zhu, "Reversible Wettability of a Chemical Vapor Deposition Prepared ZnO Film between Superhydrophobicity and Superhydrophilicity," *Langmuir,* vol. 30, pp. 5659-5661, 2004.

[23] B. Xiang, P. Wang, and e. al., "Rational Synthesis of p-Type Zinc Oxide Nanowire Arrays Using Simple Chemical Vapor Deposition," *Nano Letters,* vol. 7, pp. 323-328, 2006.

[24] G. Decher, "Fuzzy Nanoassemblies: Toward Layered Polymeric Multicomposites," *Science,* vol. 277, pp. 1232-1237, 1997.

[25] S. W. Keller, H. Kin, and T. E. Mallouk, "Layer-by-Layer Assembly of Intercalation Compounds and Heterostructures on Surfaces: Toward Molecular "Beaker" Epitaxy," *Journal of the American Chemical Society,* vol. 116, pp. 8817-8818, 1994.

[26] Y. M. Lvov, "Thin Film Nanofabrication by Alternate Adsorption of Polyions, Nanopartices, and Proteins," 2011.

[27] R. K. Iler, "Multilayers of colloidal particles," *Journal of Colloidal Interface Science,* vol. 21, pp. 569-594, 1966.

[28] G. D. a. J. D. Hong, "Buildup of ultrathin multilayer films by a self-assembly process: I. consecutive adsorption of anionic and cationic bipolar amphiphiles," *Macromolecular Symposia,* vol. 46, pp. 321-327, 1991.

[29] G. Decher and J. D. Hong, "Buildup of ultrathin multilayer films by a self-assembly process: II. Consecutive adsorption of anionic and cationic bipolar amphiphiles and polyelectrolytes on charged surfaces," *Journal of Physical Chemistry,* vol. 95, pp. 1430-1434, 1991.

[30] G. Decher, J. D. Hong, and J. Schmitt, "Buildup of ultrathin multilayer films by a self-assembly process: III. Consecutively alternating adsorption of anionic and cationic polyelectrolytes on charged surfaces," *Thin Solid Films,* vol. 210/211, pp. 831-835, 1992.

[31] D. Hong, K. Lowack, J. Schmitt, and G. Decher, "Layer-by-layer deposited multilayer assemblies of polyelectrolytes and proteins: from ultrathin films to protein arrays," *CProgress in Colloid Polymer Science,* vol. 93, pp. 92-102, 1993.

[32] M. S. Sheu and I. H. Lou, "Biomedical articles with ionically bonded polyelectrolyte coatings," U. S. Patent U.S Patent 5,837,377, 1998.

[33] M. F. A. Goosen, G. M. O'Shea, and A. M. Sun, "Microencapsulation of living tissue and cells," US Patent, 1987.

[34] K. Marton, *Vacuum Physics and Technology*: Academic Press, 1980.

[35] R. C. Jaeger, "Film Deposition," in *Introduction to Microelectronic Fabrication*, 2 ed: Prentice Hall, 2002.

[36] S. M. Sze, *Semiconductor Devices: Physics and Technology*, 3 ed.: Wiley, 2012.

[37] Z. R. Dai, Z. W. Pan, and Z. L. Wang, "Novel Nanostructures of Functional Oxides Synthesized by Thermal Evaporation," *Advanced Functional Materials,* vol. 13, pp. 9-24, 2003.

[38] B. D. Yao, Y. F. Chan, and N. Wang, "Formation of ZnO nanostructures by a simple way of thermal evaporation," *Applied Physics Letters,* vol. 81, p. 757, 2002.

[39] C. Cantalini, W. Wlodarski, Y. Li, M. Passacantando, S. Santucci, E. Comini, *et al.*, "Investigation on the O3 sensitivity properties of WO3 thin films prepared by sol–gel, thermal evaporation and r.f. sputtering techniques," *Sensors and Actuators B: Chemical,* vol. 64, pp. 182-188, 2000.

[40] G. Shen, Y. Bando, and C. J. Lee, "Synthesis and Evolution of Novel Hollow ZnO Urchins by a Simple Thermal Evaporation Process," *Journal of Physical Chemistry, B,* vol. 109, pp. 10578-10583, 2005.

[41] S. H. Sun, G. W. Meng, G. X. Zhang, T. Gao, B. Y. Geng, L. D. Zhang, *et al.*, "Raman scattering study of rutile SnO2 nanobelts synthesized by thermal evaporation of Sn powders," *Chemical Physics Letters,* vol. 376, pp. 103-107, 2003.

[42] Z. W. Pan, Z. R. Dai, and Z. L. Wang, "Nanobelts of Semiconducting Oxides," *Science,* vol. 291, pp. 1947-1949, 2001.

[43] H. H. Anderson, H. L. Bay, R. Behrisch, M. T. Robinson, H. E. Roosendaal, and P. Sigmund, *Sputering by Particle Bombardment I: Physical Sputtering of Single-Element Solids*. New York: Springer, 1981.

[44] P. J. Kelly and R. D. Arnell, "Magnetron sputtering: a review of recent developments and applications," *Vacuum,* vol. 56, pp. 159-172, 1999.

[45] P. F. Carcia, R. S. McLean, M. H. Reilly, and G. N. Jr., "Transparent ZnO thin-film transistor fabricated by rf magnetron sputtering," *Applied Physics Letters,* vol. 82, p. 1117, 2003.

[46] S. Facsko, T. Dekorsy, C. Koerdt, C. Trappe, H. Kurz, A. Vogt, *et al.*, "Formation of Ordered Nanoscale Semiconductor Dots by Ion Sputtering," *Science,* vol. 285, pp. 1551-1553, 1999.

[47] T. Minami, H. Sato, H. Nanto, and S. Takata, "Group III Impurity Doped Zinc Oxide Thin Films Prepared by RF Magnetron Sputtering," *Journal of Applied Physics,* vol. 24, p. 781, 1985.

[48] N. Laegreid and G. K. Wehner, "Sputtering Yields of Metals for Ar+ and Ne+ Ions with Energies from 50 to 600 ev," *Journal of Applied Physics,* vol. 32, p. 365, 1961.

[49] S. Bordeepong, D. Bhongsuwan, T. Pungrassami, and T. Bhongsuwan, "Characterization of halloysite from Thung Yai District, Nakhon Si Thammarat Province, in Southern Thailand," *Sonklanakarin Journal of Science and Technology,* vol. 33, pp. 599-607, 2011.

[50] G. Nitya, G. T. Nair, U. Mony, K. P. Chennazhi, and S. V. Nair, "In vitro evaluation of electrospun PCL/nanoclay composite scaffold for bone tissue engineering," *Journal of Materials Science: Materials in Medicine,* vol. 23, pp. 1749-1761, 2012.

[51] W. O. Yah, A. Takahara, and Y. M. Lvov, "Selective modification of halloysite lumen with octadecylphosphonic acid: new inorganic tubular micelle," *Journal of the American Chemical Society,* vol. 134, pp. 1853-1859, 2012.

[52] E. Joussein, S. Petit, J. Churchman, B. Theng, D. Righi, and B. Delvaux, "Halloysite clay minerals - a review " *Clay Minerals,* vol. 40, pp. 383-426, 2005.

[53] L. T. Alexander, G. T. Faust, S. B. Hendricks, H. Insley, and H. F. McMurdie, "Relationship of the clay minerals halloysite and endellite," *American Mineral,* vol. 28, pp. 1-18, 1943.

[54] G. J. Churchman and B. K. G. Theng, "Interactions of halloysites with amides: mineralogical factors affecting complex formation," *Clay Minerals,* vol. 19, pp. 161-175, 1983.

[55] H. M. Kelly, P. B. Deasy, E. Ziaka, and N. Claffey, "Formulation and preliminary in vivo dog studies of a novel drug delivery system for the treatment of periodontitis," *International Journal of Pharmaceutics,* vol. 274, pp. 167-183, 2004.

[56] R. R. Price, B. P. Gaber, and Y. Lvov, "In-vitro release characteristics of tetracycline HCl, khellin and nicotinamide adenine dineculeotid from ahlloysite; a cylindrical mineral," *Journal of Microencapsulation,* vol. 18, pp. 713-722, 2000.

[57] V. Amendola and M. Meneghetti, "Self-healing at the nanoscale," *Nanoscale,* vol. 74, pp. 74-88, 2009.

[58] E. Abdullayev, V. Abbasov, A. Tursunbayeva, V. Portnov, H. Ibrahimov, G. Mukhtarova, *et al.*, "Self-Healing Coatings Based on Halloysite Clay Polymer Composites for Protection of Copper Alloys," *ACS Applied Materials and Interfaces,* vol. 5, pp. 4464-4471, 2013.

[59] K. Hedicke-Höchstötter, G. T. Lim, and V. Altstädt, "Novel polyamide nanocomposites based on silicate nanotubes of the mineral halloysite," *Composites Science and Technology,* vol. 69, pp. 330-334, 2009.

[60] K. Prashantha, H. Shmitt, M. F. Lacrampe, and P. Krawczak, "Mechanical behaviour and essential work of fracture of halloysite nanotubes filled polyamide 6 nanocomposites," *Composites Science and Technology,* vol. 71, pp. 1859-1866, 2011.

[61] N. Ning, Q. Yin, F. Luo, Q. Zhang, R. Du, and Q. Fu, "Crystallization behavior and mechanical properties of polypropylene/halloysite composites," *Polymer,* vol. 48, pp. 109-118, 2007.

[62] H. Imsail, "The Effect of Halloysite Nanotubes as a Novel Nanofiller on Curing Behaviour, Mechanical and Microstructural Properties of Ethylene Propylene Diene Monomore (EPDM) Nanocomposites," *Polymer-Plastics Technology and Engineering,* vol. 48, pp. 313-323, 2009.

[63] C. Liu, "Enhancement of mechanical properties of poly(vinyl chloride) with polymethyl methacrylate-grafted halloysite nanotube," *eXPRESS Polymer Letters,* vol. 5, pp. 591-603, 2011.

[64] B. Guo, "Tubular Clay Composites with High Strength and Transparency," *Journal of Macromolecular Science, Part B: Physics,* vol. 49, pp. 111-121, 2010.

[65] D. G. Shchukin and H. Mohwald, "Surface-engineered nanocontainers for entrapment of corrosion inhibitors," *Advanced Functional Materials,* vol. 17, pp. 1451-1458, 2007.

[66] S. Chen, J. Li, Y. Zhang, D. Zhang, and J. Zhu, "Effect of preparation method on halloysite supported cobalt catalysts for Fischer-Tropsch synthesis," *Journal of Natural Gas Chemistry,* vol. 21, pp. 426-430, 2012.

[67] X. Tang, L. Li, B. Shen, and C. Wang, "Halloysite-nanotubes supported FeNi alloy nanoparticles for catalytic decomposition of toxic phosphine gas into yellow phosphorus and hydrogen," *Chemosphere,* 2013.

[68] Z. Jia, "Morphology, Interfacial Interaction and Properties of Styrene-Butadiene Rubber/modified Halloysite Nanotube Nanocomposites," *Chineses Journal of Polymer Science,* vol. 27, pp. 857-864, 2009.

[69] Y. Zhao and e. al., "Ammonium removal from aqueous solution by zeolite x synthesized from halloysite mineral," *Water Science & Technology,* pp. 937-946, 2010.

[70] B. Guo and e. al., "Adsorption of Ionic Liquid onto Halloysite Nanotubes: Mechanism and Reinforcement of the Modified Clay to Rubber," *Journal of Macromolecular Science, Part B: Physics,* vol. 49, pp. 1029-1043, 2010.

[71] Y. Zhao and e. al., "Removal of Ammonium from Wastewater by Pure Form Low-Silica Zeolite Y Synthesized from Halloysite Mineral," *Separation Science and Technology,* vol. 45, pp. 1029-1043, 2010.

[72] J. V. Hoene, R. G. Charles, and W. M. Hickam, "Thermal decomposition of metal acetylacetonates: mass spectrometer studies," *The Journal of Physical Chemistry,* vol. 62, pp. 1098-1101, 1958.

[73] A. J. V. Hengstum, J. G. V. Ommen, H. Bosch, and P. J. Gellings, "Preparation of supported vanadium and molybdenum oxide catalysts using metal acetylacetonate complexes," *Applied Catalysis,* vol. 5, pp. 207-217, 1983.

[74] C. A. Wilkie and D. T. Harworth, "A 13C NMR study of some metal acetylacetone complexes," *Journal of Inorganic and Nuclear Chemistry,* vol. 40, pp. 195-197, 1978.

[75] M. Niederber, G. Garnweigner, N. Pinna, and G. Neri, "Non-aqueous routes to crystalline metal oxide nanoparticles: Formation mechanisms and applications," *Progress in Solid State Chemistry,* vol. 33, pp. 59-70, 2005.

[76] M. Niederberger, G. Garnweigner, J. Buha, J. Polleux, J. Ba, and N. Pinna, "Nonaqueous synthesis of metal oxide nanoparticles: Review and indium oxide as case study for the dependence of particle morphology on precursors and solvents," *Journal of Sol-Gel Science and Technology,* vol. 40, pp. 259-266, 2006.

[77] Y. Shimizu and T. Murata, "Sol-Gel Synthesis of Perovskite-Type Lanthanum Manganite Thin Films and Fine Powders Using Metal Acetylacetonate and Poly(vinyl alcohol)," *Journal of the American Ceramic Society,* vol. 80, pp. 2702-2704, 1997.

[78] J. A. Happe and R. L. Ward, "Isotropic NMR Shifts in Pyridine-Type Bases Complexed with Paramagnetic NiII and CoII Acetylacetonates," *The Journal of Chemical* vol. 39, pp. 1211-1218, 1963.

[79] S. D. Bakrania, G. K. Rathore, and M. S. Wooldridge, "An Investigation of the Therma Decomposition of Gold Acetate," *Journal of Thermal Analysis and Calorimetry,* vol. 95, pp. 117-122, 2009.

[80] C. K. Chua, K. F. Leong, and C. S. Lim, *Rapid prototyping: principles and applications*: World Scientific, 2010.

[81] C. C. Kai, C. S. Meng, L. S. Ching, E. K. Hoe, and L. K. Fah, "Rapid prototyping assisted surgery planning," *The International Journal of Advanced Manufacturing Technology,* vol. 14, pp. 624-630, 1998.

[82] J. P. Kruth, "Material incress manufacturing by rapid prototyping techniques," *CIRP Annals-Manufacturing Technology,* vol. 40, pp. 603-614, 1991.

[83] J. Flowers and M. Moniz, "Rapid prototyping in technology education," *Technology Teacher,* vol. 62, pp. 7-25, 2002.

[84] S. Morvan, R. Hochsmann, and A. Carraro, "Rapid Manufacturing finally delivers: the Prometal RCT process, for the fabrication of complex sand molds and sand cores," presented at the RPD Conference, 2004.

[85] V. K. Balla, S. Bose, and A. Bandyopadhyay, "Processing of bulk alumina ceramics using laser engineered net shaping," *International Journal of Applied Ceramic Technology,* vol. 5, pp. 234-242, 2008.

[86] G. V. Salmoria, R. A. Paggi, A. Lago, and V. E. Beal, "Microstructural and mechanical characterization of PA12/MWCNTs nanocomposite manufactured by selective laser sintering," *Polymer Testing,* vol. 30, pp. 611-615, 2011.

[87] H. H. Tang, M. L. Chiu, and H. C. Yen, "Slurry-based selective laser sintering of polymer-coated ceramic powders to fabricate high strength alumina parts," *Journal of the European Ceramic Society,* vol. 31, pp. 1383-1388, 2011.

[88] J. W. Halloran, V. Tomeckova, S. Gentry, S. Das, P. Cilino, D. Yuan, *et al.*, "Photopolymerization of powder suspensions for shaping ceramics," *Journal of the European Ceramic Society,* vol. 31, pp. 2613-2619, 2011.

[89] Y. Liao, H. Li, and Y. Chiu, "Study of laminated object manufacturing with separately applied heating and pressing," *The International Journal of Advanced Manufacturing Technology,* vol. 27, pp. 703-707, 2006.

[90] M. J. Cima, J. S. Haggerty, E. M. Sachs, and P. A. Williams, "Three-dimensional printing techniques," U.S. Patent 5,204,055, 1993.

[91] K. Thrimurthulu, P. M. Pandey, and N. V. Reddy, "Optimum part deposition orientation in fused deposition modeling," *International Journal of Machine Tools and Manufacture,* vol. 44, pp. 585-594, 2004.

[92] K. Cooper, *Rapid prototyping technology: selection and application*: CRC press, 2001.

[93] R. Singh, "Process capability study of polyjet printing for plastic components," *Journal of Mechanical Science and Technology,* vol. 25, pp. 1011-1015, 2011.

[94] V. Petrovic, O. J. Ferrando, J. D. Gordillo, J. R. B. Puchades, and L. P. Grinan, "Additive layered manufacturing: sectors of industrial application shown through case studies," *International Journal of Production Research,,* vol. 49, pp. 1061-1079, 2011.

[95] D. Dimitrov, K. Schreve, and N. D. Beer, "Advances in three dimensional printing-state of the art and future perspectives," *Journal for New Generation Sciences,* vol. 4, pp. 21-49, 2006.

[96] D. Jijotiya and P. L. Verma, "A Survey of Performance based Advanced Rapid Prototyping Techniques," *Scholars Journal of Engineering and Technology,* vol. 1, pp. 4-12, 2013.

[97] P. J. Kitson, A. Macdonell, S. Tsuda, H. Zang, D.-L. Long, and L. Cronin, "Bringing Crystal Structures to Reality by Three-Dimensional Printing," *Crystal Growth and Design,* 2014.

[98] S. J. Leigh, R. J. Bradley, C. P. Purssell, D. R. Billson, and D. A. Hutchins, "A simple, low-cost conductive composite material for 3D printing of electronic sensors," *PloS One,* vol. 7, p. e49365, 2012.

[99] J. Cole, H. Lu, and W. Weise, "Literature Review 3D Printer," Southern Illinois University2013.

[100] M. Frauenfelder. (2015, February 5). *Ultimate guide to 3D printing 2014.* Available: Ultimate guide to 3D printing 2014

[101] F. R. DiMaio, "The science of bone cement: a historical review," *Orthopedics,* vol. 25, pp. 1399-1407, 2002.

[102] S. Breusch and K. Kühn, "[Bone cements based on polymethylmethacrylate]," *Der Orthopade,* vol. 32, pp. 41-50, 2003.

[103] G. Lewis, "Properties of acrylic bone cement: state of the art review," *Journal of Biomedical Materials Research,* vol. 38, pp. 155-182, 1997.

[104] J. E. Block and H. A. Stubb, "Reducing the risk of deep wound infection in primary joint arthroplasty with antibiotic bone cement," *Orthopedics-New Jersey,* vol. 28, p. 1334, 2005.

[105] D. A. Wininger and R. J. Fass, "Antibiotic-impregnated cement and beads for orthopedic infections," *Antimicrobial agents and chemotherapy,* vol. 40, p. 2675, 1996.

[106] D. Heck, A. Rosenberg, M. Schink-Ascani, S. Garbus, and T. Kiewitt, "Use of antibiotic-impregnated cement during hip and knee arthroplasty in the United States," *The Journal of Arthroplasty,* vol. 10, pp. 470-475, 1995.

[107] J. Leggett, S. Ebert, B. Fantin, and W. Craig, "Comparative dose-effect relations at several dosing intervals for beta-lactam, aminoglycoside and quinolone antibiotics against gram-negative bacilli in murine thigh-infection and pneumonitis models," *Scandinavian journal of infectious diseases. Supplementum,* vol. 74, pp. 179-184, 1989.

[108] M. Rubin, J. W. Hathorn, D. Marshall, J. Gress, S. M. Steinberg, and P. A. Pizzo, "Gram-positive infections and the use of vancomycin in 550 episodes of fever and neutropenia," *Annals of internal medicine,* vol. 108, pp. 30-35, 1988.

[109] P. F. Cabanillas, E. D. e. Peña, J. Barrales-Rienda, and G. Frutos, "Validation and in vitro characterization of antibiotic-loaded bone cement release," *International journal of pharmaceutics,* vol. 209, pp. 15-26, 2000.

[110] E. Lautenschlager, G. Marshall, K. Marks, J. Schwartz, and C. Nelson, "Mechanical strength of acrylic bone cements impregnated with antibiotics," *Journal of biomedical materials research,* vol. 10, pp. 837-845, 1976.

[111] W. Wei, E. Abdullayev, A. Hollister, D. Mills, and Y. M. Lvov, "Clay nanotube/poly methyl methacrylate) bone cement composites with sustained antibiotic release," *Macromolecular Materials and Engineering,* vol. 297, pp. 645-653, 2012.

[112] G. F. Knoll, *Radiation Detection and Measurement*, 3 ed. New York: John Wiley & Sons, Inc., 2000.

[113] (2015, February 24). *Tables of X-Ray Mass Attenuation Coefficients and Mass Energy-Absorption Coefficients from 1 keV to 20 MeV for Elements Z = 1 to 92 and 48 Additional Substances of Dosimetric Interest*.